Università degli Studi di Padova

Scuola di Dottorato in
Ingegneria dell'Informazione

Ph.D. Thesis

Disorder, Propagation, and Non-Linear Effects in Photonic Crystal Waveguides

Ph.D. Student
Giovanni Vadalà

School Director Ch.mo Prof. Matteo Bertocco

Supervisor Ch.mo Prof. Andrea Galtarossa

Padova, 31 December 2009

Al mio papà,
alla mia mamma
e ad Antonio

Ringraziamenti

Questo lavoro non sarebbe stato possibile senza il continuo supporto di Ermanna, che ha pazientemente condiviso questi tre anni di frequente lontananza. L'affetto dimostratomi con la sua presenza nei momenti difficili e di scoramento mi ha concesso la serenità necessaria per fare ricerca e realizzare così il mio sogno. Grazie!

Desidero ringraziare, inoltre, il prof. Andrea Galtarossa dell'Università di Padova, i cui consigli e aiuti sono stati fondamentali per iniziare - e finire - quest'avventura, il dr. Alfredo de Rossi, responsabile dell'Advanced Photonics Lab presso Thales Research and Technology, Paris, che mi ha dato l'opportunità di lavorare presso i laboratori Thales, il prof. Mike van der Pool e il prof. Jesper Mørk, che mi hanno supportato durante il mio lungo periodo presso l'Università Tecnica di Danimarca (DTU). Grazie di avermi dato l'opportunità di essere parte della grande avventura delle nanotecnologie ottiche di questi anni.

Un grazie, infine, va a tutti coloro con i quali abbiamo camminato fianco a fianco, in Italia, in Francia e in Danimarca, per le piacevoli discussioni sugli argomenti più disparati, per le serate insieme, per essermi stati amici. Grazie! Avete reso speciali questi tre anni di dottorato errante.

Contents

Figure Captions

Symbols

$\mathbf{r}$	position vector
t	time
ν	frequency
$\omega = 2\pi\nu$	angular frequency
λ	wavelength
c	speed of light in free space
μ_0	magnetic permeability in free space
$\varepsilon_0 = \dfrac{1}{\mu_0 c^2}$	electric permettivity in free space
ε	absolute permittivity
$\varepsilon_\mathrm{r} = \dfrac{\varepsilon}{\varepsilon_0}$	relative permettivity
$\mathbf{E}$	electric field
$\mathbf{D}$	electric displacement
$\mathbf{H}$	magnetic field
$\mathbf{B}$	magnetic induction
$\mathbf{P}$	polarization density
χ_e	electric susceptibility

Acronyms

PhC	Photonic Crystal
PCF	Photonic Crystal Fiber
PBG	Photonic Band Gap
PhCWG	Photonic Crystal Waveguide
FWM	Four Wave Mixing
TDR	Danish Telecom Research facility
DTU	Technical University of Denmark
TRT	Thales Research and Technology
AM	amplitude modulation
FM	frequency modulation

Sommario

Negli ultimi anni, grande attenzione è stata rivolta alle tecnologie fotoniche. La fotonica, chiamata così in analogia con l'elettronica, è divenuta una forza trainante in diverse aree come le comunicazioni e il computing, le tecnologie dell'informazione e anche le biotecnologie, grazie alle sue applicazioni nel campo dei sensori. I dispositivi fotonici offrono, infatti, una grande larghezza di banda unita alla mancanza di emissioni e a una elevata immunità alle interferenze.

All'aumentare della velocità di trasmissione, le connessioni ottiche sono passate dall'iniziale utilizzo come collegamento tra punti remoti (come nel caso delle dorsali telefoniche) a usi su scala sempre più locale (grandi reti aziendali, reti casalinghe, connessione di periferiche al computer); adesso, sono allo studio collegamenti ottici all'interno dei computer, fra chip diversi e all'interno dello stesso chip.

Dallo studio di collegamenti ottici all'interno dei chip allo sviluppo di circuiti interamente ottici, il passo è breve e diverse tecnologie sono allo studio per ottenere tale risultato, mantenendo costi di produzione e livelli di integrazione comparabili con quelli dei circuiti integrati elettronici.

Una delle tecnologie più studiate negli ultimi anni è quella dei cristalli fotonici. Tali metamateriali[1] offrono infatti la possibilità di controllare e modificare la propagazione delle onde luminose. É possibile pensare ai cristalli fotonici come l'analogo ottico dei normali cristalli: la periodicità nell'indice di rifrazione determina una struttura di bande permesse e proibite in funzione del vettore d'onda della luce incidente esattamente come avviene con le bande di conduzione e di valenza per gli elettroni nei cristalli ordinari. Quando la propagazione è inibita per ogni polarizzazione e ogni

[1] Si definisce metamateriale un materiale creato artificialmente con proprietà elettriche e magnetiche peculiari che lo differenziano dagli altri materiali. Le sue caratteristiche macroscopiche non dipendono solo dalla sua struttura molecolare, ma anche dalla sua geometria realizzativa.

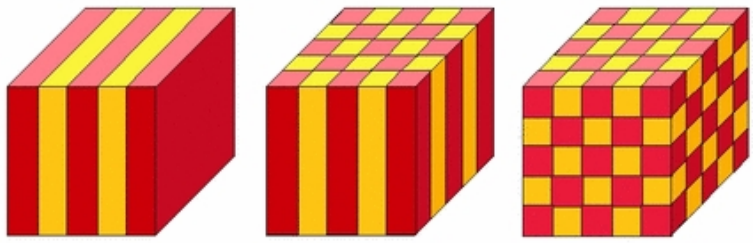

Figure 1: Un esempio di cristallo fotonico monodimensionale (a sinistra), bidimensionale (al centro) e tridimensionale (a destra)[1].

direzione all'interno del cristallo si ha un bandgap fotonico completo. Proprio per l'analogia con i cristalli ordinari, lo studio dei metamateriali si è avvantaggiato dei risultati già acquisiti dalla fisica dello stato solido.

La storia dei cristalli fotonici comincia nel 1987 con due lavori pionieristici di Eli Yablonovitch [2] e Sajeev John [3]. In entrambi i lavori, il punto di partenza era la fisica dello stato solido e come i fenomeni elettromagnetici si modificavano in presenza di strutture dielettriche periodiche. A partire da quei lavori, è stato definito cristallo fotonico qualsiasi sistema caratterizzato da una funzione dielettrica periodica in una o più dimensioni. La Fig. 1 mostra dei cristalli fotonici in una, due e tre dimensioni, a seconda della periodicità della funzione dielettrica ε. Il periodo della funzione è chiamato costante reticolare, ancora una volta in analogia alla costante reticolare dei reticoli cristallini nei cristalli naturali.

I cristalli fotonici offrono numerosi gradi di libertà in fase di progettazione e realizzazione, per esempio il materiale di cui sono realizzati, le dimensioni fisiche e la struttura della cella elementare. Infine è anche possibile inserire nella struttura periodica delle irregolarità (difetti), per ottenere bande permesse in regioni in cui precedentemente la propagazione della luce era inibita. A seconda del numero di dimensioni del difetto e del cristallo, si possono ottenere effetti diversi di localizzazione della luce; ad esempio, in un cristallo fotonico bidimensionale, un difetto puntuale assume le caratteristiche di una cavità bidimensionale, mentre un difetto lineare si comporta a tutti gli effetti come una guida d'onda, in cui la propagazione può avvenire non solo per riflessione interna totale, come in una fibra ottica, ma anche per effetto della struttura a bande del cristallo.

La grande libertà nel design permette, quindi, di realizzare numerosi dispositivi, sia attivi che passivi, come microcavità, guide d'onda, filtri e laser; tutto questo andando a modificare solo alcuni dei parametri che caratterizzano il cristallo, in

funzione dell'applicazione desiderata.

Esiste, infine, un altro grande vantaggio dei cristalli fotonici rispetto ad altre tecnologie fotoniche: la loro fabbricazione avviene, infatti, utilizzando gli stessi processi produttivi già usati nell'industria dell'elettronica, aprendo la via a una ipotetica rivoluzione tecnologica senza gli elevati costi di riconversione.

Questo lavoro di tesi presenta alcuni nuovi risultati sulle proprietà ottiche e sugli effetti del disordine sulla propagazione in guide d'onda a cristallo fotonico bidimensionale. Lo studio parte dai concetti di base dei cristalli fotonici (Cap. 1), quali la loro struttura a bande, fondamentali per comprendere appieno le proprietà dei cristalli fotonici bidimensionali (Cap. 2).

Nel Cap. 3 sono approfondite le proprietà di propagazione della luce nelle guide d'onda realizzate in cristalli bidimensionali, in particolare la loro tipica relazione di dispersione e il regime di propagazione noto come regime di Luce Lenta (*Slow Light regime*). Nello stesso capitolo, si introduce, inoltre, un modello teorico per il Four-Wave Mixing, fenomeno non lineare solo recentemente osservato in questo tipo di guide. Il Cap. 4 introduce brevemente i processi di fabbricazione per questi dispositivi; vengono quindi discussi i punti critici di tali processi, modellizzati come disordine estrinseco, e l'impatto che questi hanno sulle proprietà di propagazione della guida.

Gli ultimi due capitoli sono relativi alla parte sperimentale di questo lavoro. Sono state infatti studiate due tecniche per la caratterizzazione delle guide d'onda a cristallo fotonico. La prima è la mappa di riflettanza tempo-lunghezza d'onda (Cap. 5), sviluppato presso Thales Research and Technology (Paris, France), che permette di valutare le proprietà di propagazione della guida in funzione della lunghezza d'onda e l'impatto della dispersione indotta dal disordine estrinseco della guida. La seconda è la tecnica Heterodyne Pump-Probe, utilizzato presso il Dipartimento DTU Fotonik, Copenhagen, in una serie di esperimenti atti a indagare il regime di luce lenta e i ritardi ottenibili in tale regime.

La parte teorica di questa lavoro (Capitoli 1, 2 e 3) è stata sviluppata presso il Dipartimento di Ingegneria dell'Informazione dell'Università di Padova, sotto la supervisione del prof. Andrea Galtarossa, mentre la parte più applicativa e sperimentale è stata svolta presso l'Advanced Photonics Lab di Thales Research and Technology, Paris, in collaborazione con il dr. Alfredo de Rossi (Capitoli 4 e 5), e presso il Department of Photonics, della Technical University of Denmark, sotto la guida del prof. Mike van der Poel e del prof. Jesper Mørk (Capitolo 6).

Introduction

In recent years a great deal of attention has been devoted towards photonic materials. The technology of photons, named photonics in analogy with electronics, has become the driving force for the advancement of areas such as communications and computing, information technology and even biotechnology, for sensing devices. This technology provides larger bandwidth, high interference immunity and lack of emission. As the data transmission rate is increasing, the optical connection moves from long range to enterprise network and it is entering the domain of chip-to-chip and on-chip communication. This trend strengthens the demand of miniaturization and integration of optical signal transmission components.

An answer to this demand can be photonic crystals (aka periodic photonic structures), which study is experiencing a notable growth due to the dramatic ways in which such structures can control, modify and harvest the flow of light. They are the optical analogous of ordinary crystals, since their periodicity in refractive index determines a structure of allowed and forbidden bands for the light frequency dispersion with respect to the wavevector inside the structure. When light propagation is inhibited for any polarization and any direction inside the crystal a complete photonic bandgap is achieved. Due to the analogy between photonic and ordinary crystals, the study of these artificial materials took advantage of concepts well known in solid state physics, with the aim of investigating photonic band structure and optical spectra and of realizing functional devices.

The story of photonic crystals starts in 1987, when two pioneering works of Eli Yablonovitch [2] and Sajeev John [3] appeared on Physical Review Letters. Both articles deal with modification of electromagnetic phenomena when considering periodic dielectric structures. From those, photonic crystal has been the appellation for any system characterized by a dielectric function ε that is periodic in one or more

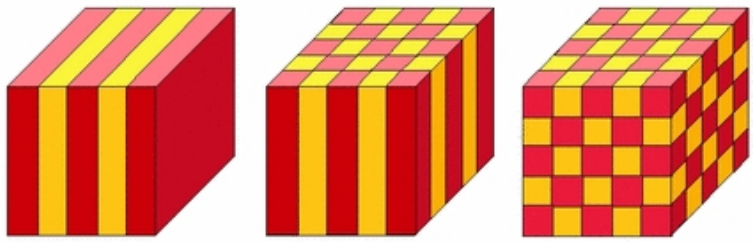

Figure 2: An example of one-dimensional (left), two-dimensional (center), and three-dimensional (right) photonic crystal [1]

dimensions. The classification into one-dimensional (1D), two-dimensional (2D), and three-dimensional (3D) photonic crystals depends on whether ε is periodic in one, two, or three dimensions, as shown in Fig. 2. The spatial period of the stack is called the lattice constant, since it corresponds to the lattice constant of ordinary crystals composed of a regular array of atoms.

The fact that photonic crystals are artificial materials opens infinite possibilities on the choice of the dielectric pattern. Furthermore, by designing defects in the otherwise periodic structure, it is possible to create defect states within the photonic band gap. According to the dimensionality of the defects itself and to the dimensionality of the photonic band gap, various degrees of light localization can be obtained [1]. For example, for a 2D photonic crystal, a point defect represents a two-dimensional cavity, and a linear defect forms a planar waveguide.

This concept envisages that several optical components could be designed on a single photonic crystal chip to process optical signals just a conventional electronic chip. The recently past years have provided important results as regards theory and experiments of passive photonic crystal blocks: micro-cavities, waveguides, filters, and lasers.

The present work would like contribute to the research in this area, by offering some results on the optical properties, disorder and non-linear effects on wave propagation in semiconductor-based two-dimensional photonic crystal waveguides. The aim is to lead the reader from the basic concepts of photonic crystals (Chapter 1), up to the properties of a 2D photonic crystal (Chapter 2) and the defect line induced waveguide in a 2D photonic crystal (Chapter 3). The propagation properties, the unusual dispersion relation, and the particular regime, known as Slow Light regime, will be analyzed depthly. Particular attention is devoted to model the extrinsic disorder induced by the fabrication process and its impact on the propaga-

tion properties of the waveguide (Chapter 4). In the last two chapters, the focus will be on two techniques to characterize photonic crystal waveguides. The first tool is the Time-Wavelength Reflectance Map (Chapter 5), developed with Thales Research and Technology, Paris, France, that permits to evaluate the propagation properties of the waveguide as function of the wavelength showing us a deep physical insight for understanding the role of disorder induced scattering and how it is connected to dispersion. In Chapter 6, a laboratory setup will be presented, based on the Heterodyne Pump-Probe technique, used in a set of experiments at DTU Fotonik, with the main objective to investigate on the Slow Light regime.

The part of the work that is more related to the fundamental research (Chapters 1, 2, 3) has been carried out mainly at the Department of Information Engineering, Università degli Studi di Padova (Padova, Italy), under the supervision of prof. Andrea Galtarossa. Instead, the part that is more application oriented (Chapters 4, 5) has been accomplished in the Advanced Photonics Lab at Thales Research and Technology (Paris, France) supervised by dr. Alfredo de Rossi, while the laboratory part (Chapter 6) has been carried out at the Department of Photonics, Technical University of Denmark (Copenhagen, Denmark), under the supervision of prof. Mike van der Poel and prof. Jesper Mørk.

Chapter 1

General Concepts on Photonic Crystals

The theoretical approach to photonic crystals is based on the rearrangement of Maxwell's equation in form of eigenvalue for the harmonic Fourier components of the electric and magnetic fields. This formulation has been used to develop numerical methods to predict their band structure from the geometric properties. For a more complete theoretical description of photonic crystals properties the reader can refer to the Sakoda [4] and Joannopoulos [1] books, on which this chapter is based.

1.1 Photonic Crystals

A photonic crystal (PhC) is characterized by a relative dielectric permittivity $\varepsilon_{\mathrm{r}}(\mathbf{r})$ assumed to be periodic along N directions (with $N = 1$, 2 or 3) and invariant along the other $3-N$ orthogonal directions. Initially, we assume it extends infinitely along all the directions. We can model it as a unit cell repeated in space according to a well defined pattern. All of those can be reduced to the two mathematical concepts of basis and lattice. The lattice defines the spatial arrangement of the unit cell, while the basis specifies the content of the unit cell.

The lattice is generated by linear combination of the so-called primitive vectors $\mathbf{a}_i$, where $i \in \{1, \ldots, N\}$, which are determined by the minimum translation that leaves the dielectric function unchanged. Choosing a reference frame and placing a lattice point at the origin of it, any other lattice point has a one-to-one correspondence with a vector $\mathbf{R}$, linear combination of $\mathbf{a}_i$:

$$\mathbf{R} = \sum_{i=1}^{N} n_i \mathbf{a}_i, \tag{1.1}$$

where n_i are integers.

In mathematical terms, the lattice is defined by a vector space $\mathbb{V}$, with basis $\{\mathbf{a}_i\}$. The dimensionality of $\mathbb{V}$ is N. The unit cell of the crystal has the same dimension of $\mathbb{V}$ and the space A_c that occupies is determined by the primitive vectors:

$$A_c = \begin{cases} |\mathbf{a}_1|, & \text{1D} \\ |\mathbf{a}_1 \times \mathbf{a}_2|, & \text{2D} \\ |\mathbf{a}_1 \cdot (\mathbf{a}_2 \times \mathbf{a}_3)|, & \text{3D.} \end{cases} \tag{1.2}$$

The dielectric function of a photonic crystal has the property

$$\varepsilon_{\mathrm{r}}(\mathbf{r} + \mathbf{R}) = \varepsilon_{\mathrm{r}}(\mathbf{r}), \qquad \forall \mathbf{R} \in \mathbb{V}, \tag{1.3}$$

that means the photonic crystal is invariant for any discrete translation defined by a vector $\mathbf{R} \in \mathbb{V}$.

1.2 Maxwell's equation for a photonic crystals

The propagation of an electromagnetic wave in a PhC free of charges and currents is governed by Maxwell's equations, which the more general form, in SI units, are

$$\begin{aligned} \nabla \cdot \mathbf{D}(\mathbf{r}, t) &= 0 & \nabla \cdot \mathbf{B}(\mathbf{r}, t) &= 0 \\ \nabla \times \mathbf{E}(\mathbf{r}, t) &= -\frac{\partial \mathbf{B}(\mathbf{r}, t)}{\partial t} & \nabla \times \mathbf{H}(\mathbf{r}, t) &= \frac{\partial \mathbf{D}(\mathbf{r}, t)}{\partial t} \end{aligned} \tag{1.4}$$

where $\mathbf{E}$, $\mathbf{D}$, $\mathbf{B}$, $\mathbf{H}$ are respectively the electric field, the electric displacement, the magnetic induction and the magnetic field.

The constitutive relation that relates $\mathbf{E}$ and $\mathbf{D}$ is

$$\begin{aligned} &\mathbf{D}(\mathbf{r}, t) = \varepsilon_0 \mathbf{E}(\mathbf{r}, t) + \mathbf{P}(\mathbf{r}, t) \\ &\text{with} \quad \mathbf{P}(\mathbf{r}, t) = \varepsilon_0 \int \chi_{\mathrm{e}}(\mathbf{r}, \mathbf{r}', t, t'; \mathbf{E})\, \mathbf{E}(\mathbf{r}', t') d\mathbf{r}' dt', \end{aligned} \tag{1.5}$$

where $\mathbf{P}$ is the polarization density and is expressed as a convolution in space and time of the tensor electric susceptibility $\chi_{\mathrm{e}}(\mathbf{r}, t)$ and the electric field.

A similar one connects the magnetic filed $\mathbf{H}$ to the magnetic induction$\mathbf{B}$ through the tensor magnetic susceptibility $\chi_{\mathrm{m}}(\mathbf{r}, t)$.

Assuming that the media composing the photonic crystals are isotropic, non-dispersive, real and non-negative, and non magnetic, the constitutive relations become:

$$\begin{aligned} \mathbf{D}(\mathbf{r},t) &= \varepsilon_0 \varepsilon_r(\mathbf{r})\mathbf{E}(\mathbf{r},t) \\ \mathbf{B}(\mathbf{r},t) &= \mu_0 \mathbf{H}(\mathbf{r},t), \end{aligned} \tag{1.6}$$

where ε_0 and μ_0 are the electric permettivity and the magnetic permeability in free space, and $\varepsilon_r(\mathbf{r})$ is the relative permettivity, defined as $\varepsilon_{\mathrm{r}}(\mathbf{r}) = (1 + \chi_{\mathrm{e}}(\mathbf{r}))$.

Using Eqs. 1.6, Maxwell's equations are simplified to

$$\begin{aligned} \nabla \cdot \varepsilon_r(\mathbf{r})\mathbf{E}(\mathbf{r},t) = 0 \qquad & \nabla \cdot \mathbf{H}(\mathbf{r},t) = 0 \\ \nabla \times \mathbf{E}(\mathbf{r},t) = -\mu_0 \frac{\partial \mathbf{H}(\mathbf{r},t)}{\partial t} \qquad & \nabla \times \mathbf{H}(\mathbf{r},t) = \varepsilon_0 \varepsilon_r(\mathbf{r}) \frac{\partial \mathbf{E}(\mathbf{r},t)}{\partial t} \end{aligned} \tag{1.7}$$

Thanks to the linearity of Maxwell's equations, it is convenient to look for solutions for harmonic fields

$$\mathbf{E}(\mathbf{r},t) = \mathbf{E}(\mathbf{r})e^{-\imath\omega t}, \qquad \mathbf{H}(\mathbf{r},t) = \mathbf{H}(\mathbf{r})e^{-\imath\omega t}. \tag{1.8}$$

The general solution will be the superposition of harmonic modes. Substituting the formulae 1.8 into Eqs. 1.7, it is possible to recast Maxwell equations in a closed form for the magnetic or electric field

$$\frac{1}{\varepsilon_{\mathrm{r}}(\mathbf{r},\omega)} \nabla \times [\nabla \times \mathbf{E}(\mathbf{r},\omega)] = \frac{\omega^2}{c^2} \mathbf{E}(\mathbf{r},\omega) \tag{1.9}$$

$$\nabla \times \left[\frac{1}{\varepsilon_{\mathrm{r}}(\mathbf{r},\omega)} \nabla \times \mathbf{H}(\mathbf{r},\omega) \right] = \frac{\omega^2}{c^2} \mathbf{H}(\mathbf{r},\omega) \tag{1.10}$$

where $c = 1/\sqrt{\varepsilon_0 \mu_0}$ is the speed of light in free space. We define the wave number $k = \omega/c = 2\pi/\lambda$, with λ wavelength of light in free space.

The propagation equations (Eqs. 1.9 and 1.10) have to be considered as distribution, because include boundary conditions at the interfaces of the different materials and the continuity of the tangential components of the electric and magnetic fields.

It is possible recast Eqs. 1.9 and 1.10 in the more compact form

$$\hat{\Theta}_E \mathbf{E}(\mathbf{r},\omega) = \frac{\omega^2}{c^2} \mathbf{E}(\mathbf{r},\omega), \tag{1.11}$$

$$\hat{\Theta}_H \mathbf{H}(\mathbf{r},\omega) = \frac{\omega^2}{c^2} \mathbf{H}(\mathbf{r},\omega), \tag{1.12}$$

where we introduced the operators $\hat{\Theta}_E$ and $\hat{\Theta}_H$:

$$\hat{\Theta}_E = \frac{1}{\varepsilon_{\mathrm{r}}(\mathbf{r},\omega)} \nabla \times [\nabla \times], \tag{1.13}$$

$$\hat{\Theta}_H = \nabla \times \left[\frac{1}{\varepsilon_{\mathrm{r}}(\mathbf{r},\omega)} \nabla \times \right], \tag{1.14}$$

so that the Maxwell's equations are transformed in a eigenvalue problem, where $k^2 = \omega^2/c^2$ are the eigenvalues and the fields are the eigenfunctions.

While $\hat{\Theta}_E$ is an operator for a generalized eigenvalue problem, $\hat{\Theta}_H$ identify an Hermitian positive definite operator [5]:

$$< F, \hat{\Theta}_H F > = < \hat{\Theta}_H F, F > \qquad \forall F, \tag{1.15}$$

where $<,>$ stands for the scalar product. This guarantees that eigenvalues are real and non-negative, and a complete set of orthonormal eigenfunctions does exist.

The above consideration and the fact that the magnetic field is transverse ($\nabla \cdot \mathbf{H} = 0$) make more convenient to solve the problem using the Eq. 1.14; this is the choice usually adopted by the research community and will be also used in this work.

Up to now, the derivation of the master equation is valid for any system for which the initial assumptions are fulfilled, without further specifications.

1.3 The Bloch-Floquet Theorem

To solve the electromagnetic problem for a PhC, it is necessary to impose the periodicity of the dielectric function given by Eq. 1.3. Photonic crystals are invariant under discrete translational symmetry defined by any vector $\mathbf{R}$ defined in Eq. 1.1. Being $\hat{T}_R$ the unitary operator associated with the discrete translation $\mathbf{R}$, the rule for transformation reads

$$\begin{aligned} \hat{\Theta}'_H &= \hat{T}_R \hat{\Theta}_H \hat{T}_R^{-1}, \\ \varepsilon' &= \hat{T}_R \varepsilon \hat{T}_R^{-1}, \\ \mathbf{H}'(\mathbf{r}) &= (\hat{T}_R \mathbf{H})(\hat{T}_R^{-1}\mathbf{r}), \end{aligned} \tag{1.16}$$

where ε' and $\mathbf{H}'$ are the transformed dielectric constant and the transformed field, respectively.

Since the PhC is invariant for this kind of transformation, the operator $\hat{\Theta}_H$ and the dielectric function ε are left unchanged, and the rules become

$$\begin{aligned} \hat{\Theta}_H &= \hat{T}_R \hat{\Theta}_H \hat{T}_R^{-1}, \\ \varepsilon &= \hat{T}_R \varepsilon \hat{T}_R^{-1}, \\ \mathbf{H}'(\mathbf{r}) &= (\hat{T}_R \mathbf{H})(\hat{T}_R^{-1}\mathbf{r}), \end{aligned} \tag{1.17}$$

The application of the operator $\hat{T}_R$ to the master equation yields a new eigenvalue problem for the transformed $\mathbf{H}'$, but the condition $< \hat{\Theta}_H, \hat{T}_R >= 0$ implies that $\mathbf{H}'$ must satisfy the same equation that holds for $\mathbf{H}$:

$$\hat{\Theta}_H \mathbf{H} = \frac{\omega^2}{c^2}\mathbf{H} \quad \Longleftrightarrow \quad \hat{\Theta}_H \hat{T}_R \mathbf{H} = \frac{\omega^2}{c^2}\hat{T}_R \mathbf{H} \tag{1.18}$$

Such condition is fulfilled if $\mathbf{H}'$ is equal to $\mathbf{H}$ within a multiplication factor, which implies that $\mathbf{H}$ is, in the most general form, a linear combination of degenerate eigenfunctions of the operator $\hat{T}_R$

$$\hat{T}_R \mathbf{H}(\mathbf{r}) = \alpha \mathbf{H}(\mathbf{r}). \tag{1.19}$$

The eigenfunctions of $\hat{T}_R$ are plane waves and the eigenvalues are complex numbers of unitary modulus:

$$\mathbf{f}_\mathbf{k}(\mathbf{r}) = \mathbf{f}_0 e^{\imath \mathbf{k}\cdot\mathbf{r}} \qquad \hat{T}_R \mathbf{f}_\mathbf{k}(\mathbf{r}) = e^{\imath \mathbf{k}\cdot\mathbf{R}} \mathbf{f}_\mathbf{k}(\mathbf{r}) \qquad \alpha = e^{-\imath \mathbf{k}\cdot\mathbf{R}}, \tag{1.20}$$

where $\mathbf{f}$ is the eigenfunction and $\mathbf{k}$ is the wave-vector. Notice that all the eigenfunctions $\mathbf{f}_{\mathbf{k}'}(\mathbf{r})$ and $\mathbf{f}_\mathbf{k}(\mathbf{r})$, with $\mathbf{k}' = \mathbf{k} + \mathbf{G}$ so that $\mathbf{G}\cdot\mathbf{R} = 2n\pi$, are degenerate.

The condition

$$\mathbf{G}\cdot\mathbf{R} = 2n\pi \tag{1.21}$$

defines the dual space $\mathbb{G}$ of the vector space $\mathbb{V}$. If $\{\mathbf{a}_i\}$ is the basis for $\mathbb{V}$, the basis for the dual space $\mathbb{G}$ is $\{\mathbf{g}_i\}$:

$$\mathbf{a}_i \cdot \mathbf{g}_j = 2\pi\delta_{ij} \quad \mathbf{G} = \sum_{i=1}^{N} l_i \mathbf{g}_i \tag{1.22}$$

where l_i are arbitrary integer numbers and δ_{ij} is Kronecker's delta.

Two eigenfunctions $\mathbf{f}_{\mathbf{k}'}(\mathbf{r})$ and $\mathbf{f}_\mathbf{k}(\mathbf{r})$ are degenerate if $\mathbf{k}' - \mathbf{k} \in \mathbb{G}$.

The general solution of the master equation is therefore

$$\mathbf{H}_\mathbf{k}(\mathbf{r}) = \sum_{\mathbf{G}\in\mathbb{G}} c(\mathbf{k}+\mathbf{G}) \mathbf{f}_{\mathbf{k}+\mathbf{G}}(\mathbf{r}). \tag{1.23}$$

The divergence condition $\nabla \cdot \mathbf{H_k}(\mathbf{r}) = 0$, that imposes that $\mathbf{H_k}$ is transverse, is automatically fulfilled if $(\mathbf{k}+\mathbf{G}) \cdot \mathbf{f_{k+G}}(\mathbf{r}) = 0$, i.e. $\mathbf{f_{k+G}}(\mathbf{r})$ is also transverse.

Since $\mathbf{H_k}(\mathbf{r})$ is also eigenfunction of $\hat{T}_R$ with the same eigenvalue α of $\mathbf{f_k}(\mathbf{r})$, the application of $\hat{T}_R$ to $\mathbf{H_k}(\mathbf{r})$ yields

$$\hat{T}_R \mathbf{H_k}(\mathbf{r}) = \mathbf{H_k}(\mathbf{r}-\mathbf{R}) = e^{-\imath \mathbf{k}\cdot\mathbf{R}} \mathbf{H_k}(\mathbf{r}). \tag{1.24}$$

The last equation represents the *Bloch-Floquet theorem*, that states that the general solution of a master equation invariant under a translational symmetry operation $\hat{T}_R$ is a periodic function $\mathbf{u_k}(\mathbf{r})$ multiplied by a phase factor $\exp(\imath \mathbf{k}\cdot\mathbf{r})$. The period of $\mathbf{u_k}(\mathbf{r})$ is determined by the elementary translational operators $\hat{T}_{\mathbf{a}_i}$.

The operator formalism and the use of symmetry have helped in finding the general form for the solution of Maxwell's equation in a PhC. What has been derived is also valid for the electric field, because the knowledge of one field determines the other one by straightforward application of Maxwell's equations.

From Eq. 1.24, it is evident that $\mathbf{H_{k'}}(\mathbf{r}) = \mathbf{H_k}(\mathbf{r})$ if $\mathbf{k'} - \mathbf{k} \in \mathbb{G}$, because of the sum over the $\mathbf{G}$ vectors; different $\mathbf{k'}$ do not necessarily correspond different solutions $\mathbf{H_k}(\mathbf{r})$. The physical meaning is that in a PhC the wave vector $\mathbf{k}$ is conserved within a vector $\mathbf{G}$, and so $\mathbf{k}$ is not a "good quantum number" for the system.

The wave vectors $\mathbf{k}$ span the reciprocal space $\mathbb{K}^3$, which is the dual space of the Euclidean space $\mathbb{R}^3$. The reciprocal space can be divided into classes of equivalence $[\mathbf{k}]$, that we define as

$$[\mathbf{k}] = \{(\mathbf{k}, \mathbf{k'}) \in \mathbb{K}^3 \times \mathbb{K}^3 : \mathbf{k'} - \mathbf{k} \in \mathbb{G}\}. \tag{1.25}$$

Each class of equivalence $[\mathbf{k}]$ points to different $\mathbf{H_k}$, where $\mathbf{k}$ is representative of the class. The class of equivalence $[\mathbf{k}]$ of the momentum $\mathbf{k}$ is conserved in a photonic crystal, and $[\mathbf{k}]$ is a good quantum number. The representative of each class $[\mathbf{k}]$ is called the Bloch vector $\mathbf{k}$. Even if the choice of the Bloch vectors is not unique, they are a convenient working choice, lending themselves to a physical interpretation.

Usually the Bloch vector is taken as the smallest element of the class, in modulus, and the ensemble of such vectors define the *first Brillouin zone* (BZ):

$$BZ = \left\{ \mathbf{k} \in \mathbb{K}^3 \ : \ |\mathbf{k}| = \min_{z \in [\mathbf{k}]}(|z|) \right\} \tag{1.26}$$

It is possible to define a unit cell in the reciprocal space. Correspondingly, there will be a reciprocal lattice which determines how the unit cell tiles the reciprocal

space. We can obtain the primitive vectors $\mathbf{g}_i$ in the reciprocal space $\mathbb{G}$ from Eq. 1.22

$$\mathbf{g}_i = 2\pi \frac{\mathbf{a}_j \times \mathbf{j}_k}{\mathbf{a}_i \cdot (\mathbf{a}_j \times \mathbf{j}_k)}, \qquad \text{3D}; \tag{1.27}$$

$$\mathbf{g}_i = 2\pi \lim_{\delta \to 0} \frac{\mathbf{a}_j \times \delta\mathbf{k}}{\mathbf{a}_i \cdot (\mathbf{a}_j \times \delta\mathbf{k})}, \qquad \text{2D}; \tag{1.28}$$

$$\mathbf{g}_1 = 2\pi \frac{\mathbf{a}_1}{|\mathbf{a}_1|}, \qquad \text{1D}; \tag{1.29}$$

where $\mathbf{k}$ gives the direction of the axis perpendicular to the plane in which there is the crystal, and i, j, k label the primitive vectors.

According the Eq. 1.26, the Brillouin zone is the region delimited by cutting the reciprocal space with planes perpendicular to the primitive vectors having distance $|\mathbf{g}_i/2|$ from the origin. Thus, once the primitive vectors of the reciprocal lattice have been calculated, the Brillouin zone can be easily drawn.

Before proceeding, it is worth to remark that the spectrum ω can be classified by considering also other symmetry properties for the PhC. For example, the invariance of the master equation under time reversal yields $\omega(\mathbf{k}) = \omega(-\mathbf{k})$. This means that we can reduce the study of the spectrum to the Brillouin zone with non-negative Bloch vectors. There are also other symmetries that can held in spectrum calculation simplification, as transformation with a fixed point (rotations, inversion, reflections), gathered in the point group of the crystal. Thanks to them, we can reduce the set of the points where the master equation has to be solved. This reduced set is called the *irreducible Brillouin zone*, and can be much smaller than the whole Brillouin zone.

Furthermore, to avoid solving the master equation for every point of the irreducible Brillouin zone, it is often enough to do it along the symmetry lines, because they correspond to higher degree of symmetry with respect to the internal points and, for this reason, are more representative.

1.4 The Band Structure

The eigenfunctions of the master equation can be classified by means of the Bloch vector $\mathbf{k}$. As $\mathbf{k}$ varies in the Brillouin zone, the eigenvalues $k^2 = \frac{\omega^2}{c^2}$ obey to a certain dispersion relation $\omega = \omega(\mathbf{k})$. There is no one-to-one correspondence between the Bloch vector and the solutions of the master equation. In fact, it is possible that two solutions $\mathbf{H}_\mathbf{k}(\mathbf{r})$ have the same Bloch vector, but different expansion coefficients

$c(\mathbf{k}+\mathbf{B})$ in Eq. 1.24. There are infinite choices for $c(\mathbf{k}+\mathbf{B})$ yielding independent linear combinations of the basis functions $\mathbf{f}_{\mathbf{k}+\mathbf{G}}(\mathbf{r})$. This means that for each value of $\mathbf{k}$ we expect an infinite set of modes with discretely spaced frequencies, which can be labeled with a band index n

$$\mathbf{H}_{\mathbf{k},n}(\mathbf{r}) = \sum_{\mathbf{G}\in\mathbb{G}} c_n(\mathbf{k}+\mathbf{G})\mathbf{f}_{\mathbf{k}+\mathbf{G}}(\mathbf{r}), \qquad \omega = \omega(\mathbf{k}). \tag{1.30}$$

A more intuitive view of the problem is possible considering the analogy with the quantum mechanics problem of the electron in a box. Considering the eigenvalue problem as restricted to a single unit cell of the PhC, it is similar to the restriction of the eigenvalue problem for the electron to a finite volume that leads to a discretization of the energy spectrum. To have some general prediction on the function $\omega(\mathbf{k})$, we can observe that $\mathbf{k}$ enter in the master equation only as parameter, so we expect the frequency of each band for a given $\mathbf{k}$ to vary continuously as $\mathbf{k}$ varies. So, the modes of a PhC are a family of continuous functions, $\omega_n(\mathbf{k})$, indexed in order of increasing frequency by the band number n. The information contained in these functions is called the band structure of the PhC.

In addition to the Bloch vector and the index n, there is also another important degree of freedom that characterizes this solution of the master equation: the polarization σ. The magnetic field vector has three components, two of which independent, because of the divergence equation. As a consequence, for each choice of $(\mathbf{k}, n)$, there are two independent solutions with different polarization. In general, the polarization is not independent of the Bloch vectors: $\sigma = \sigma(\mathbf{k})$.

For this reason, it is convenient to include the polarization degree of freedom in the band index n. Only in specific cases, where at least one polarization is independent of the Bloch vector, the index σ is used to label the eigenfunctions and the eigenfrequencies. This is, for instance, the case for in-plane propagation in 2D photonic crystals.

1.5 The Photonic Bandgap

A photon with frequency ω propagates in a PhC, only if $\exists(\mathbf{k}, n) \ : \ \omega = \omega_n(\mathbf{k})$. Thus the spectral region $[\omega_1, \omega_2]$ for which $\forall\omega \in [\omega_1, \omega_2] \ \nexists(\mathbf{k}, n) \ : \ \omega = \omega(\mathbf{k})$ is called "photonic bandgap" and is characterized by a null density of states (DOS)

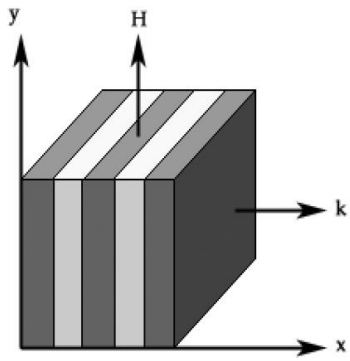

Figure 1.1: Geometry of a 1D PhC.

$\rho(\omega)$ defined [6] as

$$\rho(\omega) = \sum_{n} \sum_{\mathbf{k} \in BZ} \delta(\omega - \omega_n(\mathbf{k})). \tag{1.31}$$

The DOS is another important quantity characterizing the PhC. Contrary to the smooth DOS for an homogeneous medium, in a PhC DOS presents jumps with peaks and dips around a mean value given by the effective medium theory [6][7]. The calculation of the DOS is an important check for the existence of a photonic bandgap, because it accounts for all the Bloch vectors in the BZ, whereas the band structure is often limited to the symmetry lines of the BZ.

In order to understand intuitively photonic bands and bandgaps, it is useful to consider a simple structure, like a dielectric multilayer (1D PhC), with two layers characterized by the dielectric constant ε_1 and ε_2 and thickness l_1 and l_2, respectively. The optical properties of this structure are well-know [8]. We take the x axis in the direction perpendicular to the surface of the dielectric layers as shown in Fig. 1.1. For simplicity, we consider only electromagnetic waves propagating in the x direction and linearly polarized in the y direction. The magnetic field is denoted by the complex function $H(x,t)$ for convenience.

The wave equation for $H(x,t)$ is given by

$$\frac{c^2}{\varepsilon_r(x)} \frac{\partial^2 H}{\partial x^2} = \frac{\partial^2 H}{\partial t^2}, \qquad \varepsilon_r(x) = \varepsilon_r(x+a) \tag{1.32}$$

where $a = l_1 + l_2$ is the total length of two dielectric layers.

Because of the periodicity of $\varepsilon_r(x)$, the function $\varepsilon_r^{-1}(x)$ is also periodic and, thus,

expandable in a Fourier series

$$\varepsilon_r^{-1}(x) = \sum_{m=-\infty}^{\infty} \kappa_m \exp\left(\imath \frac{2\pi m}{a} x\right), \tag{1.33}$$

where $m \in \mathbb{N}$ and $\{\kappa_m\}$ are the Fourier coefficients.

Assuming $\varepsilon_r(x)$ real, it holds $\kappa_{-m} = \kappa_m *$. We know that $H(x,t)$ can be expressed as a Bloch function

$$H(x,t) \equiv H_k(x,t) = f_k(x) \exp[\imath(kx - \omega_k t)], \qquad f_k(x) = f_k(x+a), \tag{1.34}$$

and, hence, can be expanded in a Fourier series, too:

$$H_k(x,t) = \sum_{m=-\infty}^{\infty} H_m \exp\left[\imath\left(k + \frac{2\pi m}{a}\right) x - \imath\omega_k t\right], \tag{1.35}$$

where $\{H_m\}$ are the Fourier coefficients.

Assuming for simplicity that only the components with $m = 0, \pm 1$ are dominant in the expansion 1.33, it reads

$$\varepsilon_r^{-1}(x) \approx \kappa_0 + \kappa_1 \exp\left(\imath \frac{2\pi}{a} x\right) + \kappa_{-1} \exp\left(-\imath \frac{2\pi}{a} x\right), \tag{1.36}$$

and substituting Eqs. 1.35 and 1.36 into the wave equation 1.32, we obtain

$$\begin{aligned} \kappa_1 \left[k + \frac{2\pi(m-1)}{a}\right]^2 H_{m-1} + \kappa_{-1} \left[k + \frac{2\pi(m+1)}{a}\right]^2 H_{m+1} \\ \approx \left[\frac{\omega_k^2}{c^2} - \kappa_0 \left(k + \frac{2\pi m)}{a}\right)^2\right] H_m. \end{aligned} \tag{1.37}$$

For $m = 0$,

$$H_0 = \frac{c^2}{\omega_k^2 - \kappa_0 k^2 c^2} \left[\kappa_1 \left(k - \frac{2\pi}{a}\right)^2 H_{-1} + \kappa_{-1} \left(k + \frac{2\pi}{a}\right)^2 H_1\right]. \tag{1.38}$$

For $m = -1$,

$$H_1 = \frac{c^2}{\omega_k^2 - \kappa_0 (k - 2\pi/a)^2 c^2} \left[\kappa_1 \left(k - \frac{4\pi}{a}\right)^2 H_{-2} + \kappa_{-1} k^2 H_0\right]. \tag{1.39}$$

Therefore, if $k \approx \pi/a$, and if $\omega_k^2 \approx \kappa_0 k^2 c^2$, H_0 and H_1 are dominant in the expansion 1.35, and we can neglect all the other terms and obtain the following coupled equations:

$$\begin{aligned} (\omega_k^2 - \kappa_0 k^2 c^2) H_0 - \kappa_1 c^2 (k - 2\pi/a)^2 H_{-1} = 0 \\ -\kappa_{-1} c^2 k^2 H_0 + [\omega_k^2 - \kappa_0 (k - 2\pi/a)^2 c^2) H_{-1} = 0, \end{aligned} \tag{1.40}$$

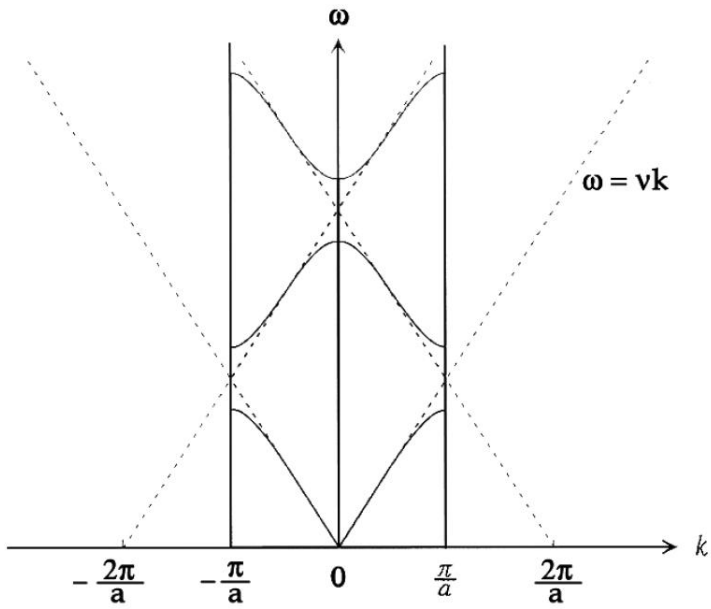

Figure 1.2: Dispersion relation for a 1D PhC (solid lines). The boundary of the BZ is denoted by two vertical lines. The dispersion lines in the uniform material are denoted by the dashed lines. They are folded into the BZ taking into account the identity of wave vectors which differ from each other by a reciprocal vector lattice $\mathbf{G}$, in this case equal to $2\pi/a$. When two dispersion lines cross, they repel each other and a photonic bandgap appears.

which solutions are

$$\omega_{\pm} = \frac{\pi c}{a}\sqrt{\kappa_0 \pm |\kappa_1|} \pm \frac{ac}{\pi|\kappa_1|}\left(\kappa_0^2 - \frac{|\kappa_1|^2}{2}\right)h^2, \tag{1.41}$$

where $h = k - \pi/a$, as far as $|h| << \pi/a$.

In the interval

$$\frac{\pi c}{a}\sqrt{\kappa_0 - |\kappa_1|} < \omega < \frac{\pi c}{a}\sqrt{\kappa_0 + |\kappa_1|} \tag{1.42}$$

there are no modes. The gap, of course, disappears if $\kappa_1 = 0$, i.e. when there is no spatial modulation in the dielectric function.

When the spatial modulation is small, the dispersion relation in the PhC is not so far from $\omega = vk$, but it should be expressed with the wave vector in the BZ, $[\pi/\,\pi/a]$. In addition, if two dispersion lines cross each other, a frequency gap appears. This consideration are schematized in Fig. 1.2.

The group velocity of an eigenmode is given by the slope of the dispersion relation:

$$v_g = \frac{\partial\omega(\mathbf{k})}{\partial\mathbf{k}}. \tag{1.43}$$

From Eq. 1.42, we can notice that for $k \to \pi/a$, $h \to 0$, hence also $v_g \to 0$. This means that eigenmodes near the BZ's edge are standing waves.

As regards the first band, if $k \to 0$, then $\omega \to 0$. This is the long-wavelength limit, according to which the PhC can be treated as an effective homogeneous medium, with a linear dispersion $\omega = ck/n_{\text{eff}}$[4], where $n_{\text{eff}} = \sqrt{\varepsilon_{\text{eff}}}$ is the effective refractive index. For the dielectric multilayer used in our example, an analytical expression for ε_{eff} has been obtained [9]:

$$\varepsilon_{\text{eff}} = (\varepsilon_1 l_1 + \varepsilon_2 l_2)/a.$$

1.6 The scaling properties

One of the differences between photonic crystals and conventional crystals is that photons do not have a fundamental length, contrary to electrons, which fundamental length is the Bohr radius $a_\circ$. This feature leads to the scaling invariance for the macroscopic Maxwell's equations. The PhC can be expanded or reduced via the following transformation

$$\varepsilon'(s\mathbf{r}) = \varepsilon(\mathbf{r}), \tag{1.44}$$

where s is the scaling factor. It is easy to show that the eigenfunctions and the eigenvalues of the master equation scale with $\varepsilon(\mathbf{r})$: $\mathbf{H}'(s\mathbf{r}) = \mathbf{H}(\mathbf{r})$ and $\omega' = \omega/s$. This means that the new mode profile and its corresponding frequency can be obtained by simply rescaling the old mode profile and its frequency. The solution of the problem at one length scale determines the solutions at all the other length scales. This property is of particular interest, because it permits to develop a particular geometries and then to tune the portion of the spectrum by changing only the lattice constant of the PhC.

Just as there is no fundamental length scale, there is also no fundamental value of the dielectric constant. If we use the following transformation

$$\varepsilon'(\mathbf{r}) = \varepsilon(\mathbf{r})/s^2, \tag{1.45}$$

we find that the harmonic modes of the new system are unchanged, but the frequencies are all scaled by a factor s, $\omega' = s\omega$. This implies that for a PhC made of two media $\varepsilon_1, \varepsilon_2$, the eigenfrequencies depend only on the ratio $\varepsilon_1/\varepsilon_2$.

Combining the above two relations, we can see that if we scale ε by s^2 and also rescale the coordinates by s, the frequency ω is unchanged.

1.7 The plane wave expansion method

After almost two decades of research in photonic bandgap materials, several techniques have been proposed for solving Maxwell's equations [10], [11], [12], but the standard de facto for computing the band structure of semiconductor-based photonic crystals is the plane-wave expansion method, based on the truncation of the sum in Eq. 1.23, that allows to reduce the master equation to a matrix eigenvalue problem. The coefficients $c_n(\mathbf{k}+\mathbf{G})$ and the eigenfrequencies $\omega_n(\mathbf{k})$ are obtained by standard numerical diagonalization of the resulting Hamiltonian.

Since the basis functions $\mathbf{f_k}(\mathbf{r})$ are plane waves, the Eq. 1.23 is explicitly written as

$$\mathbf{H}_k(\mathbf{r}) = \sum_{\mathbf{G}\in\mathbb{G}} \sum_{\sigma} c_\sigma(\mathbf{k}+\mathbf{G})\mathbf{f}_\sigma e^{\imath(\mathbf{k}+\mathbf{G})\cdot\mathbf{r}}, \tag{1.46}$$

where $\sigma = \sigma(\mathbf{k}+\mathbf{G})$ represents the two polarizations of $\mathbf{f}_\sigma$, with $\mathbf{f}_\sigma \cdot (\mathbf{k}+\mathbf{G}) = 0$. By truncating the index $\mathbf{G} \in \mathbb{G}$ to a cut-off $K \;:\; |\mathbf{G}| < K$, Eq. 1.46 becomes a finite expansion. The cut-off is the approximation imposed by the numerical method; in fact, it would be impossible to store infinite arrays in the computer memory. Eq. 1.46 is the Fourier expansion of the magnetic field truncated to a cut-off and $c_\sigma(\mathbf{k}+\mathbf{G})$ are its Fourier coefficients.

The next step is to rewrite the master equation 1.12 in the Fourier space by calculating the matrix elements of the Hamiltonian operator $\hat{\Theta}_H$ on the plane-wave basis. The result is

$$\sum_{\mathbf{G}',\sigma'} \mathcal{H}^{\sigma,\sigma'}_{\mathbf{G},\mathbf{G}'} c_{\sigma'}(\mathbf{k}+\mathbf{G}') = \frac{\omega^2}{c^2} c_\sigma(\mathbf{k}+\mathbf{G}), \tag{1.47}$$

where the Hamiltonian matrix is

$$\mathcal{H}^{\sigma,\sigma'}_{\mathbf{G},\mathbf{G}'} = |\mathbf{k}+\mathbf{G}||\mathbf{k}+\mathbf{G}'|\eta_{\mathbf{G},\mathbf{G}'} \begin{pmatrix} \mathbf{f}_{\sigma_2}\cdot\mathbf{f}_{\sigma'_2} & -\mathbf{f}_{\sigma_2}\cdot\mathbf{f}_{\sigma'_1} \\ -\mathbf{f}_{\sigma_1}\cdot\mathbf{f}_{\sigma'_2} & \mathbf{f}_{\sigma_1}\cdot\mathbf{f}_{\sigma'_1} \end{pmatrix} \tag{1.48}$$

and the matrix $[\eta_{\mathbf{G},\mathbf{G}'}] = [\varepsilon_{\mathbf{G},\mathbf{G}'}]^{-1}$ is the inverse of the dielectric function Fourier transform

$$\varepsilon_{\mathbf{G},\mathbf{G}'} = \frac{1}{V_c}\int_{V_c} \varepsilon(\mathbf{r}) e^{\imath(\mathbf{G}-\mathbf{G}')\cdot\mathbf{r}} d\mathbf{r}, \tag{1.49}$$

with V_c is the volume occupied by the unit cell.

The matrix $[\mathcal{H}]$ is a square matrix with dimensions $2M \times 2M$, while $[\eta]$ and $[\varepsilon]$ have dimensions $M \times M$, with M the number of vectors $\mathbf{G}$ below the cut-off. Likewise the operator $\hat{\Theta}_H$, also $\mathcal{H}$ is Hermitian with non-negative eigenvalues.

The equation 1.48 is the eigenproblem for $[\mathcal{H}]$. Standard numerical diagonalization of $[\mathcal{H}]$ yields the eigenfrequencies $\omega_n(\mathbf{k})$ and, optionally, the coefficients $c_n(\mathbf{k}+\mathbf{G})$. For each diagonalization, the routine outputs a set $\omega_n(\mathbf{k})$, with $n = 1, \ldots, 2M$, corresponding to the energies of $2M$ bands for a fixed Bloch vector $\mathbf{k}$. In order to calculate the whole band structure, the operation has to be repeated for a certain set of $\mathbf{k}$ vectors in the BZ, usually the edges of the irreducible BZ.

The truncation of the sum in Eq. 1.46 is the trick that allowed numerical solution of the master equation. In fact, the exact Fourier transform of the operator $\hat{\Theta}_H$ would be a matrix of infinite dimensions, whereas $[\mathcal{H}]$ is limited to $2M \times 2M$. For this reason, the matrix eigenvalue problem is an approximation of Maxwell's equations and an error will occur in the calculated eigenfrequencies. Calling $\lambda_n(\mathbf{k})$ the true eigenvalue and $\lambda_n^{(M)}(\mathbf{k})$ the eigenvalue calculated with the numerical routine, the error committed in evaluating the band energies will be $\Delta_n^{(M)}(\mathbf{k}) = |\lambda_n(\mathbf{k}) - \lambda_n^{(M)}(\mathbf{k})|$. As $M \to \infty$, the matrix $[\mathcal{H}]$ approach the true Fourier transform of $\hat{\Theta}_H$ and, consequently, the band energies should converge to the true values.

The core of the problem is related to the Fourier transform of the dielectric function $\varepsilon_r(\mathbf{r})$, which is into the operator $\hat{\Theta}_H$ as $\varepsilon_r(\mathbf{r})$. Because of $[1/\varepsilon_r]^{(M)} \neq ([\varepsilon_r]^{(M)})^{-1}$, due to the jump discontinuities of the dielectric function at the interfaces among the media of the PhC, the convergence of the plane-wave expansion method is not a trivial problem.

The correct choice for uniform convergence is $[\eta] = [\varepsilon_r]^{-1}$ [13], which is called the inverse rule, because $[\varepsilon_r]^{-1}$ satisfied uniformly the boundary conditions for the electromagnetic field, while $[1/\varepsilon_r]$ does it only non-uniformly. With this choice, for 2D PhC, the error $\Delta_n^{(M)}(\mathbf{k})$ is below 1% already with M of the order of 100.

The plane-wave expansion method with the inverse rule is thus able to output accurate eigenfrequencies with a moderate CPU time and a complexity of $O(M^3)$, due to the standard diagonalization and inversion routines.

Chapter 2

Two-dimensional Photonic Crystals

In the precedent chapter, it has been shown that the electromagnetic problem for a photonic crystal can be treated with the operator formalism, by recasting Maxwell's equations into a closed form for either the electric or the magnetic fields. The translational symmetry of the dielectric function implies that the solutions have to be Bloch waves. The frequency spectrum is organized in the band structure, with the classification of the energy levels in terms of Bloch vectors $\mathbf{k}$ and band index n. The band structure is obtained by numerical solution of the master equation by means of the plane-wave expansion method. Now we will apply these concepts and tools to the study of semiconductor-based two-dimensional photonic crystals and then of two-dimensional photonic crystal slabs. The chapter is mainly based on the works of L. C. Andreani and M. Agio [14].

2.1 2D Photonic Crystals

A 2D photonic crystal is characterized by a dielectric function periodic in a plane and homogeneous in the direction perpendicular to it (see Fig. 2.1). In other word, choosing a reference system xyz, the dielectric function is $\varepsilon_r = \varepsilon_r(x, y)$. The discussion will be focused on 2D photonic crystals with a triangular lattice of air holes in a semiconductor material. The band structure is calculated only for in-plane propagation, that is $\mathbf{k} = (k_x, k_y, 0)$. Nevertheless, many results are valid for 2D photonic crystals in general.

Figure 2.1 shows a top view of this photonic crystal and the correspondent BZ and irreducible BZ delimited by the symmetry lines T and Σ. The holes radius is

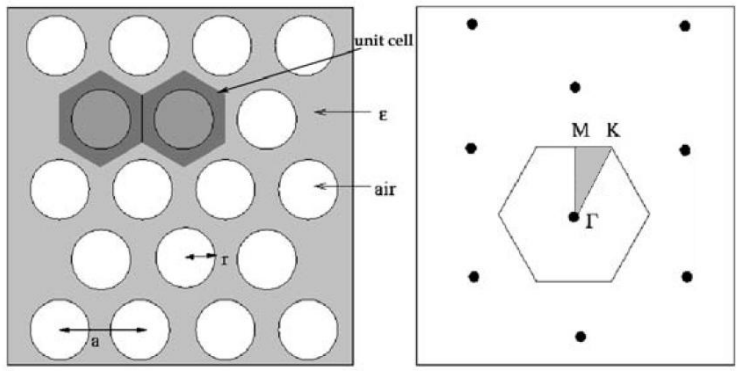

Figure 2.1: On the left, top view of a 2D photonic crystal made of a triangular lattice of period a, with air holes of radius r, in a dielectric medium with dielectric function ε. On the right, 2D reciprocal space and the hexagonal Brillouin zone with symmetry points and lines. The gray shaded area is the irreducible Brillouin zone.

r, the lattice constant a and ε_r the background dielectric function. A choice for the primitive vectors is

$$\begin{aligned} \mathbf{a}_1 &= a \cdot (1, 0) \\ \mathbf{a}_2 &= a \cdot (\frac{1}{2}, \frac{\sqrt{3}}{2}), \end{aligned} \tag{2.1}$$

and the area of the unit cell is $A_c = a^2 * \frac{\sqrt{3}}{2}$.

By using Eq. 1.29, the reciprocal-space primitive vectors are

$$\begin{aligned} \mathbf{g}_1 &= \frac{2\pi}{a} \cdot (1, -\frac{1}{\sqrt{3}}) \\ \mathbf{g}_2 &= \frac{2\pi}{a} \cdot (0, \frac{2}{\sqrt{3}}). \end{aligned} \tag{2.2}$$

We can rewrite the Maxwell's equations removing the dependence from z and obtain two independent sets of equations:

$$\begin{aligned} \frac{\partial}{\partial y} E_z(\rho, t) &= -\mu_0 \frac{\partial}{\partial t} H_x(\rho, t) \\ \frac{\partial}{\partial x} E_z(\rho, t) &= \mu_0 \frac{\partial}{\partial t} H_y(\rho, t) \\ \frac{\partial}{\partial x} H_y(\rho, x) - \frac{\partial}{\partial y} H_x(\rho, t) &= \varepsilon_0 \varepsilon_r(\rho) \frac{\partial}{\partial t} E_z(\rho, t), \end{aligned} \tag{2.3}$$

and

$$\begin{aligned}
\frac{\partial}{\partial y}H_z(\rho,t) &= \varepsilon_0\varepsilon_r(\rho)\frac{\partial}{\partial t}E_x(\rho,t)\\
\frac{\partial}{\partial x}H_z(\rho,t) &= -\varepsilon_0\varepsilon_r(\rho)\frac{\partial}{\partial t}E_y(\rho,t)\\
\frac{\partial}{\partial x}E_y(\rho,t) - \frac{\partial}{\partial y}E_x(\rho,t) &= -\mu_0\frac{\partial}{\partial t}H_z(\rho,t),
\end{aligned} \tag{2.4}$$

where $\rho = (x, y)$ denotes the 2D position vector. Mixing the two sets of equations to eliminate H_x, H_y from Eq. 2.3, and E_x and E_y from Eq. 2.4, we obtain:

$$\frac{1}{\varepsilon_r(\rho)}\left[\frac{\partial^2}{\partial x^2}+\frac{\partial^2}{\partial y^2}\right]E_z(\rho,t) = \frac{1}{c^2}\frac{\partial^2}{\partial t^2}E_z(\rho,t) \tag{2.5}$$

$$\left[\frac{\partial}{\partial x}\frac{1}{\varepsilon_r(\rho)}\frac{\partial}{\partial x}+\frac{\partial}{\partial y}\frac{1}{\varepsilon_r(\rho)}\frac{\partial}{\partial y}\right]H_z(\rho,t) = \frac{1}{c^2}\frac{\partial^2}{\partial t^2}H_z(\rho,t). \tag{2.6}$$

As done in the general case, we seek for harmonic solution of these equations

$$E_z(\rho,t) = E_z(\rho,t)\mathrm{e}^{-\imath\omega t}, \qquad H_z(\rho,t) = H_z(\rho,t)e^{-\imath\omega t}. \tag{2.7}$$

Substituting these solutions into Eqs. 2.5 and 2.6, we obtain the master equation for 2D photonic crystal given by

$$\hat{\Theta}_E E_z(\rho) = \frac{1}{\varepsilon_r(\rho)}\left[\frac{\partial^2}{\partial x^2}+\frac{\partial^2}{\partial y^2}\right]E_z(\rho) = \frac{\omega^2}{c^2}E_z(\rho) \tag{2.8}$$

$$\hat{\Theta}_H H_z(\rho) = \left[\frac{\partial}{\partial x}\frac{1}{\varepsilon_r(\rho)}\frac{\partial}{\partial x}+\frac{\partial}{\partial y}\frac{1}{\varepsilon_r(\rho)}\frac{\partial}{\partial y}\right]H_z(\rho) = \frac{\omega^2}{c^2}H_z(\rho). \tag{2.9}$$

The two eigenfunctions defined by Eqs. 2.8 and 2.9 represent two different polarizations; the first is called transverse magnetic (TM) polarization, for which the electric field is parallel to the z axis, while the second one is called transverse electric (TE) polarization, for which the magnetic field is parallel to the z axis[1].

Switching to the Fourier space of the plane-wave expansion, the master equation is split into:

$$\begin{aligned}
\sum_{\mathbf{G}'}(\mathbf{k}+\mathbf{G})\cdot(\mathbf{k}+\mathbf{G}')\eta_{\mathbf{G},\mathbf{G}'}c_{\sigma_1}(\mathbf{k}+\mathbf{G}') &= \frac{\omega^2}{c^2}c_{\sigma_1}(\mathbf{k}+\mathbf{G}), \quad \text{TE modes},\\
\sum_{\mathbf{G}'}|\mathbf{k}+\mathbf{G}||\mathbf{k}+\mathbf{G}'|\eta_{\mathbf{G},\mathbf{G}'}c_{\sigma_2}(\mathbf{k}+\mathbf{G}') &= \frac{\omega^2}{c^2}c_{\sigma_2}(\mathbf{k}+\mathbf{G}), \quad \text{TM modes},
\end{aligned} \tag{2.10}$$

[1] The TE modes correspond to (E_z, E_y, H_z), while TM modes to (E_z, H_x, H_y), where the field components are functions of x, y only; the other components are zero. The nomenclature used here is the same of [1], but in literature, other nomenclatures are often found: H-modes for TE modes and E-modes for TM modes [4]; also p-modes for TE modes and s-mode for TM-modes [6].

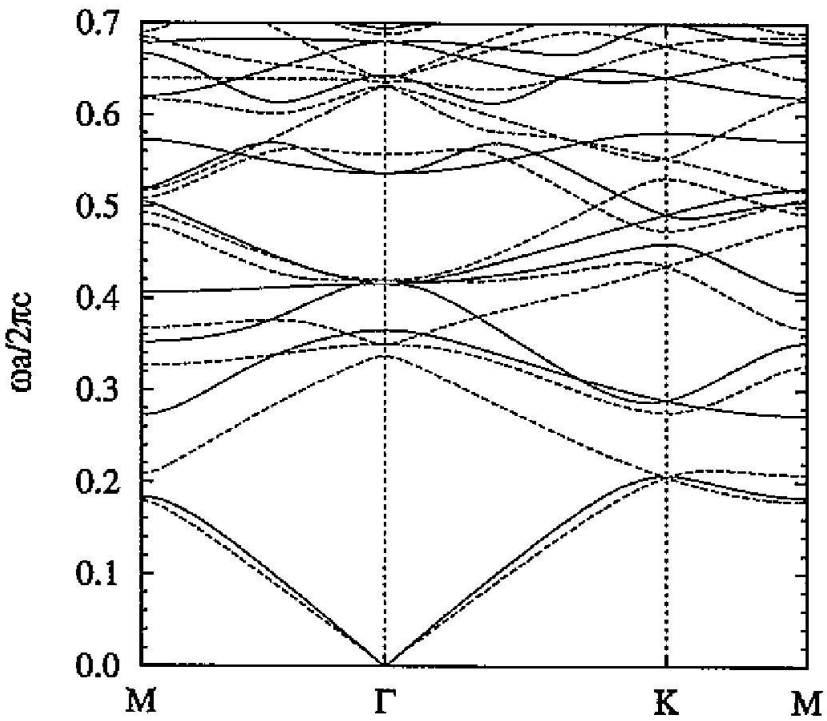

Figure 2.2: Photonic bands of a 2D photonic crystal made of a triangular lattice of air holes ($r = 0.3a$, in a dielectric medium ($\varepsilon_r = 12$). Solid (dashed) lines refer to TE modes (TH modes).

that leads to two different band structures one for the TE modes and one for the TM modes. Thus a 2D photonic crystal may show a bandgap just for only one polarization or for both polarizations. In the last case, the bandgap is called *complete*.

2.1.1 The band structure

The band structure is calculated along the symmetry lines of the Brillouin zone: Γ - K, Γ - M, and K - M. The $\mathbf{G}$ are constructed by linear combination of the reciprocal-space primitive vectors $\mathbf{g}_i$. The result of the integral in Eq. 1.49 is

$$\varepsilon_{\mathbf{G},\mathbf{G}'} = \begin{cases} (\varepsilon_{\text{air}} - \varepsilon_{\text{diel}}) \frac{2\pi r}{A_c G} J_1(Gr), & \text{if } \mathbf{G} \neq \mathbf{G}', \\ f\varepsilon_{\text{air}} + (1-f)\varepsilon_{\text{diel}}, & \text{if } \mathbf{G} = \mathbf{G}', \end{cases} \tag{2.11}$$

where $\varepsilon_{\text{air}} = 1$ is the air dielectric constant, $\varepsilon_{\text{diel}} = \varepsilon_r$ is the material dielectric function, $G = |\mathbf{G} - \mathbf{G}'|$, $J_1(x)$ is the first order Bessel function, and $f = \pi r^2 / A_c$ is the air filling factor.

Figure 2.2 shows the photonic band structure calculated for air holes with radius $r = 0.3a$, in a dielectric medium with $\varepsilon_r = 12$. The system exhibits a photonic bandgap only for the TE modes (solid lines). For TM-modes (dashed lines), the bandgap is closed by the second band. Notice that the first bands of both TE-modes and TM-modes have linear dispersion for $\omega \to 0$, that is the long wavelength limit. The TE-modes and TM-modes dispersions have different slope for $\omega \to 0$; this means that the two modes have different effective dielectric function. The effective dielectric function for TM-modes is given by the analytical formula

$$\varepsilon_{\text{eff}} = f\varepsilon_{\text{air}} + (1-f)\varepsilon_{\text{diel}} = \varepsilon_{\mathbf{G},\mathbf{G}'}. \tag{2.12}$$

The effective dielectric function for TE-modes does not have an analytic expression. Effective medium theory gives that its value is comprised between the Maxwell-Garnett bound

$$\varepsilon_{\text{eff}} = \varepsilon_{\text{diel}} \left(1 + \frac{2f\alpha}{1-f\alpha}\right), \tag{2.13}$$

where $\alpha = (\varepsilon_{\text{air}} - \varepsilon_{\text{diel}})/(\varepsilon_{\text{air}} + \varepsilon_{\text{diel}})$ is the depolarization factor, and the inverse Maxwell-Garnett bound, obtained by interchanging the filling fractions, f and $1-f$, and the dielectric functions ε_{air} and $\varepsilon_{\text{diel}}$ in the Maxwell-Garnett bound.

The correct value can be calculated numerically [6][15][7]. Thus, in the long-wavelength limit, a two-dimensional photonic crystal behaves like an homogeneous uniaxial crystal[2], where the optical axis is along the z direction and the dielectric functions $\varepsilon_{||}$ and $\varepsilon_{\perp}$ are the effective values for TM and TE modes respectively. For two-dimensional photonic crystals $\varepsilon_{||} > \varepsilon_{\perp}$ always. The effective dielectric tensor reads

$$\varepsilon = \begin{pmatrix} \varepsilon_{\perp} & 0 & 0 \\ 0 & \varepsilon_{\perp} & 0 \\ 0 & 0 & \varepsilon_{||} \end{pmatrix} \tag{2.14}$$

For finite frequencies the photonic crystal effects become important and the mean field approximation is more complicated [6]. Nevertheless, it is still meaningful to speak in terms of effective dielectric function as the zero-th term in a perturbative expansion of the band structure [16].

Looking again at Fig. 2.2, it is found that TE-modes have a photonic band gap also around $\omega a/2\pi c \approx 0.6$. However, the band gaps lying at higher frequencies are

[2] That is true for the square and the triangular lattices. For lattices with a lower symmetry the crystal is biaxial, with two effective dielectric functions for TE-modes [15].

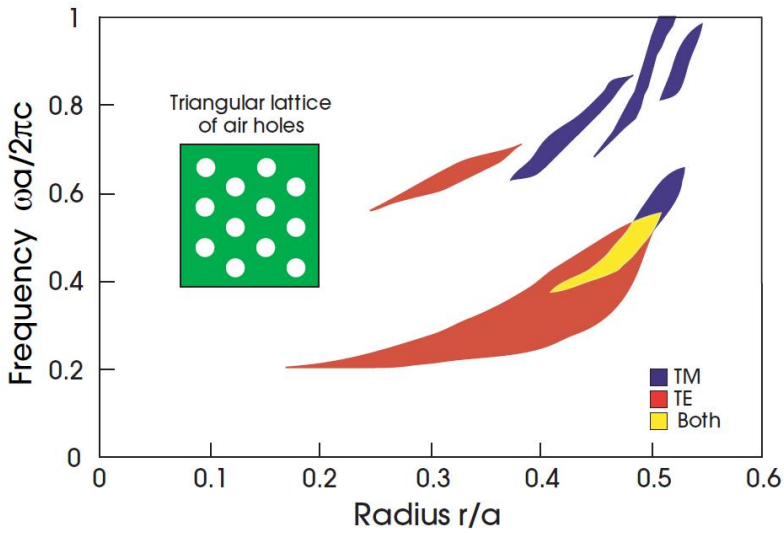

Figure 2.3: Gap map for a photonic crystal with triangular lattice from [1]. A complete photonic band gap opens for $0.41a < r < 0.5a$ (yellow area).

more sensitive to disorder, contrary to the first band gap at $\omega a/2\pi c \approx 0.25$. Indeed, for the higher bands, the coefficients $c_\sigma(\mathbf{k}+\mathbf{G})$ with large $\mathbf{k}+\mathbf{G}$ vectors have a stronger weight in the plane-wave expansion, contrary to what happens for the lower bands.

Disorder primarily affects the coefficients with large $\mathbf{k}+\mathbf{G}$ vectors, because they correspond to plane waves with short wavelength, more sensitive to roughness and other irregularities. Since disorder is practically unavoidable in real samples, it is important to devise photonic crystals where the desired properties are robust [17].

It has been shown that the band structure of Fig. 2.2 exhibits band gaps only for TE-modes. However, this is true only for particular choice of r and ε. It is interesting to see what happens if one of the two parameters is varied. In theory, one could change the dielectric function ε, but in practice, its value is determined by the choice of the material, which is the most important parameter. For the most common semiconductor-based photonic crystals (Si, GaAs, InP), ε is within [11, 12]. For this reason, only the hole radius is considered as a free parameter.

2.1.2 Gap Maps

The existence of a complete photonic band gap is one of the most attracting features of photonic crystals. If one wants to know whether a structure has a full

band gap, or simply locates the band gaps for each polarization, it would be necessary to examine a large number of band structures, one for a given value of the hole radius r. It turns out, that is more convenient and clear to visualize only the edges of the photonic band gap as a function of r in the the so-called gap map. Fig. 2.3 shows the band gaps for the parameters of Fig. 2.2, with r/a varying from 0 to 0.5, which corresponds to the closed-packed condition. There is a wide band gap for TE-modes (solid lines) that opens for $r > 0.17a$ and increases with the hole radius until it reaches the maximum value for $r \approx 0.45a$. Another band gap for TE-modes occurs for a smaller range of r and at higher frequencies. This is the second gap seen in the band structure of Fig. 2.2, where $r = 0.3a$.

Concerning the other polarization (dashed lines), the lowest frequency band gap is located around $r = 0.45a$, with a steep profile that covers the frequency range $\omega a/2\pi c \approx 0.35 - 0.6$. Smaller band gaps appear at higher frequencies for $r \approx 0.4a$. The map of the complete band gap is determined by the intersection of the TE-modes band gaps with the TM-modes band gaps. This happens only for $r > 0.41a$ in the frequency window $\omega a/2\pi c \approx 0.35 - 0.55$ (gray shaded area). It is worth to mention that the gap edges shift towards higher frequencies as the radius increases, in accordance to the reduction of the effective dielectric constants $\varepsilon_{\parallel}$ and $\varepsilon_{\perp}$.

In order to obtain a complete photonic band gap in this system, it is necessary to have a high air fraction. Such condition might be critical from the experimental point of view, because of intrinsic limits in the fabrication process. In fact, it would be difficult to reach high aspect ratios with hole walls as thin as membranes. The alternative is to release the requirement of a full band gap and to work with a partial band gap using polarized light. For a two-dimensional photonic crystal of air holes in a semiconductor one finds convenient to exploit the wide band gap given for TE-polarization.

2.2 2D Photonic Crystal Slab

A two-dimensional photonic-crystal slab is made of a planar dielectric waveguide that is deeply etched according to a two-dimensional pattern. In other words, the dielectric function is periodic in the $x - y$ plane and is a step-wise function in the vertical direction z: $\forall R \in \mathbb{V},\ \forall z \in \mathbb{R},\ \varepsilon_r(\mathbf{x} + \mathbf{R}, z) = \varepsilon_r(\mathbf{x}, z)$, with $\mathbf{x} = (x, y)$ and $\mathbb{V}$ is the vector space associated to the two-dimensional lattice. The number of parameters involved in the characterization of these systems is large: the structure of

the planar waveguide (layers, thicknesses, dielectric functions), the two-dimensional photonic crystal (lattice and unit cell) and the etch depth. Nevertheless, there are few representative cases that are able to address all the important features pertaining to two-dimensional photonic-crystal slabs. Since the attention is focused on the effects due to the planar waveguide, the photonic crystal pattern is chosen una tantum as a triangular lattice of air holes. At this stage, the etch depth is considered as infinite, the cladding layers above and below the core are equal.

Fig. 2.4 gives examples of planar waveguides patterned with a triangular lattice of air holes. The thickness of the core layer is d, whereas the cladding layers are considered as semi-infinite. The low panels display three types of planar waveguide: (d) a dielectric self-standing membrane, also known as air bridge, (e) waveguide based on a semiconductor heterostructure, for instance a GaAs/AlGaAs system, (f) waveguide with strong asymmetry, like a silicon-on-insulator wafer. The air bridge is a typical strong-confinement waveguide, while the GaAs/AlGaAs system belongs to the weak confinement case; both waveguides are symmetric.

The photonic band structure of these systems is more complicated than for ideal two-dimensional photonic crystals, because of the finite-height of the two-dimensional pattern. For symmetric waveguides, the modes are still even or odd with respect to the mid-plane of the core layer. However, they are not TE-modes or TM-modes anymore, because the fields are also function of the z coordinate. Nevertheless, it makes sense to call them TE-like modes or TM-like modes. For asymmetric waveguides such separation breaks down and the band structure has to be calculated by solving the master equation with all the transverse field components. However, the main complication with respect to two-dimensional photonic crystals consists of the so-called *light-line problem* and of the existence of Bloch modes with a cut-off. In fact, these structures support two kinds of modes. If the waveguide thickness is not too small, guided modes exist whose energies lie below the light line of the cladding material (or light lines, if the waveguide is asymmetric). An example of a band structure for these kind of systems is displayed in figure 2.5.

The modes below the light line are true stationary Bloch modes and, ideally, they are not subject to propagation losses. Above the light line of the cladding material, the spectrum becomes a continuum of states with resonances called quasi-guided modes. Since these modes lie within the leaky modes of the waveguide, they exhibit intrinsic propagation losses due to out-of-plane diffraction. Moreover, the planar waveguide can be single mode or multi-mode in the frequency region of interest. If

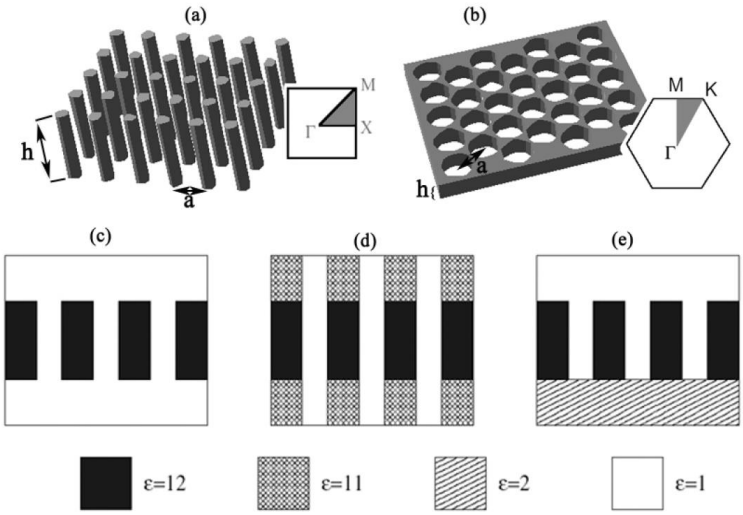

Figure 2.4: Upper panels: (a) slab photonic crystal of thickness h patterned with a square lattice of dielectric rods, (b) slab photonic crystal of thickness h patterned with a triangular lattice of air holes. Lower panels: (c) strong-confinement symmetric waveguide, i.e. patterned self-standing dielectric membrane (air bridge), (d) weak-confinement symmetric waveguide (e.g. patterned AlGaAs-GaAs-AlGaAs system), (e) patterned asymmetric waveguide (e.g. silicon-on-insulator). The values of the dielectric function given here are reasonable, because for typical semiconductor, ε is within [11, 12].

the waveguide is multi-mode, there will be Bloch waves with a cut-off corresponding to the onset of a higher-order mode in the planar waveguide. All of these concepts appear in the photonic band structure.

There are mainly four numerical methods that solve Maxwell's equations for two-dimensional photonic-crystal slabs: the plane-wave expansion method, with a super-cell in the vertical direction that accounts for the waveguide [18], the finite-difference time-domain (FDTD) method [19], the scattering matrix method [20], and magnetic field expansion method [14]. Each one has its advantages and its flaws. In particular, the plane-wave expansion method with the super-cell is limited to energies below the light line; the finite-difference time-domain method is time consuming and less accurate than frequency-domain methods; the scattering matrix method does not directly outputs the band structure; in the last one, the photonic band structure is calculated by expanding the magnetic field in the basis of guided modes of the planar waveguide, where each layer is taken to have an average dielectric function.

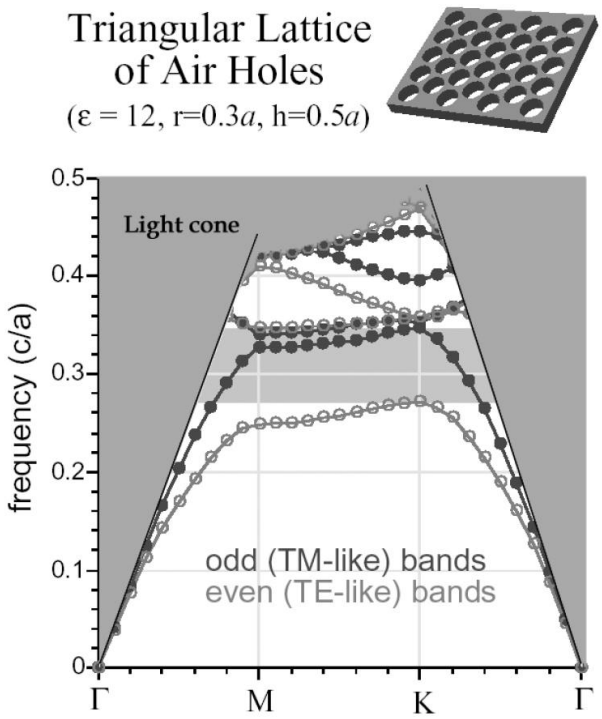

Figure 2.5: Projected band diagram for a photonic crystal slab of air holes in dielectric. The gray shaded region is the light cone: the projection of all states that can radiate in air. Black/gray lines denote guided modes (confined to the slab) that are even/odd with respect to the horizontal mirror plane of the slab, whose polarization is TE-like/TM-like, respectively. The bandgap is present only for the TE-like modes.

The approach goes beyond the nearly-free approximation of Ochiai [21], since no perturbative assumption is required, and it is valid also for strong modulation of the dielectric function.

2.2.1 The Band Structure

The photonic band structure of photonic-crystal slabs is characterized by the light-line problem, which discriminates between guided modes and quasi-guided modes. This is one of the main novelties with respect to conventional photonic crystals. Moreover, it has been mentioned that there can exist Bloch waves with a cut-off, which depends on the waveguide geometry. The structure of the dielectric matrix $[\varepsilon]$ is the origin of propagation losses in photonic crystal slabs. When a guided mode is folded, it crosses the air light line and enters the leaky mode region.

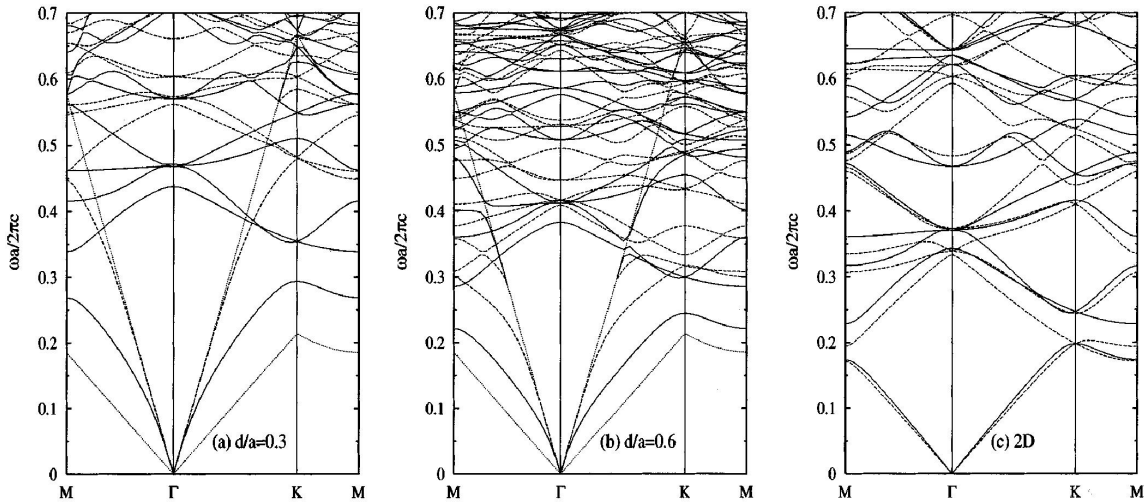

Figure 2.6: Photonic bands for an air-bridge structure, with hole radius $r = 0.24a$. (a) Waveguide thickness $d = 0.3a$; (b) waveguide thickness $d = 0.6a$; (c) ideal 2D case. Solid (dashed) lines represent modes that are even (odd) with respect to the xy mirror plane. The dotted lines in (a) and (b) refer to the light lines in air and in the effective waveguide material.

However, the mode remains truly guided, because the coupling with leaky modes is null, since the dielectric tensor of the effective waveguide is diagonal. Below the light line, the photonic band structure is made of guided Bloch states, which may form a photonic band gap. Once the Bloch mode has crossed the light line, even if it is calculated as a state with zero line-width, in fact, it becomes a resonance, due to the non-zero off-diagonal elements of the dielectric matrix $[\varepsilon]$, which couple the Bloch mode to the external field. Therefore, these states are subject to intrinsic propagation losses. The physical process that causes losses, is thus diffraction, since states with different $\mathbf{G}$ vectors are coupled by the off-diagonal elements of $[\varepsilon]$, and the origin of diffraction is the periodicity of the dielectric function.

The spectrum is a continuum of states and the photonic band picture seems to break down. However, assuming that above the light line, the dispersion relation of photonic crystal slabs is not a mere continuum of states, but it is organized in resonances, with central frequency and width well defined, the photonic band picture is still valid. In summary, the photonic bands lying below the light line represent the dispersion of guided modes, while those above the light line represent the dispersion of resonances. The photonic band picture is valid also for modes above the light line, provided that the structure is properly designed [22].

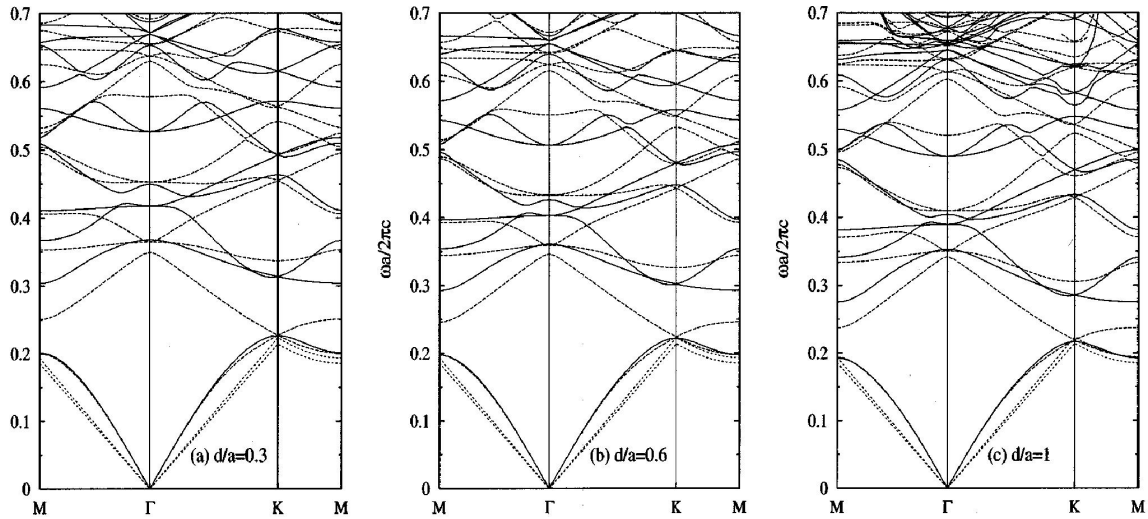

Figure 2.7: Photonic bands for an SOI structure, with hole radius $r = 0.24a$. (a) Waveguide thickness $d = 0.3a$; (b) $d = 0.6a$; (c) $d = 1.0a$. Solid (dashed) lines represent modes that are even (odd) with respect to the xy mirror plane. The dotted lines refer to the light lines in the effective core and cladding materials.

The concept of photonic band gap needs to be redefined in a 2D photonic crystal slab, because if we consider states just the guided modes it is not characterized by a null density of states. In Eq. 1.31 the sum is performed over the whole Brillouin zone, which includes the leaky mode region, so considering that above the light line the states are organized in resonances, we can define the photonic band gap as the spectral region $[\omega_1, \omega_2]$ for which $\forall\omega \in [\omega_1, \omega_2], \nexists\, (\mathbf{k}, n) : \omega = \tilde{\omega}_n(\mathbf{k})$, where $\tilde{\omega}_n(\mathbf{k})$ is either a guided mode or a resonance.

2.2.2 Vertical Confinement Effects

Going back to the structures of Fig. 2.4, it is important to study the two most representative systems: the strong confinement waveguide (air bridge, Fig. 2.4c) and the weak confinement waveguide (AlGaAs/GaAs/AlGaAs, Fig. 2.4d). The pattern is a triangular lattice of air holes (Fig. 2.4b). The aim is to see the dependence of the photonic band structure on the waveguide thickness d and on the hole radius r for both weak and strong confinement cases. The band structure is calculated along the symmetry lines of the two-dimensional Brillouin zone. Since these systems are symmetric, the bands are classified in TE-like modes and TM-like modes.

Bands

Fig. 2.6 shows the photonic band structure of the air bridge for a hole radius $r = 0.24a$ and waveguide thickness $d = 0.3a,\ 0.6a$, compared with the ideal two-dimensional case. The bands of the two-dimensional system, Fig. 2.6c, exhibit a photonic band gap between the first and second band for even modes (TE-modes). The bands of the photonic crystal slab fall partly in to the guided mode region, where they agree with those calculated by Johnson, S. C., et at. (1999), and partly in the leaky mode region, where they must be viewed as resonances. For thickness $d = 0.3a$ (see Fig. 2.6a), the lowest bands are qualitatively similar to their two-dimensional counterpart, but they are also strongly blue-shifted due to field confinement in the z direction. The gap in the TE modes opens between $\omega a/2\pi c \approx 0.29 - 0.34$, while it is located between 0.2 and 0.23 in the two-dimensional case. The confinement effect is stronger for odd modes. In the long-wavelength limit, the waveguide behaves as a uniaxial medium, with $\varepsilon_{||} \equiv \varepsilon_{zz}$, given by Eq. 2.12 and being larger than $\varepsilon_{\perp} \equiv \varepsilon_{xx} \equiv \varepsilon_{yy}$, approximated by Eq. 2.13. In the two-dimensional case, odd modes have the electric field along z and feel the largest dielectric constant $\varepsilon_{||}$: hence they are better confined in the waveguide and have a larger blue-shift compared to even modes.

The six photonic modes at the point Γ in each polarization can be interpreted as the fundamental waveguide mode at the lowest non-zero reciprocal lattice vectors, folded in the Brillouin zone and split by the dielectric matrix. Notice that the in the photonic crystal slab with $d = 0.3a$, the modes up to $\omega a/2\pi c \simeq 0.57$ can be put in one-to-one correspondence with the bands of the two-dimensional case, indicating that the waveguide is single mode. A second-order waveguide mode appears above $\omega a/2\pi c \simeq 0.57$. Analogous considerations hold for the case of waveguide thickness $d = 0.6a$, where the field confinement is less pronounced. Moreover, a second-order waveguide mode starts at $\omega a/2\pi c \simeq 0.3$ and the bands at higher frequencies become more complex.

The example allows to discuss the trend with waveguide thickness with fixed hole radius $r = 0.24a$. For a small value of d/a, the waveguide is single mode in a wide frequency range and the photonic bands can be interpreted as two-dimensional bands blue-shifted by the field confinement. The confinement is stronger for odd modes. By increasing the ratio d/a, the blue-shift is reduced and a second-order waveguide mode occurs with decreasing cut-off frequency. For $d > 0.6a$, the second-order mode falls into the gap of even modes. When defects are present in the band

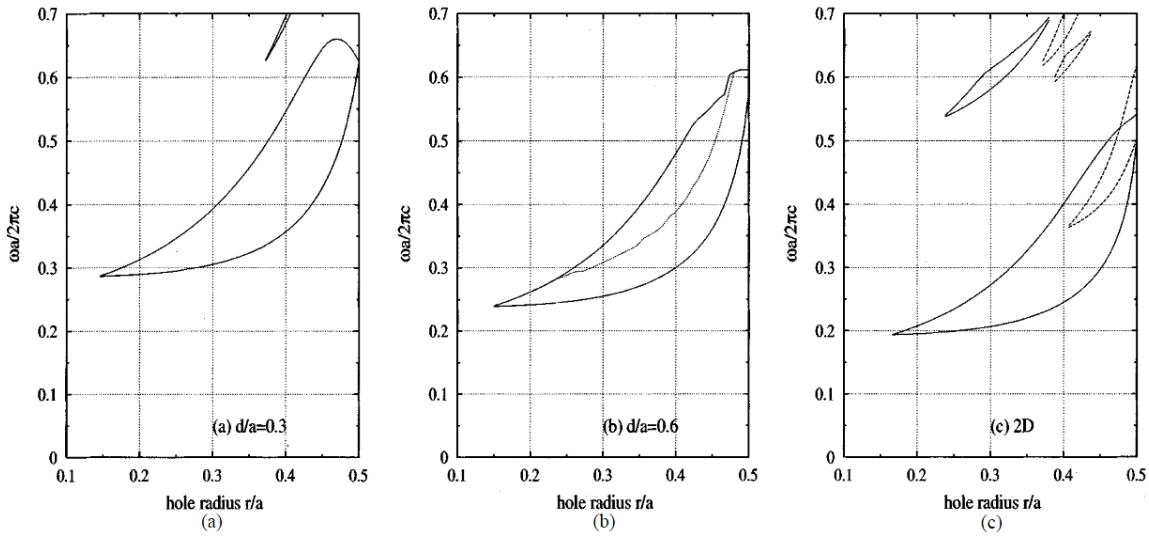

Figure 2.8: Gap maps for the air bridge structure. (a) Waveguide thickness $d = 0.3a$; (b) waveguide thickness $d = 0.6a$; (c) ideal 2D case. Solid (dashed) lines represent the edges of photonic bands that are even (odd) with respect to the xy mirror plane. The dotted line in (b) refers to the cut-off of the second-order waveguide mode[14].

gap, the presence of the second-order mode will contribute to losses. Concerning low-loss wave propagation , it is better to have structures that are single mode in the frequency range of interest. For the air bridge system, small values of d/a are more favorable.

Fig. 2.7 displays the photonic bands for an SOI structure (Fig. 2.4d) for three values of waveguide thickness. Due to the small dielectric contrast between core and cladding, there are no truly guide modes and all photonic modes lie in the radiative region. The dispersion of quasi-guided modes is very similar to the two-dimensional case of Fig. 2.6c and the blue-shift is much less than for the air bridge. However, it is noticeable that the gap in the even modes is increased compared to the two-dimensional case. The three patterned waveguides are single mode for the shown frequency range, except for $d = a$, where a second-order mode occurs for $\omega a/2\pi c \simeq 0.65$. Like for the strong confinement case, the results of Fig. 2.7 suggest that, in order to maximize the even gap, it is more convenient to use small values of waveguide thickness.

Gap Maps

It is also interesting to see the trends of the band gaps with the hole radius. Fig.

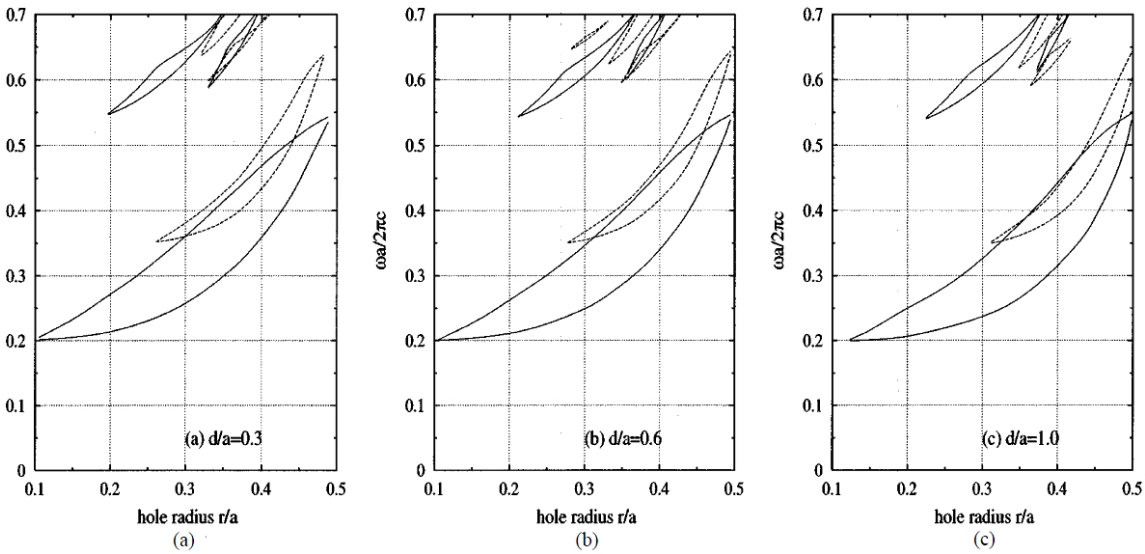

Figure 2.9: Gap maps for the SOI structure. (a) Waveguide thickness $d = 0.3a$; (b) $d = 0.6a$; (c)$d = 1.0a$. Solid (dashed) lines represent the edges of photonic bands that are even (odd) with respect to the xy mirror plane[14].

2.8 displays the gap maps as a function of hole radius for the air bridge structure of Fig. 1.9d with waveguide thickness d = 0.3a, 0.6a and in the two-dimensional case. The purpose of Fig. 2.8c is to set a reference for the gap maps in a photonic crystal slab. The gap map of the two-dimensional case has already been discussed in Sec. 2.2.2. From Fig. 2.8a,b, it is possible to see that there are no gaps in the odd modes (dashed lines) for any hole radius and, therefore, no complete band gap. The band gap for even modes (solid lines) occurs at higher frequencies than in two-dimensions, because of the vertical confinement. It has to be remarked that the upper edge of the gap lies in the radiative region for a hole radius larger than about $0.4a$ so that the even gap is formed partly in the guided mode region and partly in the leaky mode region.

Fig. 2.9 shows the gap maps for the SOI structure, with photonic crystal thickness $d = 0.3a, 0.6a, a$. They are rather similar to the two-dimensional case, because the confinement effect is much less important than for the air bridge. It has to be pointed out that a weak-confinement structure, as SOI structure, has no truly guided modes in the considered range of crystal thicknesses: all modes are resonances and the photonic band gap lies entirely in the radiative region. Notice that, on decreasing the thickness, the gap for odd modes opens at smaller values of the hole radius; the same happens for the even gap. Contrary to the strong confinement waveguide, as

a membrane, full band gap common to both polarizations still exists and it occurs even for hole radii of the order of $0.3a$, if waveguide widths $d \sim 0.3a$ are used.

2.2.3 Conclusions

The concept of photonic band structure and of photonic band gap have been extended, in order to account for the existence of quasi-guided modes in the radiative region. For strong-confinement waveguides (air bridge), the photonic modes exhibit a large blue-shifted with respect to the two-dimensional case.

The gap maps of the air bridge display only a gap for even modes. The even gap remains large even for small waveguide thickness, while it is closed by a second-order waveguide mode when the thickness reaches $d = 0.6a$. In the weak confinement waveguide (GaAs/AlGaAs system), the bands are similar to the two-dimensional case. However, the single gaps and the complete band gap open for smaller values of the hole radius. Another difference between strong and weak confinement waveguides regards the nature of photonic modes. While strong confinement waveguides support both guided and quasi-guided modes, weak confinement waveguides has practically only quasi-guided modes. These modes are subject to propagation losses, because of the coupling to the external field. Understanding and quantifying out-of-plane losses is very important, since they may preclude the use of photonic crystal slabs towards integrated photonic crystals circuits. One would like to know which is the optimal waveguide design that accounts for minimal out-of-plane losses, ease of fabrication with lithographic methods and appropriate band gap properties. An air bridge system allows to operate with truly guided modes; on the other hand, it is more difficult to fabricate.

Two-dimensional photonic crystals embedded in weak confinement waveguides possess a band structure that is more similar to the two-dimensional case and they can be obtained with top-down processes much easily than suspended membranes. These features make weak confinement systems more promising than the strong confinement counterpart, provided they exhibit “small” propagation losses [23].

Chapter 3

Two-dimensional Photonic Crystal Waveguides

The photonic band gap is so much attracting because of the capability to control wave propagation, but it is possible to create energy levels within it by designing defects. Considering the plane of periodicity of two-dimensional photonic crystals, a point defect corresponds to a resonant cavity, while a linear defect corresponds to a waveguide. Resonant cavities and waveguides are among the building blocks of photonic integrated circuits.

In this chapter, we will focus on waveguides realized as linear defects in a two dimensional photonic crystal. A linear defect preserves the periodicity in one dimension, yielding a one dimensional Brillouin zone and a Bloch vector $\mathbf{k}$. Therefore, these defect states will obey to a dispersion relation $\omega = \omega_m(\mathbf{k})$, where m is the order of the guided mode.

The simpler way to realize a linear defect [1][24] is to remove N adjacent rows of holes in a photonic crystal made of a triangular lattice of air holes in a dielectric material. The so-called WN waveguide, where N is the number of removed rows, is usually created along the $\Gamma - K$ direction, rather than the $\Gamma - M$, because the waveguide walls are smoother. The width of a WN waveguide is $w = a\sqrt{3}(N+1)/2$. The guides with odd N (W1,W3,...) have symmetric boundaries, while those with even N (W2, W4, ...) have boundaries shifted by $a/2$ with respect to each other [25]. Usually, waveguides with odd N are used, because they are symmetric with respect to their axis.

The presence of the waveguide breaks the periodicity along $\Gamma - M$. Nevertheless,

the system remains periodic along $\Gamma - K$, with lattice constant a, so that the Bloch theorem applies. There are several efficient numerical techniques for calculating the dispersion relation of the guided modes. In the next sections, we will present the two ones that will be used in this work: the *super-cell* method [25] and the *Finite-Difference Time-Domain* (FDTD) method [26].

3.1 The Super-Cell Method

Consider a WN waveguide. For simplicity we do not consider the height dimension. A unit cell of the waveguide is a section of the waveguide with a length equal to the period a of the photonic crystal along the propagation direction and unlimited along the other direction. The super-cell method consists of assuming a periodic array of waveguides, spaced by bulk photonic crystal, whose unit cell corresponds to the one just mentioned, but limited along the direction perpendicular to the Bloch vector (see the right panel of Fig. 3.3). The spacing is determined by the width of the super cell. A guided mode is characterized by an evanescent field in the direction perpendicular to the Bloch vector. For this reason, if the super-cell is sufficiently large, the guided modes of adjacent unit cells will not overlap (no interaction) and the dispersion relation will be like that one of a single waveguide. The array of waveguides is characterized by two primitive vectors $\mathbf{a}_1$, $\mathbf{a}_2$. Even if the Brillouin zone is two-dimensional, only the Bloch vector along the waveguide axis represents the true guided-mode wave-vector. Given the unit cell, the reciprocal primitive vectors and the Bloch vector, the dispersion relation is calculated by the usual plane-wave expansion method.

While the primitive vectors are easily found by looking at the super cell:

$$\mathbf{a}_1 = a \cdot (1, 0), \qquad \mathbf{a}_2 = a\sqrt{3}(0, (N+1)/2 + K), \tag{3.1}$$

where N is for WN and $2K + 1$ is the number of photonic-crystal rows between two waveguide channels, the dielectric matrix $\|\varepsilon\|$ of the unit cell is more difficult to calculate. The dielectric function inside the super cell can be written as

$$\varepsilon(\mathbf{x}) = \varepsilon_{diel} + (\varepsilon_{air} - \varepsilon_{diel}) \sum_{\mathbf{v}} \theta(|\mathbf{x} - \mathbf{v}| - r), \qquad \mathbf{x} \in \text{ unit cell}, \tag{3.2}$$

where r is the hole radius, $\mathbf{x} = (x, y)$, $\mathbf{v}$ are the displacement vectors, and $\theta(x)$ is the Heaviside function. Using this expression, the Fourier transform of the dielectric

function can be expressed as the bulk Fourier transform multiplied by a structure factor,

$$\varepsilon_{\mathbf{G},\mathbf{G}'} = \begin{cases} S(\mathbf{G}-\mathbf{G}')F(\varepsilon_{air},\varepsilon_{diel},r,G), & \text{if } \mathbf{G}\neq\mathbf{G}', \\ f'\varepsilon_{air}+(1-f')\varepsilon_{diel}, & \text{if } \mathbf{G}=\mathbf{G}', \end{cases} \tag{3.3}$$

where f' is the super-cell filling factor and $\mathbf{G},\mathbf{G}'$ are the reciprocal vectors of the super-cell lattice, and $G=|\mathbf{G}-\mathbf{G}'|$.

The two function

$$S(\mathbf{G}) = A_c/A\sum_{\mathbf{v}} \mathrm{e}^{i\mathbf{G}\cdot\mathbf{v}}, \qquad F(\varepsilon_{air},\varepsilon_{diel},r,G) = (\varepsilon_{air}-\varepsilon_{diel})\frac{2\pi r}{A_c G}J_1(Gr), \tag{3.4}$$

with A the area of the super cell and A_c the area of the bulk crystal unit cell, are the structure factor and the atomic factor, corresponding to the dielectric-function Fourier transform of the bulk photonic crystal, respectively.

Once that the dielectric matrix has been calculated, Eqs. 2.10 can be used to find the dispersion relation of guided TE-modes and guided TM-modes, respectively. Since the waveguide is symmetric with respect to its axis, the guided modes can be further classified as even or odd with respect to a reflection plane σ_{xz}, where x is the waveguide axis and z is the vertical direction.

3.2 The FDTD Method

Finite-difference time-domain (FDTD) method dates back to the work of Yee [27], who proposed an algorithm for solving the time dependent Maxwell's curl equations, that transforms the differential operators in finite differences in space and time. It is considered easy to understand and easy to implement in software. Since it is a time-domain method, solutions can cover a wide frequency range with a single simulation run.

Considering the Maxwell's differential equations:

$$\nabla\times\mathbf{E}(\mathbf{r},t) = -\mu\frac{\partial}{\partial t}\mathbf{H}(\mathbf{r},t), \qquad \nabla\times\mathbf{H}(\mathbf{r},t) = \varepsilon\frac{\partial}{\partial t}\mathbf{E}(\mathbf{r},t), \tag{3.5}$$

we can see that the change in the E-field in time (the time derivative) is dependent on the change in the H-field across space (the curl). This results in the basic FDTD time-stepping relation that, at any point in space, the updated value of the E-field in time is dependent on the stored value of the E-field and the numerical curl of the local distribution of the H-field in space.

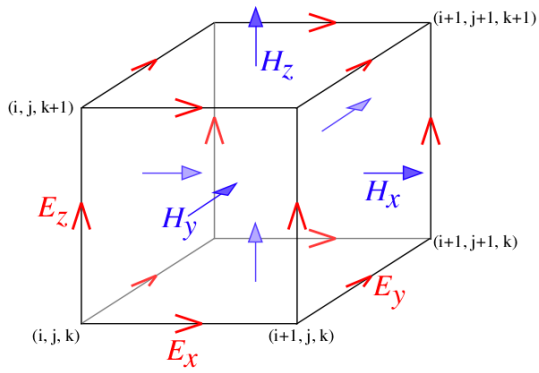

Figure 3.1: Illustration of a standard Cartesian Yee cell used for FDTD, about which electric and magnetic field vector components are distributed. Visualized as a cubic voxel, the electric field components form the edges of the cube, and the magnetic field components form the normals to the faces of the cube. A three-dimensional space lattice is comprised of a multiplicity of such Yee cells. An electromagnetic wave interaction structure is mapped into the space lattice by assigning appropriate values of permittivity to each electric field component, and permeability to each magnetic field component.

The H-field is time-stepped in a similar manner. At any point in space, the updated value of the H-field in time is dependent on the stored value of the H-field and the numerical curl of the local distribution of the E-field in space. Iterating the E-field and H-field updates results in a marching-in-time process wherein sampled-data analogs of the continuous electromagnetic waves under consideration propagate in a numerical grid stored in the computer memory.

This description holds true for 1-D, 2-D, and 3-D FDTD techniques. When multiple dimensions are considered, calculating the numerical curl can become complicated. Yee [27] proposed spatially staggering the vector components of the E-field and H-field about rectangular unit cells of a Cartesian computational grid so that each E-field vector component is located midway between a pair of H-field vector components, and conversely. This scheme, now known as a **Yee lattice**, has proven to be very robust, and remains at the core of many current FDTD software constructs.

Furthermore, Yee proposed a leapfrog scheme for marching in time wherein the E-field and H-field updates are staggered so that E-field updates are conducted midway during each time-step between successive H-field updates, and conversely. This

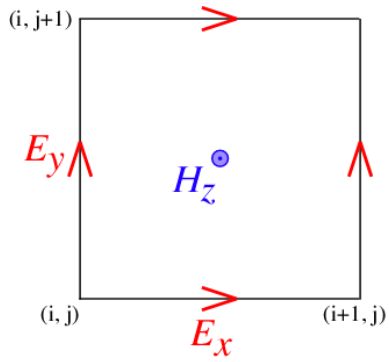

Figure 3.2: Yee lattice in 2D for the TE polarization.

explicit time-stepping scheme avoids the need to solve simultaneous equations, and furthermore yields dissipation-free numerical wave propagation, but it mandates an upper bound on the time-step to ensure numerical stability.

For simplicity, we will discuss in a deeper manner the FDTD method in two dimensions. Before proceeding, it is convenient to define the following notation for the finite differences. Time is discretized by division in uniform intervals Δt. The 2D space is defined on a discrete uniform rectangular mesh $x - y$. A space point in the mesh is denoted as

$$(i, j) = (i\Delta x, j\Delta y), \tag{3.6}$$

where Δx and Δy are the lattice space increments in the x and y directions, respectively, and $i,\ j$ are integers.

A function f of space and time evaluated at a discrete point in the grid and at a discrete point in time is denoted as

$$f(i\Delta x, j\Delta y, n\Delta t) = f\|^n_{i,j}. \tag{3.7}$$

We can define the partial space derivative of f at the fixed time $t_n = n\Delta t$:

$$\begin{aligned} \frac{\partial}{\partial x} f(i\Delta x, j\Delta y, n\Delta t) &= \frac{f\|^n_{i+\frac{1}{2},j} - f\|^n_{i-\frac{1}{2},j}}{\Delta x} + O[(\Delta x)^2] \\ \frac{\partial}{\partial y} f(i\Delta x, j\Delta y, n\Delta t) &= \frac{f\|^n_{i,j+\frac{1}{2}} - f\|^n_{i,j-\frac{1}{2}}}{\Delta y} + O[(\Delta y)^2] \end{aligned} \tag{3.8}$$

and the partial time derivative, evaluated at the grid point (i, j):

$$\frac{\partial}{\partial t} f(i\Delta x, j\Delta y, n\Delta t) = \frac{f\|^{n+\frac{1}{2}}_{i,j} - f\|^{n-\frac{1}{2}}_{i,j}}{\Delta t} + O[(\Delta t)^2], \tag{3.9}$$

where the $\pm 1/2$ increment in the several subscript of f represents a space or time finite difference. This notation is chosen to interleave the **E** and **H** components in time and space for implementing the so-called *leapfrog algorithm*.

This algorithm is stable if

$$\Delta t \leq \frac{1}{c\sqrt{\frac{1}{(\Delta x)^2} + \frac{1}{(\Delta y)^2}}}. \tag{3.10}$$

The computational domain is simply the physical region over which the simulation will be performed. The **E** and **H** fields are determined at every point in space within that computational domain. The material of each cell within the computational domain must be specified. Similarly, source and boundary conditions must be specified.

The Yee algorithm is second-order accurate. The accuracy can be improved by using smaller time and space increments. Even if the loop over the grid point is a $O(N^2)$ process, where N is the number of lattice points in the mesh, the whole algorithm is actually a $O(N^3)$ process, because the time stepping has to satisfy Eq. 3.10. For this reason, the three-dimensional version of the FDTD method is very much time consuming, with four nested loops.

3.3 The W1 waveguide

Given a WN waveguide, the best choice for the number of rows to remove depends on the device or application being developed. A narrow waveguide is likely to be single-mode, but it possesses higher propagation losses with respect to a larger waveguide, which, on the contrary, is likely to be multi-mode.

The W1 waveguide (one row removed) is the simplest linear defects waveguide and it is the choice of waveguide used in this work. Fig. 3.3 shows a W1 waveguide, which is created by removing one row of air holes along the $\Gamma - K$ direction of the triangular lattice, so that the width corresponds to $w = a\sqrt{3}$.

3.3.1 The Dispersion Relation

Fig. 3.4 shows the dispersion relation of the W1 channel waveguide of Fig. 3.3, with $w = a\sqrt{3}$, $r = 0.30a$ and $\varepsilon_{diel} = 12.25$, only for the guided TE-modes. Thin dotted lined correspond to the modes outside the photonic band gap (PBG) region, and they are guided in the bulk PhC and hence are not confined to the line defect.

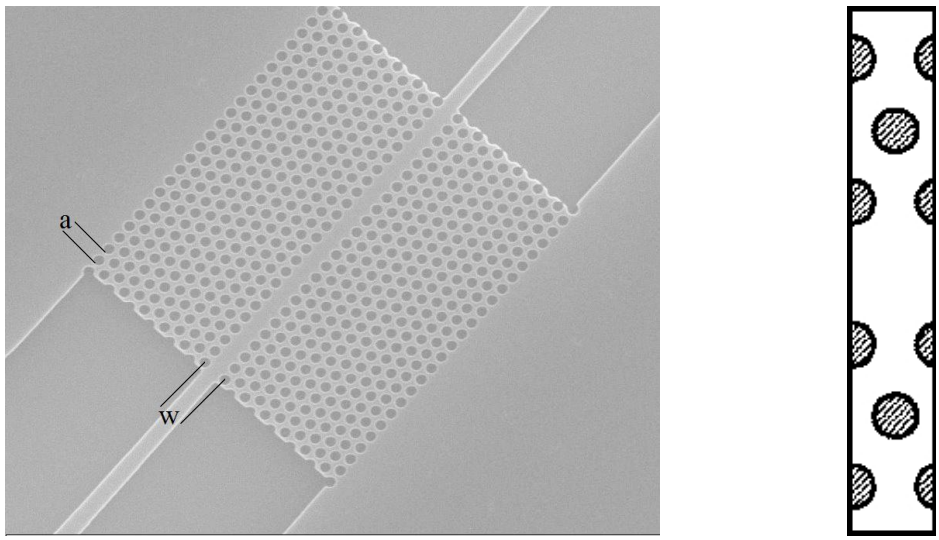

(a) (b)

Figure 3.3: (a) A 2D photonic crystal waveguide along the $\Gamma - K$ direction of a triangular lattice of air holes in a dielectric material, w defines the width of the waveguide, a is the lattice constant. (b) An example of super-cell for the calculation of the waveguide band diagram.

The modes at frequencies inside the PBG region can be separated by their lateral symmetry of magnetic field with respect to a plan along the propagation direction and vertical to even and odd modes. The even mode of such waveguides can be categorized with respect to their field distribution as *index guided* ν_2 or *gap guided* ν_1. An index guided mode has its energy concentrated inside the defect and interacts only with the first row of holes adjacent to the defect. Its behavior can be simply represented by a dielectric waveguide with periodical corrugation. A gap guided mode interacts with several rows of holes, thus it is dependent on the symmetry of the PC and its PBG. The names index guided and gap guided don't specify exactly the guidance mechanisms (in the PBG region all modes are gap guided) but mainly describe the resemblance in terms of the modal field distribution. Any mode of the periodical waveguide generally shows a small group velocity near the band edge which eventually vanishes at the Brillouin zone edge.

If the waveguide is realized on a membrane, it is possible to see the same odd and even modes observed in the PBG region, though the PBG region is moved at higher frequencies. The main difference is the appearance of the radiation modes above the

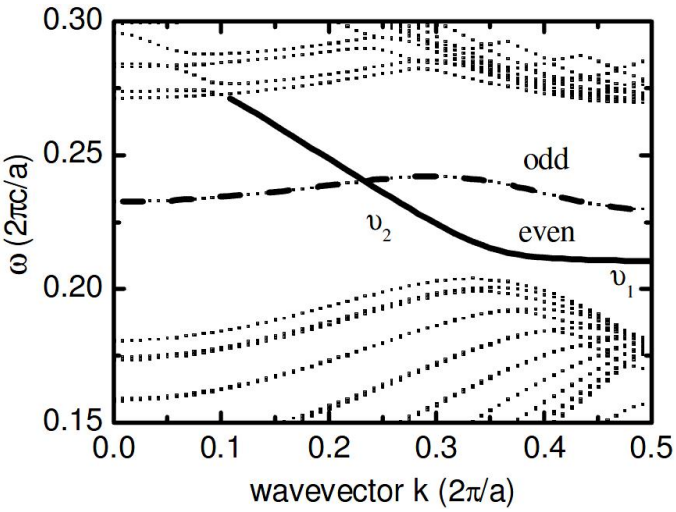

Figure 3.4: Dispersion relation for the photonic crystal waveguide of Fig. 3.3 with $w = a\sqrt{3}$, $r = 0.30a$ and $\varepsilon_{diel} = 12.25$, TE polarization. The thick lines represent the modes introduced by the line defect.

light line. These modes do not fulfill completely the total internal reflection condition and are scattered vertically. Thus only the modes below the light line are available in the slab structure for application.

3.3.2 Group velocity and slow light

The group velocity v_g of light with frequency ω in a waveguide is given as

$$v_g = \frac{d\omega}{dk} = \frac{c}{n_g}, \tag{3.11}$$

where k is the wave vector along the waveguide and n_g the group index.

The group velocity in a PhC waveguide is strongly dependent on the frequency as quantified by the group velocity dispersion (GVD) parameter β_2:

$$\beta_2 = \frac{d^2k}{d\omega^2} = \frac{1}{c}\frac{dn_g}{d\omega}. \tag{3.12}$$

The group velocity is a function of structural parameters, that can change completely the dispersion relation of a photonic crystal waveguide, as it is possible to see in the Fig. 3.5. The phenomenon of the low group velocity is called *slow light*. The flatter is the dispersion relation of a mode, the smaller is the group velocity, the slower is the light propagating into the waveguide.

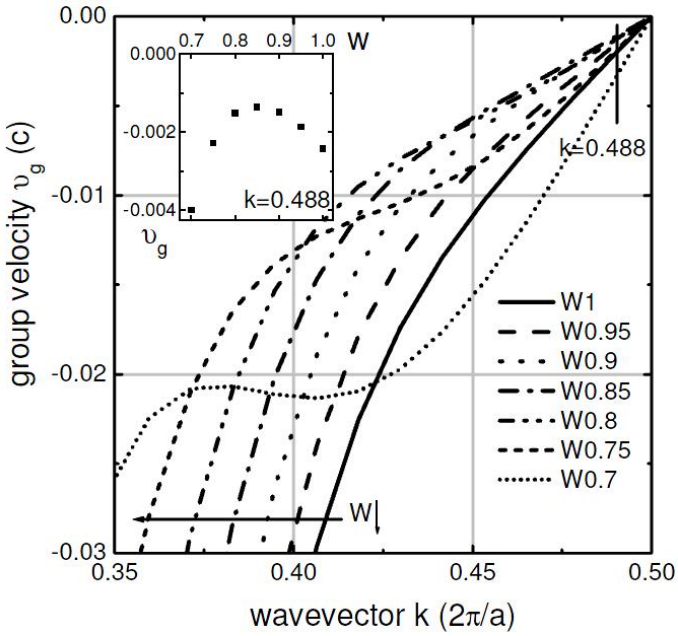

Figure 3.5: Group velocity as a function of wavevector for $r = 0.275a$ for different waveguide widths. The inset show group velocity at the k-point $k = 0.4888$, where the absolute value of v_g has a minimum at W0.85. A bandwidth of constant group velocity is obtained at W0.7 [28].

The exploitation of slow light phenomena opens perspectives for the realization of very compact and massively integrated optical functions (delay lines, GVD compensation, etc.) [29][30][31]. Very small values of group velocity have been reported by several groups ($v_g \simeq c/200$ [32]), however the waveguide length was very short in that case, resulting into a moderate group delay. Longer structures, potentially providing longer delays, are problematic, because the impact of propagation loss increases dramatically.

It was also demonstrated [33] the possibility to tailor the dispersion properties of the fundamental even mode. In this way , it is possible to obtain semi-slow light having a group velocity in the range $v_g \in [c/15 - c/100]$.

The photonic crystal waveguide with these properties is show in Fig. 3.6. It is realized as silicon-on-insulator structure with an height of 338nm. The peculiarity is that the holes of the first two rows have a radius r_1 and r_2, respectively, while all the other holes have with radius $r = 117$nm. Fig. 3.7 shows ~ 11nm bandwidth below the silica-line with a nearly constant group velocity $\sim c/34$ and relatively low and positive group velocity dispersion with β_2 on the order of $10^5 - 10^6 \text{ps}^2/\text{km}$. Within

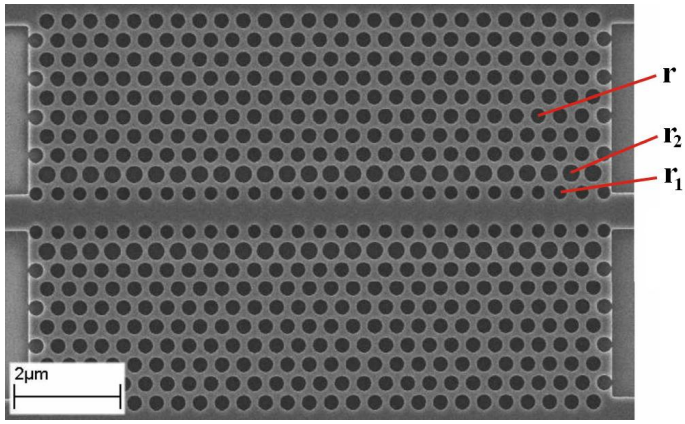

Figure 3.6: Scanning electron micrograph of the perturbed photonic crystal waveguide used in [33]. The radii r_1, r_2 have been decreased/increased compared to the radius r of the bulk holes.

this bandwidth, the measured propagation loss is less than 20dB/mm and drops below 5dB/mm for $\sim$ 2nm bandwidth.

3.4 Slow Light

In this section, we want to understand better the phenomenon of slow light, that offers functionality to control the speed of light by structuring alone.

We can define the *slowdown factor* as the ratio of the phase velocity over the group velocity:

$$S = \frac{v_\phi}{v_g}. \tag{3.13}$$

If it is taken in account bandwidth and dispersion [34], the performance of slow light devices scales as the refractive index contrast, so that an high refractive index structure such as photonic crystals appears promising.

The nature of the delay in a photonic crystal waveguide is easily understood by using the ray picture commonly used to describe light propagation in a dielectric waveguide. Compared with total internal reflection alone, however, photonic crystals offer two additional features that can lead to the formation of slow modes.

Backscattering Light is coherently backscattered at each unit cell of the crystal, so the crystal acts as a one-dimensional grating (indicated by the vertical lines on the left-hand side of Fig. 3.8. If the forward propagating and the backscattered

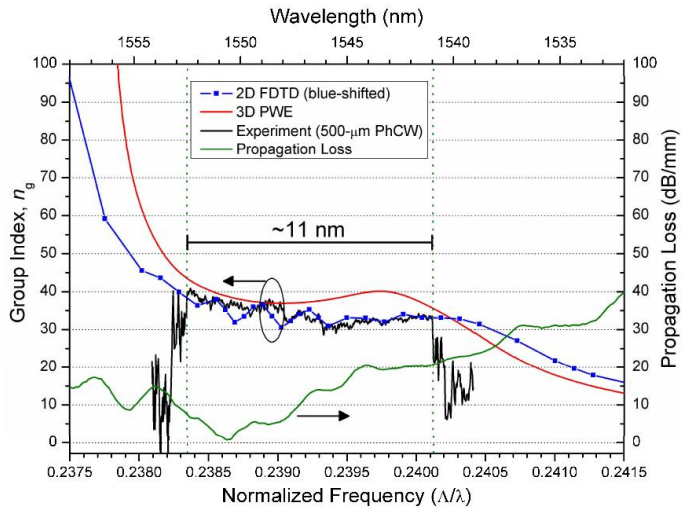

Figure 3.7: Measured (black), 2D FDTD (blue) and 3D PWE (red) calculated group index for the perturbed PhCWG of [33]. In green the measured propagation loss is plotted.

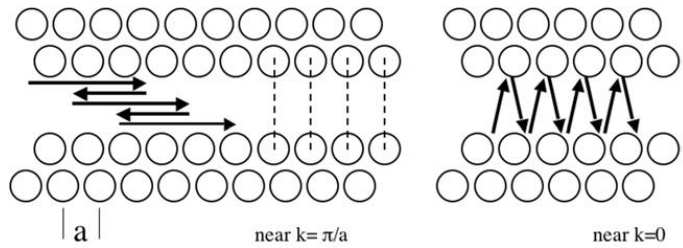

Figure 3.8: Illustration of the two possible mechanisms for achieving slow light in photonic crystal waveguides, namely coherent backscattering (left) and omni directional reflection (right).

light agree in phase and amplitude (as they do at the Brillouin zone boundary for $k = \pi/a$), a standing wave results, which can also be understood as a slow mode with zero group velocity. If we move away from the Brillouin zone boundary, we enter the slow light regime; the forward and backward traveling components begin to move out of phase but still interact, resulting in a slowly moving interference pattern: the slow mode. Further from the Brillouin zone boundary, the forward and backward traveling waves are too much out of phase to experience much interaction and the mode behaves like a regular waveguide mode that is dominated by total internal reflection. In Fig. 3.8, the slow light regime is depicted by arrows pointing right and left, for the forward and

backward traveling components, respectively. The forward arrows are longer, because a slow forward movement is as three steps forward and two steps back. This explanation suggests that the slow light effect is limited to the Brillouin zone boundary. This is not true, however; the key point is that the optical mode is close to a resonance with the structure. Other resonances may be created, such as anticrossing points, where slow light effects also occur [28]. Therefore, by balancing multiple resonances carefully, one may induce a slow light regime that spans a considerable fraction of the Brillouin zone.

Omni directional reflection The other unique feature offered by the photonic crystal environment is that there is no cut-off angle; if a photonic bandgap is present, light propagating at any angle is reflected. Even light propagating at or near normal incidence may therefore form a mode, as indicated by the steep zigzag on the right of Fig. 3.8. In band structure terms, this corresponds to propagation at or near the Γ point, i.e. $k \approx 0$. It is obvious that such modes have very small forward components, i.e. they travel as slow modes along the waveguide, or for $k = 0$, form a standing wave.

These two effects also represent the two limiting cases for slow light propagation in photonic crystal waveguides; the bandwidth is ultimately limited by the size of the Brillouin zone. In order to achieve a group velocity of c/n_g, with n_g the group index, the maximum bandwidth can then be determined as follows:

$$v_g = \frac{d\omega}{dk} = \frac{c}{n_g} \quad \Rightarrow \quad \Delta\nu = \frac{1}{2\pi}\frac{c}{n_g}\frac{1}{2}\frac{2\pi}{a} = \frac{c}{2n_g a} \tag{3.14}$$

As an example, for $n_g = 100$ and a typical period of $a = 400$nm at 1.55µm wavelength, the bandwidth will be $\Delta\nu = 3.75$THz. In practice, and subject to good design and operation below the light line, it may be possible to achieve 20-30% of this bandwidth, which corresponds approximately to 1THz. A value of $n_g = 100$ corresponds to a slowdown factor of $S \approx 50$, given the typical phase index in a semiconductor photonic crystal material of around 2. Recent papers have already shown structures approaching this performance [28]. Please note that the above discussion holds for symmetric structures, which indeed represent the majority of structures studied in the literature; asymmetry may offer additional design parameters, as shown in [35] and [36].

3.4.1 Slowdown factor and linear interactions

Any type of optical device, linear or nonlinear, operates on the basis of a relative phase change, typically expressed as ΔkL. It is possible to rewrite this phase change as $\Delta n k_0 L$, with Δn the refractive index change and k_0 the wavevector in free space. This refractive index change depends on two index: the material index n_{mat} and the effective modal index n_{eff}.

Suppose to consider a given mode into a PhCWG. If the material index is changed for some reasons, the mode moves accordingly, and the corresponding change in frequency is proportional to the change in index, so $\Delta\omega/\omega \approx \Delta n_{\text{mat}}/n_{\text{mat}}$. But if the change is in the effective modal index, we have that $\Delta n_{\text{eff}} = (c/\omega)\Delta k$. It is clear that where the dispersion curve is flat, i.e. in the slow light regime, the Δk and therefore the Δn_{eff} is much larger than in the fast light regime where the dispersion curve is steeper. So a slow mode experiences a larger change in effective index than a fast mode, despite the fact that the change in material index Δn_{mat} is the same in both the cases.

Since Δk scales with the slope of the dispersion curve, it also scales with the slowdown factor, which allows us to write the condition for switching as

$$\Delta kL = k_0 S \Delta n_{\text{mat}} L, \tag{3.15}$$

which now includes the slowdown factor. This highlights the fact that although the slowdown factor is defined in terms of group velocity, the slow light regime offers significant benefits for devices operating on the basis of phase velocity or effective index. A beautiful demonstration of this effect was recently provided by Vlasov in [29], by demonstrating experimentally that a thermo-optically tuned Mach-Zehnder modulator requires less energy when operating in the slow light regime than it does when operating in the fast light regime.

3.4.2 Slowdown factor and intensity

If we assume a dispersion-free environment, i.e. one where the different spectral components of a pulse experience the same slowdown factor, a pulse will be spatially compressed when entering the slow light regime. The front of the pulse, entering the slow light regime first, will travel slower than the back of the pulse which therefore catches up. The resulting pulse will occupy less space, i.e. it will be *spatially compressed* without changing its properties in terms of time and spectrum. If we further

assume that no energy is lost at the interface, the same amount of energy is concentrated in a smaller volume, so the intensity of the pulse increases. This effect can be shown mathematically, using a Gaussian pulse as an example. The distribution of a Gaussian pulse can be described by the following functional dependence:

$$I(x) = I_0 \exp(-Sx)^2, \tag{3.16}$$

where I_0 is the peak intensity and S the slowdown factor, with x a spatial coordinate normalized to the size of the pulse. The full width half maximum (FWHM) of such a pulse scales inversely with S, which is the condition discussed above; a larger slowdown factor results in a shorter pulse. Given that the total pulse energy does not change, the integral over the pulse has to be a constant, which is achieved by the following expression:

$$\int_{-\infty}^{\infty} I_0 \exp(-Sx)^2 dx = I_0 \frac{\sqrt{\pi}}{S} \quad \Leftrightarrow \quad \int_{-\infty}^{\infty} I_0 \frac{S}{\sqrt{\pi}} \exp(-Sx)^2 dx = I_0. \tag{3.17}$$

This shows that the peak intensity scales linearly with the slowdown factor and inversely with the size of the pulse; as the pulse is spatially compressed, the peak intensity increases by the same factor in order to satisfy energy conservation.

Overall, nonlinear interaction benefits twofold from the slowdown factor, namely (a) via the enhanced phase change and (b) via the enhanced intensity, such that the interaction in a Kerr-medium, for example, can be written as

$$n_{\text{mode}} = n_0 + n_2 I = n_0 + S(n_2 I S). \tag{3.18}$$

In general, the $\chi^{(3)}$ nonlinearities scale with the square of the slowdown factor. This favorable scaling law is unique to slow light devices based on dielectric structures such as photonic crystals and ring resonators; while slow light based on material resonances does not exhibit the same effect. Naturally, there are limitations. The square scaling law assumes zero dispersion and no change of mode distribution.

If the dispersion is nonzero, pulses will broaden, with drastic consequences such that the effect of dispersion may outweigh any benefit of slow light compression [37]. It is therefore important to design waveguides with low second and higher order dispersion. This has already been proposed by several authors [28] who adjusted the dispersion curve of a W1-type waveguide, in particular the presence of an anticrossing with the lattice modes, by adjusting its width and/or the diameter of the innermost rows of holes. The second limitation arises from the assumption of unchanged mode

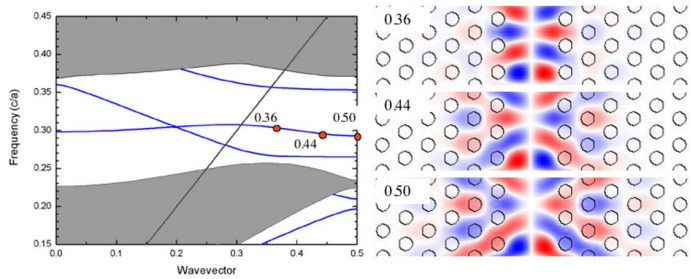

Figure 3.9: Comparison of the shape of a guided mode in the fast and the slow light regime, exemplified by the odd mode of the system. The odd mode was chosen as it demonstrates the effect more dramatically than the fundamental mode. The respective k values are indicated both in the mode profiles and in the corresponding band structure. As k approaches the Brillouin zone boundary, the mode slows down and samples deeper into the photonic lattice.

shape. In photonic crystals, this assumption does not generally hold, as illustrated in figure 3.9. In the slow light regime, the mode samples more of the photonic lattice and therefore assumes a different shape. So even though the mode may compress in propagation direction, the corresponding lateral spread dilutes some of the benefit one can expect. This leads to the conclusion that an enhancement proportional to S^P with $1 < P < 2$ can be expected in reality, depending on how well the above conditions on dispersion and mode shape are met. Nevertheless, even for a modest slowdown factor of around 20, an overall enhancement of around 100 can be expected for $P = 1.5$. So the size of a Kerr-type optical switch would drop from centimeters to hundreds of micrometers, or the required switching power would be reduced by two orders of magnitude. This is also equivalent to increasing the nonlinear coefficient (the n_2 or the $\chi^{(3)}$) by two orders of magnitude, simply by appropriately microstructuring the material.

3.5 Third Order Dispersion

It is possible to consider a PhCWG as a system with a well defined transfer function:

$$H(\omega) = \exp(-(\alpha(\omega) + \imath\beta(\omega))L) \tag{3.19}$$

where $\alpha(\omega)$ is the attenuation constant, $\beta(\omega)$ is the mode propagation constant, and L is the length of the PhCWG. By neglecting attenuation, it is possible to rewrite

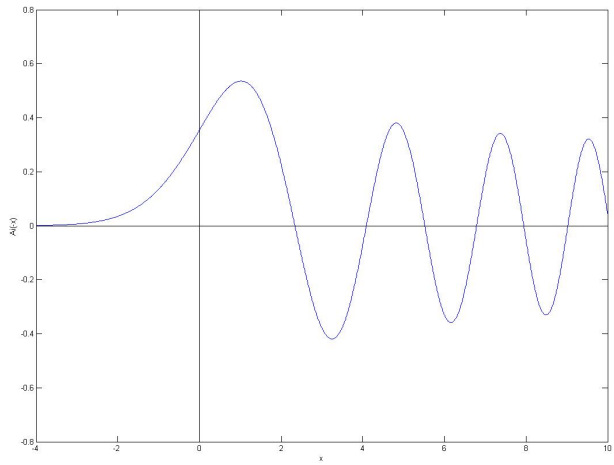

Figure 3.10: Airy function

it as

$$H(\omega) = \mathrm{e}^{-\imath\beta(\omega)L}. \tag{3.20}$$

As we already saw in Sec. 1.3, the propagation of light into a PhCWG is described with Floquet-Bloch waves, and the dispersion relation is characterized by allowed and prohibited bands (see Fig. 3.4).

The interval of frequencies that a pulse will excite depends on the width τ_p of the pulse. If the pulse bandwidth is narrow enough, we can consider just the portion of the dispersion relation relative to the waveguide modes, located in the PBG region. They are denoted *even* and *odd* by their in-plane symmetry with respect to the waveguide. Focusing only on the even mode, we can write the relative Bloch mode as

$$\tilde{E}(z,\omega) = \tilde{E}_0(\omega)\exp(-ik_0(\omega)z) \tag{3.21}$$

where $\tilde{E}_0(\omega)$ and $k_0(\omega)$ are the amplitude of the electric field and the wavevector of the Bloch wave, respectively. In this equation, we focus our attention only on the z direction.

We can approximate $k_0(\omega)$ with a Taylor expansion around the central frequency of the pulse ω_0

$$k_0(\omega) = \sum_{i=0}^{\infty} \frac{\beta_i}{i!}(\omega-\omega_0)^i \tag{3.22}$$

where the coefficients $\beta_i = \left.\dfrac{d^i k}{d\omega^i}\right|_{\omega=\omega_0}$.

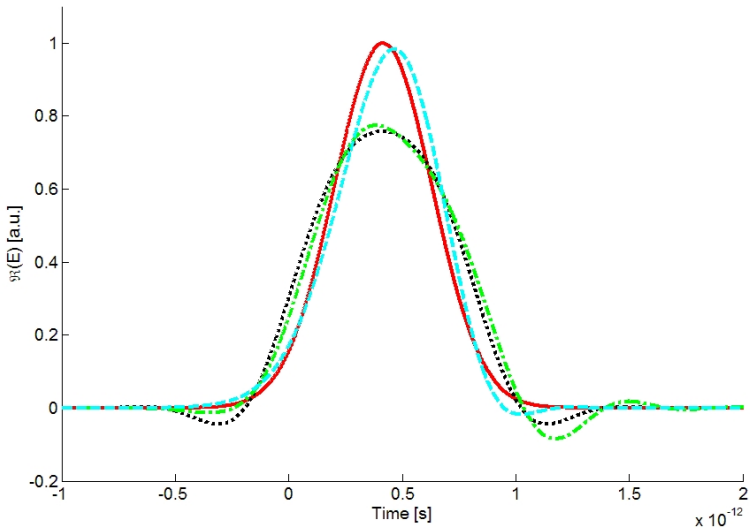

Figure 3.11: Real part of pulses modified by different order of dispersion. In red (continuous line) the initial pulse E_0; in black (dotted line) the pulse modified by a second order dispersion $\beta_2 = 1 \cdot 10^{-20}\mathrm{s}^2/\mathrm{m}$; in cyan (broken line) the pulse modified also by a TOD $\beta_3 = 1 \cdot 10^{-33}\mathrm{s}^3/\mathrm{m}$, and in cyan (broken dotted line) the pulse modified by the TOD, but supposing $\beta_2 = 0$.

The evolution of the propagating electric field can be obtained from the inverse Fourier transform of Eq. 3.21

$$E(z,t) = \mathcal{F}^{-1}\left\{\tilde{E}(z,\omega)\right\}. \tag{3.23}$$

If we consider a Gaussian pulse[1] with intensity width τ_p centered at frequency ω_0 and at time $t = t_0$

$$E_0(t) = E_0 \exp\left(-\frac{(t-t_0)^2}{\tau_p^2} + \imath\omega_0 t\right), \tag{3.25}$$

and the Taylor expansion of the dispersion stopped at the third order, we obtain

$$E(z,t) = \frac{E_0}{\sqrt{\pi}} e^{\imath(\omega_0 t - \beta_0 z)} \int_{-\infty}^{\infty} \exp\left(iB_1\omega - (1+iB_2)\omega^2 - \imath\frac{B_3}{3}\omega^3\right) d\omega, \tag{3.26}$$

where B_1, B_2, and B_3 are defined by

$$B_1 = 2(t - \beta_1 z)/\tau_p \tag{3.27}$$

[1] In the frequency domain, the pulse becomes

$$\tilde{E}_0(\omega) = \frac{E_0\tau_p}{\sqrt{2}} \exp\left(-\frac{\tau_p^2}{4}(\omega-\omega_0)^2 + \imath\omega t_0\right). \tag{3.24}$$

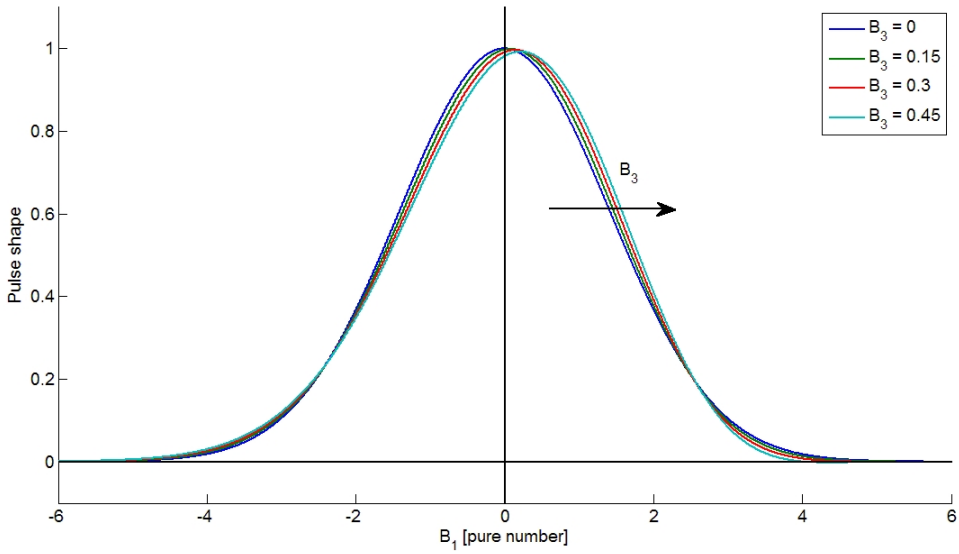

Figure 3.12: Real part of pulses modified by low values of TOD factor with $\beta_2 = 0$.

$$B_2 = 2\beta_2 z/\tau_p^2 \tag{3.28}$$

$$B_3 = 4\beta_3 z/\tau_p^3. \tag{3.29}$$

If $B_3 = 0$, it is possible to rewrite the pulse in a simpler way:

$$\begin{aligned} E(z,t) &= \frac{E_0}{\sqrt{1+iB_2}} e^{\imath(\omega_0 t - \beta_0 z)} \exp\left[-\frac{B_1^2}{4(1+iB_2)}\right] \\ &= \frac{\tau_p E_0}{\sqrt{\tau_p^2 - 2iz\beta_2}} e^{\imath(\omega_0 t - \beta_0 z)} \exp\left[-\frac{(t-\beta_1 z)^2}{\tau_p^2 - 2iz\beta_2}\right] \end{aligned} \tag{3.30}$$

If $B_3 \neq 0$, by changing the variable $\omega = B_3^{-1/3} u + (\imath - B_2)/B_3$, and using some properties of complex integration we can express $E(z,t)$ as:

$$\begin{aligned} E(z,t) = &\frac{2E_0\sqrt{\pi}}{|B_3|^{1/3}} e^{\imath(\omega_0 t - \beta_0 z)} \\ &\times \exp\left(\frac{2 - 3B_1B_3 - 6B_2^2}{3B_3^2} + iB_2\frac{6 - 3B_1B_3 - 2B_2^2}{3B_3^2}\right) \\ &\times \mathrm{Ai}[(1 - B_1B_3 - B_2^2 + 2iB_2)B_3^{-4/3}], \end{aligned} \tag{3.31}$$

where $\mathrm{Ai}(\cdot)$ is the Airy function (see Fig. 3.10). When the total second order

dispersion vanishes, i.e. $B_2 = 0$, we have

$$E(z,t) = \frac{2E_0\sqrt{\pi}}{|B_3|^{1/3}} e^{\imath(\omega_0 t - \beta_0 z)} \times \exp\left(\frac{2 - 3B_1B_3}{3B_3^2}\right) \times \mathrm{Ai}[(1 - B_1B_3)B_3^{-4/3}]. \tag{3.32}$$

In Fig. 3.11 and 3.12, pulses with different values of B_2 and B_3 are shown.

Eq. 3.31 shows that the pulse shape for $\beta'''(\omega_0) < 0$ is the same for $\beta'''(\omega_0) > 0$ with time reversed at the time $t = \beta'(\omega_0)z$. From now on, we'll consider just the case with $\beta'''(\omega_0) > 0$.

3.5.1 Effects of Third-Order Dispersion

Figures 3.12 shows the pulse shape for limited values of B_3, when SOD vanishes, calculated using the Eq. 3.32. We can see that the pulse is approximately Gaussian with a shift of the peak in the positive B_1-direction when B_3 is positive and vice versa. This means that the group velocity of the pulse change due to the TOD term. The group velocity of the pulse is obtained by the condition $\partial|E(z,t)|\partial t = 0$, that can be written as:

$$-\frac{1}{B_3}\mathrm{Ai}\left[(1 - B_1B_3 - B_2^2 + 2iB_2)B_3^{-4/3}\right] + \frac{\partial}{\partial B_1}\mathrm{Ai}\left[(1 - B_1B_3 - B_2^2 + 2iB_2)B_3^{-4/3}\right] = 0. \tag{3.33}$$

Substituting $x = (1 - B_1B_3 - B_2^2 + 2iB_2)B_3^{-4/3}$, we get:

$$\mathrm{Ai}(x) + B_3^{2/3}\frac{\partial}{\partial x}\mathrm{Ai}(x) = 0, \tag{3.34}$$

and resolving it numerically, it holds

$$v_g^{-1} = v_{g0}^{-1} + f(B_2, B_3), \tag{3.35}$$

where $v_{g0} = 1/\beta_1 = 1/\beta'(\omega_0)$ is the group velocity of the pulse when TOD does not exist and $f(B_2, B_3)$ is a function of B_2 and B_3, that the describes the changes of group velocity. The Fig. 3.13 shows this change, and in the inset of the same figure, it is possible to observe that for $B_3 \leq 0.3$, the function $f(B_2, B_3)$ shows a linear trend. Using this hypothesis, Eq. 3.35 becomes:

$$v_g^{-1} = v_{g0}^{-1} + \frac{\tau_p}{4z}\frac{1 - B_2^2}{1 + B_2^2}B_3. \tag{3.36}$$

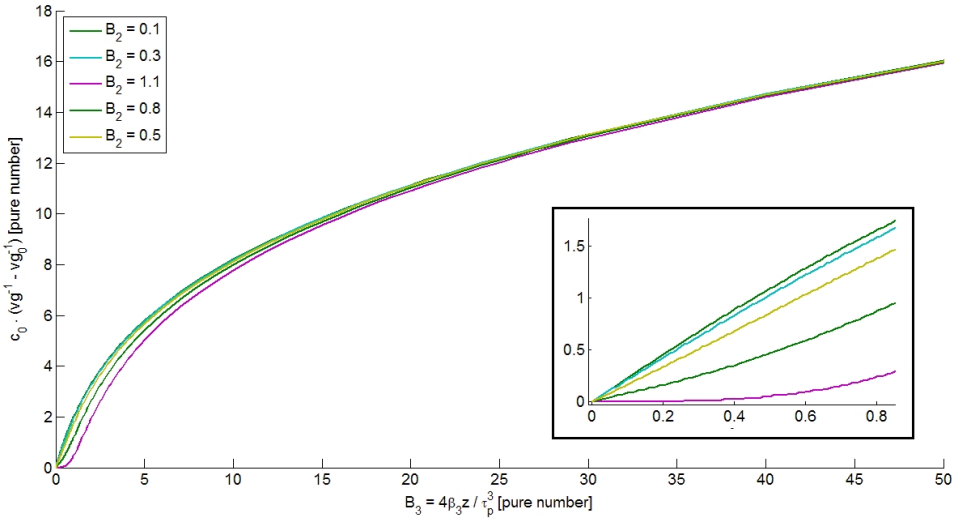

Figure 3.13: Change in group velocity in function of B_3. In the inset, it is shown the linear behavior of the group velocity for small values of B_3.

By considering the center of the pulse[2] and by supposing that it is not very sensitive to B_2, we can model the position of the center of the pulse with the following equation:

$$\mu = \mu_0 + \tau_p \; B_3/8, \tag{3.38}$$

where $\mu_0 = \beta_1 z$ is the center of the pulse in a non-dispersive medium ($\beta_2 = 0$).

In a similar manner, we consider the width of the pulse[3] and we find, as shown in Fig. 3.14, that for little values of B_3, the width is constant to the value set by B_2, while when B_3 grows up, the pulse width grows almost proportionally to B_3.

[2]We define the pulse center μ as follows:

$$\mu = \frac{\int_{-\infty}^{\infty} t \cdot I(t)dt}{\int_{-\infty}^{\infty} I(t)dt}, \tag{3.37}$$

where $I(t)$ is the intensity of the pulse $I(t) = |E(t)|^2$.

[3]We define the pulse center W as follows:

$$W = \left[8 \ln 2 \frac{\int_{-\infty}^{\infty} (t-\mu)^2 \cdot I(t)dt}{\int_{-\infty}^{\infty} I(t)dt} \right]^{1/2}, \tag{3.39}$$

where $I(t)$ is the intensity of the pulse $I(t) = |E(t)|^2$.

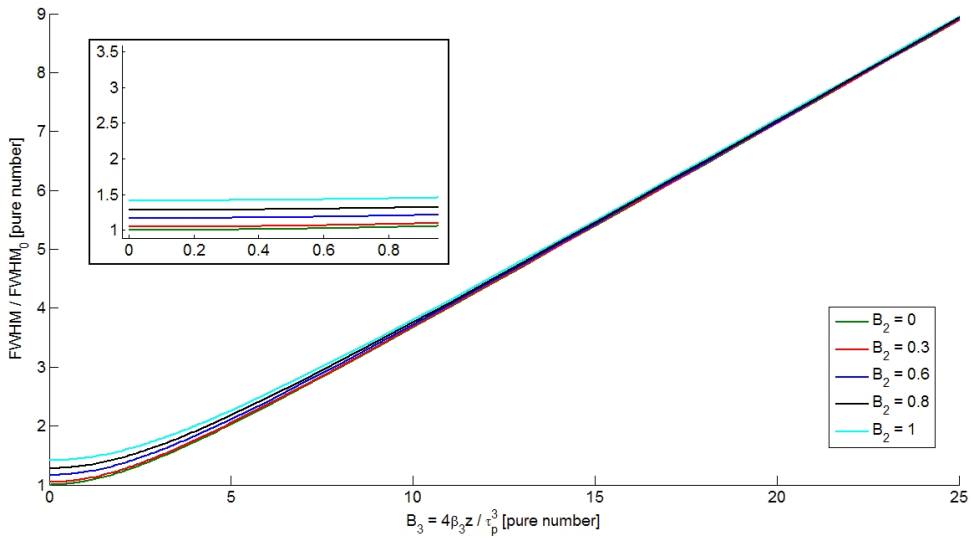

Figure 3.14: Width of the pulse calculated for different values of B_2.

3.6 Four-wave mixing equations in photonic crystal waveguide

All the waveguides considered till now are passive ones, because they are based just on the linear behavior of photonic crystal. To develop application involving a time variable control on the flow of light, it is necessary consider non-linear effects. In particular, we consider cubic non-linearity due to third order susceptibility so that we can derivate the Four-wave mixing equations for a photonic crystal waveguide.

Let us start from the Maxwell's equations in the time domain

$$\begin{aligned} \nabla \times \mathbf{E}(\mathbf{r},t) &= -\mu \frac{\partial}{\partial t}\mathbf{H}(\mathbf{r},t) \\ \nabla \times \mathbf{H}(\mathbf{r},t) &= \varepsilon(\mathbf{r}) \frac{\partial}{\partial t}\mathbf{E}(\mathbf{r},t), \end{aligned} \tag{3.40}$$

where the permittivity is a spatially varying function, as usual in a photonic crystal waveguide.

Let us suppose that four frequencies, satisfying the condition $\omega_1 + \omega_2 = \omega_3 + \omega_4$ are propagating in the same fundamental mode of the photonic crystal, i.e.:

$$\begin{aligned} \mathbf{E}(\mathbf{r},t) &= \sum_{k=1}^{4} \mathbf{E}_k(\mathbf{r},t) = \sum_{k=1}^{4} A_k \mathbf{e}(\mathbf{r},\omega_k) e^{\imath(\beta_k z - \omega_k t)} + \text{c.c.} \\ \mathbf{H}(\mathbf{r},t) &= \sum_{k=1}^{4} \mathbf{H}_k(\mathbf{r},t) = \sum_{k=1}^{4} A_k \mathbf{h}(\mathbf{r},\omega_k) e^{\imath(\beta_k z - \omega_k t)} + \text{c.c.}, \end{aligned} \tag{3.41}$$

where $\beta_k = \beta(\omega_k)$ are the mode propagation constants, A_k and $\mathbf{e}(\mathbf{r}, \omega_k)$, $\mathbf{h}(\mathbf{r}, \omega_k)$ are the complex amplitudes and the electric and magnetic Bloch modes at $\omega_k = 1, 2, 3, 4$, respectively.

For each frequency, Maxwell's equations yield

$$\begin{aligned} \nabla \times \left[\mathbf{e}(\mathbf{r}, \omega_k) e^{\imath \beta_k z}\right] &= \imath \mu \omega_k \mathbf{h}(\mathbf{r}, \omega_k) e^{\imath \beta_k z} \\ \nabla \times \left[\mathbf{h}(\mathbf{r}, \omega_k) e^{\imath \beta_k z}\right] &= -\imath \varepsilon(\mathbf{r}) \omega_k \mathbf{e}(\mathbf{r}, \omega_k) e^{\imath \beta_k z}, \end{aligned} \tag{3.42}$$

that are exactly the equations that define the Bloch modes of the waveguide.

Let us now consider a nonlinear perturbation of the Maxwell's equations:

$$\begin{aligned} \nabla \times \mathbf{E}(\mathbf{r}, t) &= -\mu \frac{\partial}{\partial t} \mathbf{H}(\mathbf{r}, t) \\ \nabla \times \mathbf{H}(\mathbf{r}, t) &= \varepsilon(\mathbf{r}) \frac{\partial}{\partial t} \mathbf{E}(\mathbf{r}, t) + \frac{\partial}{\partial t} \mathbf{P}_{NL}(\mathbf{r}, t), \end{aligned} \tag{3.43}$$

The nonlinear polarization due to the third order susceptibility can be described by a third order tensor which shows a tensor character also in an isotropic material (e.g. semiconductors). In this case, it reads as:

$$\mathbf{P}^{NL} = A\,(\mathbf{E} \cdot \mathbf{E}^*)\mathbf{E} + \frac{1}{2}\,B\,(\mathbf{E} \cdot \mathbf{E})\mathbf{E}^* \tag{3.44}$$

with the definition: $\mathbf{E}(t) = \frac{1}{2}\mathbf{E}(\omega)\exp(i\,\omega\,t) + \text{c.c.}$

The coefficients A and B depend on the dominant nonlinear process. If the non-resonant electronic contribution is dominant, then: $B = A = \frac{1}{2}\chi^{(3)}$ [38].

When the nonlinearity is small, the (linear) mode structure (eqs. 3.42) is not altered and the only modification is that the complex amplitudes become slowly varying in the z direction: $A_k = A_k(z)$. Note that A_k is slowly varying with respect to both $e^{\imath \beta_k z}$ and the Bloch mode within the cell: $\mathbf{e}(\mathbf{r}, \omega_k), \mathbf{h}(\mathbf{r}, \omega_k)$.

Among all terms generated by the cubic nonlinearity we retain here only those accounting for self- and cross-phase modulation (SPM, XPM), that are always self-phase matched effects, and those accounting for non degenerate four wave mixing (FWM). The latter are considered in the hypothesis, to be later verified, that they are phase-matched. Phase-matching the non-degenerate FWM typically prevents other nonlinear effects (e.g. third harmonic generation, other sum and difference frequency generation) to occur.

Then, the nonlinear polarization consists of four terms only, each one oscillating

at one of the selected frequencies $\omega_k,\ k = 1, 2, 3, 4$:

$$\begin{aligned}
\mathbf{P}_1^{NL} &= \frac{3}{4}\varepsilon_0\chi^{(3)}(\mathbf{r})\left[(|\mathbf{E}_1|^2 + 2\sum_{l=2,3,4}|\mathbf{E}_i|^2)\mathbf{E}_1 + 2\mathbf{E}_3\mathbf{E}_4\mathbf{E}_2^*\right]\\
\mathbf{P}_2^{NL} &= \frac{3}{4}\varepsilon_0\chi^{(3)}(\mathbf{r})\left[(|\mathbf{E}_2|^2 + 2\sum_{l=1,3,4}|\mathbf{E}_i|^2)\mathbf{E}_2 + 2\mathbf{E}_3\mathbf{E}_4\mathbf{E}_1^*\right]\\
\mathbf{P}_3^{NL} &= \frac{3}{4}\varepsilon_0\chi^{(3)}(\mathbf{r})\left[(|\mathbf{E}_3|^2 + 2\sum_{l=1,2,4}|\mathbf{E}_i|^2)\mathbf{E}_3 + 2\mathbf{E}_1\mathbf{E}_2\mathbf{E}_4^*\right]\\
\mathbf{P}_4^{NL} &= \frac{3}{4}\varepsilon_0\chi^{(3)}(\mathbf{r})\left[(|\mathbf{E}_4|^2 + 2\sum_{l=1,2,3}|\mathbf{E}_i|^2)\mathbf{E}_4 + 2\mathbf{E}_1\mathbf{E}_2\mathbf{E}_3^*\right]
\end{aligned} \tag{3.45}$$

For simplicity let us consider eqs. (3.43) at one frequency only (ω_4); the equations for the other three frequencies can be obtained following the same guideline. Let substitute the last of eqs. (3.45) into eqs. (3.43) also using eqs. (3.41):

$$\begin{aligned}
\nabla \times \left[A_4\mathbf{e}_4 e^{\imath\beta_4 z}\right] &= \imath\mu\omega_4 A_4\mathbf{h}_i e^{\imath\beta_4 z}\\
\nabla \times \left[A_4\mathbf{h}_4 e^{\imath\beta_4 z}\right] &= -\imath\varepsilon(\mathbf{r})\omega_4 A_4\mathbf{e}_4 e^{\imath\beta_4 z} - \imath\omega_4\frac{3}{4}\varepsilon_0\chi^{(3)}(\mathbf{r})\\
&\quad\left[\left(|A_4|^2|\mathbf{e}_4|^2 + 2\sum_{l=1}^{3}|A_l|^2|\mathbf{e}_l|^2\right)A_4\mathbf{e}_4 e^{\imath\beta_4 z}\right.\\
&\quad\left. + 2A_1A_2A_3^*\mathbf{e}_1\mathbf{e}_2\mathbf{e}_3^* e^{\imath(\beta_1+\beta_2-\beta_3)z}\right],
\end{aligned} \tag{3.46}$$

where the following notation is also used for the sake of simplicity: $\mathbf{e}(\mathbf{r}, \omega_k) = \mathbf{e}_k, \mathbf{h}(\mathbf{r}, \omega_k) = \mathbf{h}_k$, for $k = 1, 2, 3, 4$.

Calculating the curls explicitly and subtracting eqs. 3.42 from eqs. 3.46 yields:

$$\begin{aligned}
\nabla A_4 \times \left[\mathbf{e}_4 e^{\imath\beta_4 z}\right] &= 0\\
\nabla A_4 \times \left[\mathbf{h}_4 e^{\imath\beta_4 z}\right] &= -\imath\omega_4\frac{3}{4}\varepsilon_0\chi^{(3)}(\mathbf{r})\\
&\quad\left[\left(|A_4|^2|\mathbf{e}_4|^2 + 2\sum_{l=1}^{3}|A_l|^2|\mathbf{e}_l|^2\right)A_4\mathbf{e}_4 e^{\imath\beta_4 z}\right.\\
&\quad\left. + 2A_1A_2A_3^*\mathbf{e}_1\mathbf{e}_2\mathbf{e}_3^* e^{\imath(\beta_1+\beta_2-\beta_3)z}\right].
\end{aligned} \tag{3.47}$$

Note that the latter equations are approximated, in the sense that the mode structure was supposed to be not affected by the non linearity.

From eqs. (3.47) the following can be derived:

$$\begin{aligned}
&\nabla A_4 \times \left[\mathbf{e}_4 e^{\imath\beta_4 z}\right] \cdot \mathbf{h}_4^* e^{-\imath\beta_4 z} = 0 \\
&\nabla A_4 \times \left[\mathbf{h}_4 e^{\imath\beta_4 z}\right] \cdot \mathbf{e}_4^* e^{-\imath\beta_4 z} = -\imath\omega_4 \frac{3}{4}\varepsilon_0 \chi^{(3)}(\mathbf{r}) \\
&\qquad \left[\left(|A_4|^2|\mathbf{e}_4|^2 + 2\sum_{l=1}^{3}|A_l|^2|\mathbf{e}_l|^2\right) A_4|\mathbf{e}_4|^2 \right. \\
&\qquad \left. + 2A_1A_2A_3^*\mathbf{e}_1\mathbf{e}_2\mathbf{e}_3^*\mathbf{e}_4^* e^{\imath(\beta_1+\beta_2-\beta_3-\beta_4)z}\right].
\end{aligned} \tag{3.48}$$

By exploiting the cyclic permutation property of vector and scalar products and by setting $\nabla A_4 = \partial A_4/\partial z\ \hat{z}$, one gets

$$\begin{aligned}
&\frac{\partial A_4}{\partial z}\hat{z}\cdot(\mathbf{e}_4 \times \mathbf{h}_4^*) = 0 \\
&\frac{\partial A_4}{\partial z}\hat{z}\cdot(\mathbf{h}_4 \times \mathbf{e}_4^*) = -\imath\omega_4 \frac{3}{4}\varepsilon_0 \chi^{(3)}(\mathbf{r}) \\
&\qquad \left[\left(|A_4|^2|\mathbf{e}_4|^2 + 2\sum_{l=1}^{3}|A_l|^2|\mathbf{e}_l|^2\right) A_4|\mathbf{e}_4|^2 \right. \\
&\qquad \left. + 2A_1A_2A_3^*\mathbf{e}_1\mathbf{e}_2\mathbf{e}_3^*\mathbf{e}_4^* e^{-\imath\Delta\beta z}\right],
\end{aligned} \tag{3.49}$$

where $\Delta\beta = \beta_3 + \beta_4 - \beta_1 - \beta_2$ is the linear phase mismatch.

If the second of eqs. (3.49) is subtracted from the first and upon integration over the volume V of the elementary cell of the photonic crystal waveguide, the following relation is found

$$\begin{aligned}
&\frac{\partial A_4}{\partial z}\int_V (\mathbf{e}_4 \times \mathbf{h}_4^* + \mathbf{e}_4^* \times \mathbf{h}_4)\cdot\hat{z}\, dV \simeq \\
&\quad \simeq \imath\omega_4 \frac{3}{4}\varepsilon_0 \int_V \chi^{(3)}(\mathbf{r}) \left[\left(|A_4|^2|\mathbf{e}_4|^2 + 2\sum_{l=1}^{3}|A_l|^2|\mathbf{e}_l|^2\right) A_4|\mathbf{e}_4|^2 \right. \\
&\quad \left. + 2A_1A_2A_3^*\mathbf{e}_1\mathbf{e}_2\mathbf{e}_3^*\mathbf{e}_4^* e^{-\imath\Delta\beta z}\right] dV
\end{aligned} \tag{3.50}$$

where $\partial A_4/\partial z$ is considered a constant in the cell volume.

Yeh demonstrated in [39] that in photonic crystal waveguides the group and mean energy velocity are equal:

$$\mathbf{v}_{gk} = \nabla_\beta \omega(\beta) = \mathbf{v}_{ek} = \frac{\frac{1}{4V}\int_V (\mathbf{e}_k \times \mathbf{h}_k^* + \mathbf{e}_k^* \times \mathbf{h}_k)\, dV}{\frac{1}{4V}\int_V (\varepsilon_0\varepsilon_r(\mathbf{r})|\mathbf{e}_k|^2 + \mu_0|\mathbf{h}_k|^2)\, dV}. \tag{3.51}$$

By projecting this relation along the z direction, we get (for $k = 1, 2, 3, 4$)

$$\mathbf{v}_{gk}\cdot\hat{z} = \nabla_\beta \omega(\beta)\cdot\hat{z} = \mathbf{v}_{ek}\cdot\hat{z} = \frac{\int_V (\mathbf{e}_k \times \mathbf{h}_k^* + \mathbf{e}_k^* \times \mathbf{h}_k)\cdot\hat{z}\, dV}{\int_V (\varepsilon_0\varepsilon_r(\mathbf{r})|\mathbf{e}_k|^2 + \mu_0|\mathbf{h}_k|^2)\, dV}. \tag{3.52}$$

Moreover, it is known (e.g. [40]) that the time-space average electric and magnetic energies are equal for a Bloch mode:

$$\mathcal{E}_{magn} = \frac{1}{4}\mu_0 \int_V \mathbf{h}\cdot\mathbf{h}^* = \frac{1}{4}\int_V \mathbf{e}\cdot\mathbf{d}^* = \mathcal{E}_{elec}. \tag{3.53}$$

The integral $\int_V (\mathbf{e}_k \times \mathbf{h}_k^* + \mathbf{e}_k^* \times \mathbf{h}_k)\cdot\hat{z}\, dV$ that appears in eq. (3.50) is a normalization factor whose physical dimension is a length (m) as soon as the complex amplitudes A_k are such that $|A_k|^2 = P_k$ is the mean active power transported in the z direction within the cell.

Let us set:

$$\int_V (\mathbf{e}_k \times \mathbf{h}_k^* + \mathbf{e}_k^* \times \mathbf{h}_k)\cdot\hat{z}\, dV = 2a\, f_k, \tag{3.54}$$

It can be shown that the dimensionless factors f_k are all equal to 2. In fact, let us multiply eq. 3.54 on both sides by $|A_k|^2/(2V)$:

$$\frac{2}{V}\int_V Re[\mathbf{P_k}]\cdot\hat{z}\, dV = \frac{1}{S}\, f_k\, |A_k|^2 \tag{3.55}$$

where $\mathbf{P_k} = \mathbf{e}_k \times \mathbf{h}_k^*/2$ is the Poynting vector (power density) of the wave at frequency ω_k and $S = V/a$ is the cell cross-section. The LHS is twice the mean active power density flux in the z direction contained in the cell and so

$$2S\langle Re[\mathbf{P_k}]\cdot\hat{z}\rangle = 2P_k = f_k\, |A_k|^2 \tag{3.56}$$

which yields $f_k = 2$, also in agreement with [41].

From eqs. (3.52), (3.53) and (3.54) the group velocity can be written as:

$$\begin{aligned} v_{gk} &= \frac{\int_V (\mathbf{e}_k \times \mathbf{h}_k^* + \mathbf{e}_k^* \times \mathbf{h}_k)\cdot\hat{z}\, dV}{2\int_V \varepsilon_0\varepsilon_r(\mathbf{r})|e_k|^2\, dV} \\ &= \frac{2a}{\int_V \varepsilon_0\varepsilon_r(\mathbf{r})|e_k|^2\, dV} = \frac{2a}{W_k} \end{aligned} \tag{3.57}$$

Substituting eqs. 3.54 in eqs. 3.50 we get:

$$\begin{aligned}
4a\frac{\partial A_4}{\partial z} &\simeq \imath\omega_4\frac{3}{4}\varepsilon_0\int_V \chi^{(3)}(\mathbf{r})\left(|A_4|^2|\mathbf{e}_4|^2+2\sum_{l=1}^{3}|A_l|^2|\mathbf{e}_l|^2\right)A_4|\mathbf{e}_4|^2dV \\
&\quad+\imath\omega_4\frac{3}{2}\varepsilon_0\int_V \chi^{(3)}(\mathbf{r})A_1A_2A_3^*\mathbf{e}_1\mathbf{e}_2\mathbf{e}_3^*\mathbf{e}_4^*e^{-\imath\Delta\beta z}dV \\
&\simeq \imath\omega_4\frac{3}{4}\varepsilon_0\left[A_4\left(\frac{4a^2|A_4|^2\int_V\chi^{(3)}(\mathbf{r})|\mathbf{e}_4|^4\,dV}{v_{g4}^2W_4^2}\right.\right. \\
&\quad\left.+2\sum_{l=1}^{3}\frac{4a^2|A_l|^2\int_V\chi^{(3)}(\mathbf{r})|\mathbf{e}_4|^2|\mathbf{e}_l|^2\,dV}{(v_{g4}W_4)(v_{gl}W_l)}\right) \\
&\quad+2\sqrt{\frac{(2a)^4}{(v_{g1}W_1)(v_{g2}W_2)(v_{g3}W_3)(v_{g4}W_4)}} \\
&\quad\left.\left(\int_V\chi^{(3)}(\mathbf{r})\mathbf{e}_1\mathbf{e}_2\mathbf{e}_3^*\mathbf{e}_4^*\,dV\right)A_1A_2A_3^*e^{-\imath\Delta\beta z}\right].
\end{aligned} \tag{3.58}$$

The first two terms account for SPM and XPM and the third one for the FWM. Note that in the first step the hypothesis that A_k are slowly varying (constant) in the cell is used; regarding the mismatch term, $e^{-\imath\Delta\beta z}$, we are looking for nearly phase-matched interactions and so it can be also considered as slowly varying (constant) in the cell. Finally:

$$\begin{aligned}
\frac{\partial A_4}{\partial z} &\simeq \imath\frac{3a\omega_4\varepsilon_0}{4v_{g4}^2W_4^2}\left(\int_V\chi^{(3)}(\mathbf{r})|\mathbf{e}_4|^4\,dV\right)|A_4|^2A_4 \\
&\quad+\imath\sum_{l=1}^{3}\frac{3a\omega_4\varepsilon_0}{2v_{g,4l}^2W_{4l}^2}\left(\int_V\chi^{(3)}(\mathbf{r})|\mathbf{e}_4|^2|\mathbf{e}_l|^2\,dV\right)|A_l|^2A_4 \\
&\quad+\imath\frac{3a\omega_4\varepsilon_0}{2v_{g,1234}^2W_{1234}^2}\left(\int_V\chi^{(3)}(\mathbf{r})\mathbf{e}_1\mathbf{e}_2\mathbf{e}_3^*\mathbf{e}_4^*\,dV\right)A_1A_2A_3^*e^{-\imath\Delta\beta z},
\end{aligned} \tag{3.59}$$

where we defined

$$v_{g,ijkl}^2 = \sqrt{v_{g,i}v_{g,j}v_{g,k}v_{g,l}}, \tag{3.60}$$

$$v_{g,ij}^2 = v_{g,i}v_{g,j}, \tag{3.61}$$

$$W_{ijkl}^2 = \sqrt{W_iW_jW_kW_l}, \tag{3.62}$$

$$W_{ij}^2 = W_iW_j. \tag{3.63}$$

We are searching for FWM equations in a "standard" form [42]:

$$\begin{aligned}\frac{\partial A_4}{dz} = & \imath\frac{n_2\omega_4}{c}\frac{a}{V_{SPM,4}}|A_4|^2A_4 \\ & + 2\sum_{l=1}^{3}\imath\frac{n_2\omega_4}{c}\frac{a}{V_{XPM,4l}}|A_l|^2A_4 \\ & + 2\imath\frac{n_2\omega_4}{c}\frac{a}{V_{FWM,4}}A_1A_2A_3^*e^{-\imath\Delta\beta z},\end{aligned} \tag{3.64}$$

where the effective volumes are introduced in replacement of an effective area, that is meaningless in a photonic crystal, where the cross section is not constant.

By comparing the last equation with eq. 3.59, we get:

$$\frac{n_2}{cV_{SPM,4}} = \frac{3}{4}\frac{\varepsilon_0}{v_{g4}^2W_4^2}\int_V\chi^{(3)}(\mathbf{r})|\mathbf{e}_4|^4\,dV \tag{3.65}$$

$$\frac{n_2}{cV_{XPM,4l}} = \frac{3}{4}\frac{\varepsilon_0}{v_{g,4l}^2W_{4l}^2}\int_V\chi^{(3)}(\mathbf{r})|\mathbf{e}_4|^2|\mathbf{e}_l|^2\,dV \tag{3.66}$$

$$\frac{n_2}{cV_{FWM,4}} = \frac{3}{4}\frac{\varepsilon_0}{v_{g,1234}^2W_{1234}^2}\int_V\chi^{(3)}(\mathbf{r})\mathbf{e}_1\mathbf{e}_2\mathbf{e}_3^*\mathbf{e}_4^*\,dV \tag{3.67}$$

and recalling that [38]

$$n_2\left[\frac{m^2}{W}\right] = \frac{3}{4\,\varepsilon_r\,\varepsilon_0\,c}\chi^{(3)}, \tag{3.68}$$

where $\chi^{(3)}$ and ε_r are the values of the bulk, we finally obtain the definition of the effective volumes:

$$\frac{1}{V_{SPM,4}} = \frac{c^2}{v_{g4}^2}\frac{\int_V\varepsilon_r\frac{\chi^{(3)}(\mathbf{r})}{\chi^{(3)}}|\mathbf{e}_4|^4\,dV}{\left(\int_V\varepsilon_r(\mathbf{r})|\mathbf{e}_4|^2\,dV\right)^2} \tag{3.69}$$

$$\frac{1}{V_{XPM,4l}} = \frac{c^2}{v_{g,4l}^2}\frac{\int_V\varepsilon_r\frac{\chi^{(3)}(\mathbf{r})}{\chi^{(3)}}|\mathbf{e}_4|^2|\mathbf{e}_l|^2\,dV}{\left(\int_V\varepsilon_r(\mathbf{r})|\mathbf{e}_4|^2\,dV\right)\left(\int_V\varepsilon_r(\mathbf{r})|\mathbf{e}_l|^2\,dV\right)} \tag{3.70}$$

$$\frac{1}{V_{FWM,4}} = \frac{c^2}{v_{g,1234}^2}\frac{\int_V\varepsilon_r\frac{\chi^{(3)}(\mathbf{r})}{\chi^{(3)}}\mathbf{e}_1\mathbf{e}_2\mathbf{e}_3^*\mathbf{e}_4^*\,dV}{\prod_{l=1}^{4}\left(\int_V\varepsilon_r(\mathbf{r})|\mathbf{e}_l|^2\,dV\right)^{1/2}}. \tag{3.71}$$

In a similar manner, the coefficients for all the other waves can be found as well. We define

$$\gamma_i = \frac{n_2\omega_i a}{cV_{SPM,i}}, \tag{3.72}$$

$$\gamma_{il} = \frac{n_2\omega_i a}{cV_{XPM,il}}, \tag{3.73}$$

$$\gamma_{Fi} = \frac{n_2 \omega_i a}{c V_{FWM,i}}, \tag{3.74}$$

$$P_i = |A_i(0)|^2, \tag{3.75}$$

where i, $l = 1, 2, 3, 4$.

With these coefficients, the general system of equations describing the four wave mixing is:

$$\begin{aligned}
\frac{\partial A_1}{dz} =& i\left[(\gamma_1|A_1|^2 + 2\sum_{k=2,3,4}\gamma_{1k}|A_k|^2)A_1 + 2\gamma_{F1}A_2^* A_3 A_4 e^{i\Delta\beta z}\right] \\
\frac{\partial A_2}{dz} =& i\left[(\gamma_2|A_2|^2 + 2\sum_{k=1,3,4}\gamma_{2k}|A_k|^2)A_2 + 2\gamma_{F2}A_1^* A_3 A_4 e^{i\Delta\beta z}\right] \\
\frac{\partial A_3}{dz} =& i\left[(\gamma_3|A_3|^2 + 2\sum_{k=1,2,4}\gamma_{3k}|A_k|^2)A_3 + 2\gamma_{F3}A_4^* A_1 A_2 e^{-i\Delta\beta z}\right] \\
\frac{\partial A_4}{dz} =& i\left[(\gamma_4|A_4|^2 + 2\sum_{k=1,2,3}\gamma_{4k}|A_k|^2)A_4 + 2\gamma_{F4}A_3^* A_1 A_2 e^{-i\Delta\beta z}\right]
\end{aligned} \tag{3.76}$$

This general system has [42] approximate solutions by first considering the evolution of the pump fields (A_1, A_2) assuming the transfer of energy to A_3 and A_4 is negligible (undepleted pump approximation). The equations that govern the field amplitudes in this case are

$$\begin{aligned}
\frac{dA_1}{dz} =& i(\gamma_1 P_1 + 2\gamma_{12}P_2)A_1, \\
\frac{dA_2}{dz} =& i(\gamma_2 P_2 + 2\gamma_{21}P_1)A_2.
\end{aligned} \tag{3.77}$$

whose solutions are

$$\begin{aligned}
A_1(z) =& \sqrt{P_1}\exp[i(\gamma_1 P_1 + 2\gamma_{12}P_2)z], \\
A_2(z) =& \sqrt{P_2}\exp[i(\gamma_2 P_2 + 2\gamma_{21}P_1)z],
\end{aligned} \tag{3.78}$$

Then Eqs. 3.76 give

$$\begin{aligned}
\frac{dA_3}{dz} =& \imath 2(\gamma_{31}P_1 + \gamma_{32}P_2)A_3 + \imath 2\gamma_{F3}\sqrt{P_1 P_2}A_4^* e^{-i\Theta z} \\
\frac{dA_4^*}{dz} =& -\imath 2(\gamma_{41}P_1 + \gamma_{42}P_2)A_4^* - \imath 2\gamma_{F4}^*\sqrt{P_1 P_2}A_3^* e^{i\Theta z},
\end{aligned} \tag{3.79}$$

where $\Theta = \Delta\beta - (\gamma_1 + 2\gamma_{21})P_1 - (\gamma_2 + 2\gamma_{12})P_2$.

To solve these equations, we introduce

$$B_j = A_j \exp[-2\imath(\gamma_{j1}P_1 + \gamma_{j2}P_2)z], \quad j = 3, 4 \tag{3.80}$$

and we obtain

$$\begin{aligned} \frac{dB_3}{dz} =& 2\imath\gamma_{F3}\sqrt{P_1P_2}e^{-\imath\eta z}B_4^* \\ \frac{dB_4^*}{dz} =& -2\imath\gamma_{F4}^*\sqrt{P_1P_2}e^{\imath\eta z}B_3 \end{aligned} \tag{3.81}$$

where

$$\begin{aligned} \eta = \Delta\beta &- (\gamma_1 + 2\gamma_{21} - 2\gamma_{31} - 2\gamma_{41})P_1 + \\ &- (\gamma_2 + 2\gamma_{12} - 2\gamma_{32} - 2\gamma_{42})P_2. \end{aligned} \tag{3.82}$$

We can transform the system 3.81 in the following two second-order differential homogeneous equations

$$\frac{d^2B_3}{dz^2} + \imath\eta\frac{dB_3}{dz} - 4\gamma_{F3}\gamma_{F4}^*P_1P_2B_3 = 0 \tag{3.83}$$

$$\frac{d^2B_4^*}{dz^2} - \imath\eta\frac{dB_4^*}{dz} - 4\gamma_{F3}^*\gamma_{F4}P_1P_2B_4^* = 0. \tag{3.84}$$

Their general solution is in the form

$$B_3(z) = \quad (a_4e^{gz} + b_4e^{-gz})\exp(-\imath\eta z/2) \tag{3.85}$$

$$B_4^*(z) = \quad (a_4e^{gz} + b_4e^{-gz})\exp(\imath\eta z/2) \tag{3.86}$$

where $a_j, b_j, j = 3, 4$, depend from initial conditions, and

$$g = \sqrt{4\gamma_{F3}\gamma_{F4}^*P_1P_2 - (\eta/2)^2}. \tag{3.87}$$

If we consider the degenerate case with one pump ($\omega_1 = \omega_2$, $A_1 = A_2$ and consequently $\gamma_1 = \gamma_2 = \gamma_{12} = \gamma_{21} = \gamma_p$, and $P_1 = P_2 = P/2$), we find

$$\eta = \quad \Delta k - (3\gamma_p - 2\gamma_{3p} - 2\gamma_{4p})P, \tag{3.88}$$

$$g = \quad \sqrt{\gamma_{F3}\gamma_{F4}^*P^2 - (\eta/2)^2}, \tag{3.89}$$

$$G = \quad 1 + \frac{\gamma_{F3}\gamma_{F4}^*}{g^2}P^2\sinh^2(gL), \tag{3.90}$$

where G is the amplification factor and L the length of the waveguide.

Chapter 4

Fabrication Process and Disorder

One of the most interesting similarities between real crystals and photonic ones is the presence of disorder. We can define disorder as anything breaking symmetry properties of the lattice.

It can take many forms, but we usually can divide it into two group. The first one is represented by any defect we deliberately introduce in the lattice and allow the realization of photonic crystal based devices as waveguides, filters, etc; it is also called *intrinsic disorder*. Instead, the second group contains the defects due to noise in the lattice and unit cell parameters introduced by the fabrication process and it cause diffraction losses in the propagating fields destroying the photonic confinement ability of the device; it is called *extrinsic disorder*. We will focus on this second type of disorder, but before to study it in detail, it is important to have a clear prospect about the fabrication process of a 2D photonic crystal device.

4.1 Fabrication of 2D Photonic Crystal Devices

Despite their geometry simplicity, the fabrication of a two dimensional photonic crystal device is quite complicate and requires several full featured facilities.

The final application of the desired device determine the necessary starting material; for example, Gallium Arsenide based substrates are most common for light emitting devices, while Silicon is commonly used for waveguiding purposes. After the decision about the material, the subsequent step is to purchase the substrate wafer from a specialized company.

The core process of the device fabrication is lithography, from the Greek $\lambda\iota\theta o\varsigma$,

lithos, that means stone plus $\gamma\rho\alpha\phi\omega$, *graph*, that means to write. It is the process of transferring designed device patterns to the wafer, by selectively removing parts of the bulk of the substrate.

A single iteration of lithography combines several steps in sequence (see Fig.4.1).

Cleaning and Preparation The wafer is initially heated to the temperature adeguate to drive off any moisture that may be present on the surface. If other contaminations are present on the wafer surface, they are removed by wet chemical treatment.

Resist application The wafer is covered with a sensitive material, called *photoresist*, or simply resist, by spin coating. In some cases, a liquid or gaseous adhesion promoter is applied to promote adhesion of the resist to the wafer. Then, a viscous, liquid solution of resist is dispensed onto the wafer, and the wafer is spun rapidly (between 1200 and 4800 rpm) for 30 to 60 seconds to produce a layer of resist with a thickness between 0.5 and 2.5µm and a uniformity of within 5 to 10 nm. The resist-coated wafer is then prebaked to drive off excess, typically at 90 to 100 °C for 30 to 60 seconds on a hotplate.

Exposure and developing After prebaking, the resist is exposed to a pattern of intense light or an electron beam. This difference divide lithography into two great families: serial lithography, where the pattern, drawn with the help of a computer aided design (CAD) software, is directly plotted on the resist, and parallel lithography, where the geometrical pattern is on masks that shadow the incoming radiation and is transferred on the resist in one single shot. The most known example of the first group is the Electron Beam Lithography (EBL), consisting in exposing the resist layer through an electron beam which position is controlled by a computer, while photolithography is the most common of the second family and it is widely used in semiconductor industry. Two type of resist exist. *Positive* one is the most common type and becomes soluble in the basic developer when exposed; *negative* resist becomes insoluble in the (organic) developer. This chemical change allows some of the resist to be removed by a special solution, called developer by analogy with photographic developer. A post-exposure bake is performed before developing, typically to help reduce standing wave phenomena caused by the destructive and constructive interference patterns of the incident light. The develop chemistry is delivered on a spinner, much like resist. The resulting wafer is then hard-baked typically at

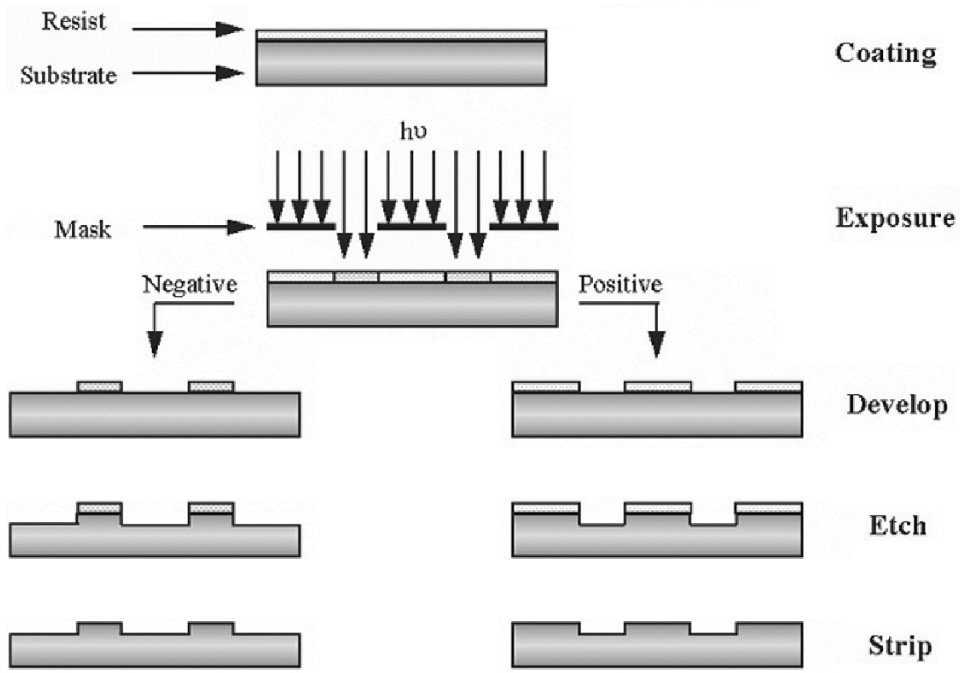

Figure 4.1: Diagram of a parallel lithography process.

120 to 180 °C for 20 to 30 minutes. The hard bake solidifies the remaining resist, to make a more durable protecting layer for the future steps.

Etching In etching, a liquid (*wet*) or plasma (*dry*) chemical agent removes the uppermost layer of the substrate in the areas that are not protected by resist. In semiconductor fabrication, dry etching techniques are generally used, as they can be made anisotropic, in order to avoid significant undercutting of the resist pattern. This is essential when the width of the features to be defined is similar to or less than the thickness of the material being etched (i.e. when the aspect ratio approaches unity). Wet etch processes are generally isotropic in nature, which is often indispensable for MEMS, where suspended structures must be released from the underlying layer.

Ashing After resist is no longer needed, it must be removed from the substrate. This usually requires a liquid resist stripper, which chemically alters the resist so that it no longer adheres to the substrate. Alternatively, resist may be removed by a plasma containing oxygen, which oxidizes it.

Since the typical size of the features of 2D photonic crystal is of the order of 100 nm, the required accuracy is about 10 nm or less, and the lithographic resolution

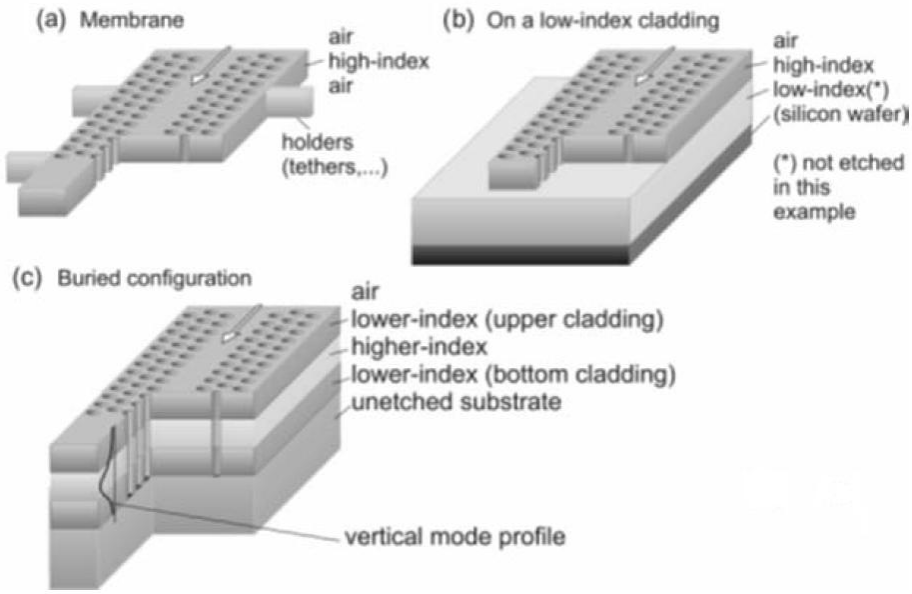

Figure 4.2: (a) Straight photonic crystal waveguide defined on a membrane. (b) Same object defined on a low-index cladding. (c) Same object defined in a buried configuration, the multilayer structure corresponding, for instance, to a standard laser diode. The vertical mode profile is sketched[4].

has to be more or less of the same order, optical lithography results inadequate, so that the most adequate method for the definition of photonic crystal patterns in semiconductor substrates is the electron-beam (e-beam) lithography: a focused electron beam, with a typical spot size below 10 nm, scans all the parts of the resist which are to be dissolved. The possibility of using deep-ultraviolet (DUV) lithography with the projection of a mask at a high resolution has also been demonstrated recently [43]. This method should be preferred for mass production as its throughput is an order of magnitude higher than with serial e-beam lithography. Further, this method is undoubtedly in a position of benefiting from the current advances in the miniaturization of silicon microelectronics, where the size of the grids for transistor gates is expected to fall well below 40 nm within the next few years. The X-Ray Lithography is also a suitable tool for its good throughput and resolution, but needs an intermediated mask to be duplicate on the final substrate using EBL. Finally, the possibility of using laser holography has also been considered, above all for 3D photonic crystals. This technique allows only the fabrication of uniform crystals, and does not seem to be well-suited to the realization of periodicity defects in photonic

crystals, which is essential for the implementation of genuine optoelectronic devices.

After having correctly defined the mask and the corresponding set of etching steps, the three main possible implementations are represented in Fig. 4.2. A straight photonic crystal waveguide has been chosen here as a visual example. It consists of a line of missing holes along a direction of the photonic crystal.

The membrane (Fig. 4.2a) is apparently the simplest case, but its fabrication process is quite complex from a technological point of view, because the presence of a sacrificial layer under the waveguide that has to be removed by chemical etching. The case of a low index substrate is generally the simplest in terms of etching (Fig. 4.2b). The case of a buried waveguide (Fig. 4.2c) is of great interest as regards technological integration, but its implementation imposes very demanding requirements in terms of deep etching.

4.2 Disorder in 2D photonic crystal waveguide

The extrinsic disorder collects all the random fabrication variations and represent one of the most critical hurdles facing the development of PhC and PhC-based devices. In this work, we will focus on arbitrary PhC waveguides and we will use the formalism introduced by Sakoda [4] and Hughes [44], that yields explicit formulae for both the backscattered and total transmission loss due to disorder imperfections.

Because the fabrication process, the real structure differs from the ideal one. As PC materials can be described entirely by their permittivity[1] $\varepsilon(\mathbf{r})$, we can introduce the disorder function as the difference between the real and the ideal permittivity

$$\Delta\varepsilon(\mathbf{r}) \equiv \varepsilon(\mathbf{r}) - \varepsilon_i(\mathbf{r}). \tag{4.1}$$

We consider, moreover, that the ideal structure is periodic along the defect direction; we assume this direction as the x direction and the waveguides periodic along it with period a

$$\varepsilon_i(\mathbf{r}) = \varepsilon_i(\mathbf{r} + ma\hat{\mathbf{x}}), \tag{4.2}$$

where $\hat{\mathbf{x}}$ is the unit vector in the x direction, and m is an integer. Furthermore, we indicate with L the length of the waveguides and V the volume of the unit cell; it is bounded in the x direction by the period a and unbounded in the y and z directions.

The idea is to calculate the unperturbed field, solution of Maxwell equations for the ideal structure, and then apply the Marcuse perturbation equations.

[1] We consider that permettivity is frequency independent: $\varepsilon(\mathbf{r}, \omega) \equiv \varepsilon(\mathbf{r})$

By considering the Maxwell's equations in the frequency domain

$$\nabla \cdot \varepsilon(\mathbf{r})\mathbf{E}(\mathbf{r},\omega) = 0 \tag{4.3a}$$
$$\nabla \cdot \mathbf{B}(\mathbf{r},\omega) = 0 \tag{4.3b}$$
$$\nabla \times \mathbf{E}(\mathbf{r},\omega) = -\imath\omega\mu_0\mathbf{H}(\mathbf{r},\omega) \tag{4.3c}$$
$$\nabla \times \mathbf{H}(\mathbf{r},\omega) = +\imath\omega\varepsilon_0\varepsilon(\mathbf{r})\mathbf{E}(\mathbf{r},\omega). \tag{4.3d}$$

we obtain the wave equation for the electric field

$$\nabla \times \nabla \times \mathbf{E}(\mathbf{r},\omega) = \frac{\omega^2}{c^2}\varepsilon(\mathbf{r})\mathbf{E}(\mathbf{r},\omega), \tag{4.4}$$

that can be written as

$$\nabla \times \nabla \times \mathbf{E}(\mathbf{r},\omega) - \frac{\omega^2}{c^2}\varepsilon_i(\mathbf{r})\mathbf{E}(\mathbf{r},\omega) = \frac{\omega^2}{c^2}\mathbf{\Delta P}(\mathbf{r},\omega), \tag{4.5}$$

with $\mathbf{\Delta P}(\mathbf{r},\omega) \equiv \Delta\varepsilon(\mathbf{r})\mathbf{E}(\mathbf{r},\omega)$.

By introducing the operator[2] $\hat{\Theta} = \nabla \times \nabla\times$, we obtain

$$\left(-\frac{\omega^2}{c^2}\varepsilon_i(\mathbf{r}) + \hat{\Theta}\right)\mathbf{E}(\mathbf{r},\omega) = \frac{\omega^2}{c^2}\mathbf{\Delta P}(\mathbf{r},\omega). \tag{4.6}$$

The solution of (4.4) is obtained from the implicit Lippmann-Schwinger equation

$$\mathbf{E}(\mathbf{r},\omega) = \mathbf{E}_0(\mathbf{r},\omega) + \int_D \overleftrightarrow{G}(\mathbf{r},\mathbf{r}',\omega)\cdot\mathbf{\Delta P}(\mathbf{r}',\omega)d\mathbf{r}' \tag{4.7}$$

where the first term $\mathbf{E}_0(\mathbf{r},\omega)$ is referred to as the incident field, while the second one is the scattered field obtained from the integration over the domain D, that is the part of the volume V, where $\mathbf{\Delta P}$ is non-zero.

To solve the Lippmann-Schwinger equation, we need to know the analytical solution $\mathbf{E}_0(\mathbf{r},\omega)$ of the homogeneous equation

$$\nabla \times \nabla \times \mathbf{E}_0(\mathbf{r},\omega) - \frac{\omega^2}{c^2}\varepsilon_i(\mathbf{r})\mathbf{E}_0(\mathbf{r},\omega) = 0, \tag{4.8}$$

and the associated Green dyadic defined by

$$\nabla \times \nabla \times \overleftrightarrow{G}(\mathbf{r},\mathbf{r}',\omega) - \frac{\omega^2}{c^2}\varepsilon_i(\mathbf{r})\overleftrightarrow{G}(\mathbf{r},\mathbf{r}',\omega) = \frac{\omega^2}{c^2}\delta(\mathbf{r}-\mathbf{r}')\overleftrightarrow{I}. \tag{4.9}$$

[2] This operator is different from the one defined in Eq. 1.11.

It is difficult to find the analytic form of (4.7) since $\mathbf{E}$ appears within the integration. Then, we suppose to work in condition of weak scattering, so that we can consider the Born expansion

$$\begin{aligned}\mathbf{E}(\mathbf{r},\omega) = \mathbf{E}_0(\mathbf{r},\omega) \\ + \int_D \overleftrightarrow{G}(\mathbf{r},\mathbf{r}',\omega)\cdot\Delta\varepsilon(\mathbf{r}')\mathbf{E}_0(\mathbf{r}',\omega)d\mathbf{r}' \\ + \int_D\int_D \overleftrightarrow{G}(\mathbf{r},\mathbf{r}',\omega)\cdot\overleftrightarrow{G}(\mathbf{r}',\mathbf{r}'',\omega)\cdot\Delta\varepsilon(\mathbf{r}')\Delta\varepsilon(\mathbf{r}'')\mathbf{E}_0(\mathbf{r}'',\omega)d\mathbf{r}''d\mathbf{r}' \\ + \dots .\end{aligned} \tag{4.10}$$

We truncated the expansion after the first three terms because the volume D is very small and the contribution of terms with order higher than $(\Delta\varepsilon(\mathbf{r}))^2$ is negligible.

4.2.1 Solution of the homogeneous equation

The propagating mode solutions are obtained from the eq. (4.8), which here we rewrite by using the $\hat{\Theta}$ operator

$$\frac{1}{\varepsilon_i(\mathbf{r})}\hat{\Theta}\mathbf{E}_0(\mathbf{r},\omega) = \frac{\omega^2}{c^2}\mathbf{E}_0(\mathbf{r},\omega). \tag{4.11}$$

The operator $\hat{\Theta}$ is a Hermitian operator[3]. Therefore, its eigenfunctions form an orthogonal complete set. These eigenfunctions are classified into transverse-wave solutions $\mathbf{E}^{\mathrm{T}}_{\mathbf{k}}(\mathbf{r})$ and longitudinal-wave solutions $\mathbf{E}^{\mathrm{L}}_{\mathbf{k}}(\mathbf{r})$.

[3]The inner product of two periodic complex functions $\mathbf{F_1}(\mathbf{r})$ e $\mathbf{F_2}(\mathbf{r})$ is defined by

$$< \mathbf{F_1}(\mathbf{r}), \mathbf{F_2}(\mathbf{r}) >= \int_V \mathbf{F_1}^*(\mathbf{r})\cdot\mathbf{F_2}(\mathbf{r})d\mathbf{r}, \tag{4.12}$$

where V is the volume on which the periodic boundary condition is imposed. Applying these definitions to our case, we obtain

$$< \hat{\Theta}\mathbf{F_1}(\mathbf{r}), \mathbf{F_2}(\mathbf{r}) >= \int_V [\nabla\times\{\nabla\times\mathbf{F_1}^*(\mathbf{r})\}]\cdot\mathbf{F_2}(\mathbf{r})d\mathbf{r}. \tag{4.13}$$

Using the following vector identity

$$\nabla\cdot(\mathbf{A}\times\mathbf{B}) = (\nabla\times\mathbf{A})\cdot\mathbf{B} - \mathbf{A}\cdot(\nabla\times\mathbf{B}) \tag{4.14}$$

the (4.13) becomes

$$\begin{aligned}< \hat{\Theta}\mathbf{F_1}(\mathbf{r}), \mathbf{F_2}(\mathbf{r}) >= \int_S [\{\nabla\times\mathbf{F_1}^*(\mathbf{r})\}\times\mathbf{F_2}(\mathbf{r})]dS \\ + \int_V \{\nabla\times\mathbf{F_1}^*(\mathbf{r})\}\cdot\{\nabla\times\mathbf{F_2}(\mathbf{r})\}d\mathbf{r}\end{aligned} \tag{4.15}$$

The equations that characterize these solutions are

$$\nabla \cdot \varepsilon_i(\mathbf{r})\mathbf{E}^{\mathrm{T}}_{\mathbf{k}}(\mathbf{r}) = \mathbf{0}, \tag{4.17}$$

and

$$\nabla \times \mathbf{E}^{\mathrm{L}}_{\mathbf{k}}(\mathbf{r}) = 0. \tag{4.18}$$

Note that $\mathbf{E}^{\mathrm{T}}_{\mathbf{k}}(\mathbf{r})$ and $\mathbf{E}^{\mathrm{L}}_{\mathbf{k}}(\mathbf{r})$ are not purely transverse nor longitudinal, because of the spatial variation of $\varepsilon_i(\mathbf{r})$, the terms are adopted because of when $\varepsilon_i(\mathbf{r})$ is a constant the equations become the usual relations defining transverse and longitudinal waves, respectively.

For each transverse solution, we can write the associated equation

$$\frac{1}{\varepsilon_i(\mathbf{r})}\nabla \times \nabla \times \mathbf{E}^{\mathrm{T}}_{\mathbf{k}}(\mathbf{r}) = \frac{\omega^2_{\mathbf{k}}}{c^2}\mathbf{E}^{\mathrm{T}}_{\mathbf{k}}(\mathbf{r}), \tag{4.19}$$

where $\mathbf{k}$ and $\omega_{\mathbf{k}}$ are respectively the wavevector and the eigenvalue corresponding to the eigenfunction $\mathbf{E}_{\mathbf{k}}(\mathbf{r})$, while the eigenvalue of the longitudinal mode is zero.

Now, we normalize these wave functions as follows

$$\int_V \varepsilon_i(\mathbf{r})(\mathbf{E}^{\alpha}_{\mathbf{k}}(\mathbf{r}))^* \cdot \mathbf{E}^{\beta}_{\mathbf{k}'}(\mathbf{r})d\mathbf{r} = \delta_{\mathbf{k}\mathbf{k}'}\delta_{\alpha\beta}, \tag{4.20}$$

with $\alpha, \beta = T$ or L.

The completeness of the eigenfunctions [4] leads to

$$|\varepsilon_i(\mathbf{r})| \sum_{\mathbf{k}} \left[\mathbf{E}^{\mathrm{T}}_{\mathbf{k}}(\mathbf{r}) \otimes (\mathbf{E}^{\mathrm{T}}_{\mathbf{k}}(\mathbf{r}'))^* + \mathbf{E}^{\mathrm{L}}_{\mathbf{k}}(\mathbf{r}) \otimes (\mathbf{E}^{\mathrm{L}}_{\mathbf{k}}(\mathbf{r}'))^*\right] = \delta(\mathbf{r}-\mathbf{r}') \overleftrightarrow{I}, \tag{4.21}$$

where $\overleftrightarrow{I}$ is the unitary tensor, and we use $|\varepsilon_i(\mathbf{r})|$ because of $\varepsilon_i(\mathbf{r}) \in \mathbb{C}$ generically.

---

where S denotes the surface of the volume V. The surface integral is zero because of the periodic boundary condition. Applying again the identity (4.14), we find

$$\begin{aligned} < \hat{\Theta}\mathbf{F_1}(\mathbf{r}), \mathbf{F_2}(\mathbf{r}) > = & \int_S [\mathbf{F_1}^*(\mathbf{r}) \times \{\nabla \times \mathbf{F_2}(\mathbf{r})\}]dS \\ & + \int_V \mathbf{F_1}^*(\mathbf{r}) \cdot [\nabla \times \{\nabla \times \mathbf{F_2}(\mathbf{r})\}]d\mathbf{r} \\ = & < \mathbf{F_1}(\mathbf{r}), \hat{\Theta}\mathbf{F_2}(\mathbf{r}) >, \end{aligned} \tag{4.16}$$

where we have again used the fact that the surface integral is equal to zero. The operator $\hat{\Theta}$ is, therefore, Hermitian.

Applying the Bloch's theorem to the eq. (4.11) and considering only the value of $\mathbf{k}$ in the x direction so that k is scalar, we can express the eigenfunctions in terms of Bloch function

$$\mathbf{E}_k^T(\mathbf{r}) = \sqrt{\frac{a}{L}}\mathbf{e}_k(\mathbf{r})\mathrm{e}^{\imath kx}. \tag{4.22}$$

We remember here that the Bloch functions have the following properties

$$\mathbf{e}_k(\mathbf{r}) = \mathbf{e}_k(\mathbf{r} + \hat{\mathbf{x}}ma), \qquad \mathbf{e}_k(\mathbf{r}) = \mathbf{e}^*_{-k}(\mathbf{r}), \tag{4.23}$$

and we normalize them according to

$$\int_V \varepsilon_i(\mathbf{r}) \left[\mathbf{e}^*_{k_n}(\mathbf{r}) \cdot \mathbf{e}_{k_m}(\mathbf{r})\right] d\mathbf{r} = \delta_{nm}. \tag{4.24}$$

To set the homogeneous solution, we consider the dispersion relation $\omega(k)$ and a fixed frequency ω_0 and we suppose there to be multiple solutions to $\omega(k) = \omega_0$, and these solutions are $k_n, n \in [1, N_0]$. For different ω, the value of N_0 can change. So we consider a function $N(\omega)$ that gives the number of solutions of the equation $\omega(k) = \omega_0$, $N_0 = N(\omega_0)$.

We set the homogeneous solution as the sum of all the forward propagating modes at the frequency ω_0

$$\mathbf{E}_0(\mathbf{r}, \omega_0) \equiv \sqrt{\frac{a}{L}} \sum_{n=1}^{N_0} \mathbf{e}_{k_n}(\mathbf{r})\mathrm{e}^{\imath k_n x}. \tag{4.25}$$

4.2.2 Green function tensor

The Green function can be expressed in terms of the eigenfunctions $\mathbf{E}_\mathbf{k}$ in the sum

$$\begin{aligned}\overleftrightarrow{G}(\mathbf{r}, \mathbf{r}', \omega) = &\sum_{\mathbf{k}} \frac{\omega^2}{\omega_\mathbf{k}^2 - (\omega + \imath\delta)^2} \mathbf{E}^{\mathrm{T}}_\mathbf{k}(\mathbf{r}) \otimes \left(\mathbf{E}^{\mathrm{T}}_\mathbf{k}(\mathbf{r}')\right)^* \\ &- \frac{\omega^2}{(\omega + \imath\delta)^2} \sum_{\mathbf{k}} \mathbf{E}^{\mathrm{L}}_\mathbf{k}(\mathbf{r}) \otimes \left(\mathbf{E}^{\mathrm{L}}_\mathbf{k}(\mathbf{r}')\right)^*,\end{aligned} \tag{4.26}$$

where $\otimes$ denotes the dyadic product[4] and δ is a positive infinitesimal that assure the causality of the solution of the eq. (4.5). Using (4.21), the Green function tensor can be written as

$$\overleftrightarrow{G}(\mathbf{r}, \mathbf{r}', \omega) = \frac{\omega^2}{(\omega + \imath\delta)^2} \left(\sum_{\mathbf{k}} \omega_\mathbf{k}^2 \frac{\mathbf{E}^{\mathrm{T}}_\mathbf{k}(\mathbf{r}) \otimes \left(\mathbf{E}^{\mathrm{T}}_\mathbf{k}(\mathbf{r}')\right)^*}{\omega_\mathbf{k}^2 - (\omega + \imath\delta)^2} - \frac{\delta(\mathbf{r} - \mathbf{r}')}{|\varepsilon_i(\mathbf{r})|} \overleftrightarrow{I} \right). \tag{4.29}$$

[4]The dyadic product $\mathbf{A}$ of two vectors, $\mathbf{u} = [u_1, \ldots, u_m]^T$ and $\mathbf{v} = [v_1, \ldots, v_n]^T$, is defined as

It is possible to divide the last equation in three different part. The first one takes in the modes which propagate in the x direction and, then, have the associated wavevectors written as a scalar quantity k

$$\overleftrightarrow{G}_{prop}(\mathbf{r},\mathbf{r}',\omega) = \frac{\omega^2}{(\omega+\imath\delta)^2}\sum_k \frac{\omega_k^2}{\omega_k^2-(\omega+\imath\delta)^2}\mathbf{E}_k^{\mathrm{T}}(\mathbf{r})\otimes\left(\mathbf{E}_k^{\mathrm{T}}(\mathbf{r}')\right)^*. \tag{4.30}$$

The second part, $\overleftrightarrow{G}_{rad}$, includes the radiative modes and the delta function term, that comprises all the quasi-longitudinal modes and contributes only to the real part of $\overleftrightarrow{G}$ at $\mathbf{r}=\mathbf{r}'$

$$\overleftrightarrow{G} = \overleftrightarrow{G}_{prop} + \overleftrightarrow{G}_{rad}. \tag{4.31}$$

We can write explicitly $\overleftrightarrow{G}_{prop}$, by considering the Bloch functions

$$\overleftrightarrow{G}_{prop}(\mathbf{r},\mathbf{r}',\omega) = \frac{a}{L}\frac{\omega^2}{(\omega+\imath\delta)^2}\sum_k \frac{\omega_k^2}{\omega_k^2-(\omega+\imath\delta)^2}\mathbf{e}_k(\mathbf{r})\otimes\mathbf{e}_k^*(\mathbf{r}')\mathrm{e}^{\imath k(x-x')}, \tag{4.32}$$

and by extending k as a continuous variable and by converting the sum over k into an integral[5], we obtain

$$\begin{aligned}\overleftrightarrow{G}_{prop}(\mathbf{r},\mathbf{r}',\omega) =& \frac{L}{2\pi}\frac{\omega^2}{(\omega+\imath\delta)^2}\int_{-\infty}^{\infty}\mathbf{E}_k^{\mathrm{T}}(\mathbf{r})\otimes\left(\mathbf{E}_k^{\mathrm{T}}(\mathbf{r}')\right)^* dk \\ =& \frac{a}{2\pi}\frac{\omega^2}{(\omega+\imath\delta)^2}\int_{-\infty}^{\infty}\frac{\omega^2(k)}{\omega^2(k)-(\omega+\imath\delta)^2}\mathbf{e}_k(\mathbf{r})\otimes\mathbf{e}_k^*(\mathbf{r}')\mathrm{e}^{\imath k(x-x')}dk,\end{aligned} \tag{4.33}$$

where $\omega(k)$ is the continuous dispersion relation.

Before to integrate this formula, we suppose there to be multiple solutions to $\omega(k)=\omega_0$, and these solutions are $k_n, n\in[1,N_0]$. Integrating and letting $\delta\to 0$, we

---

the matrix obtained by multiplying $\mathbf{u}$ as a column vector by $\mathbf{v}$ as a row vector

$$\mathbf{A}=\mathbf{u}\otimes\mathbf{v}=\mathbf{u}\cdot\mathbf{v}^T=\begin{bmatrix}u_1v_1 & \dots & u_1v_n\\ \vdots & \ddots & \vdots\\ u_mv_1 & \dots & u_mv_n\end{bmatrix} \tag{4.27}$$

Consider three vectors $\mathbf{u},\mathbf{v},\mathbf{w}$ with the same dimensions. We have this interesting property that we use extensively:

$$(\mathbf{u}\otimes\mathbf{v})\cdot\mathbf{w}=(\mathbf{v}\cdot\mathbf{w})\mathbf{u}, \tag{4.28}$$

where the result of the product $\mathbf{v}\cdot\mathbf{w}$ is a scalar.

[5]The conversion is $\sum_k \to \frac{L}{2\pi}\int_{-\infty}^{\infty}dk$

obtain

$$\begin{aligned}\overleftrightarrow{G}_{prop}(\mathbf{r},\mathbf{r}',\omega_0) = &\sum_{n=1}^{N_0} \imath\frac{L\omega_0}{2v_{g,n}}\left[\mathbf{E}^T_{k_n}(\mathbf{r})\otimes(\mathbf{E}^T_{k_n}(\mathbf{r}'))^*\Theta(x-x')\right.\\ &\left.+(\mathbf{E}^T_{k_n}(\mathbf{r}))^*\otimes\mathbf{E}^T_{k_n}(\mathbf{r}')\Theta(x'-x)\right]\\ = &\imath\frac{a\omega_0}{2}\sum_{n=1}^{N_0}\frac{1}{v_{g,n}}\left[\mathbf{e}_{k_n}(\mathbf{r})\otimes\mathbf{e}^*_{k_n}(\mathbf{r}')\mathrm{e}^{\imath k_n(x-x')}\Theta(x-x')\right.\\ &\left.+\mathbf{e}^*_{k_n}(\mathbf{r})\otimes\mathbf{e}_{k_n}(\mathbf{r}')\mathrm{e}^{\imath k_n(x'-x)}\Theta(x'-x)\right],\end{aligned} \tag{4.34}$$

where $v_{g,n}\equiv\frac{d\omega}{dk}\big|_{k=k_n}$ and $\Theta(x)$ is the Heaviside function.

4.2.3 The loss expressions

We consider the electric field at frequency ω_0 as sum of all the modes[6] of the waveguide at the same frequency along the direction of propagation, as already defined in Eq. 4.25:

$$\mathbf{E}_0(\mathbf{r},\omega_0)\equiv\sum_{n=1}^{N(\omega_0)}\mathbf{E}^T_{k_n}=\sqrt{\frac{a}{L}}\sum_{n=1}^{N(\omega_0)}\mathbf{e}_{k_n}(\mathbf{r})\mathrm{e}^{\imath k_n x}. \tag{4.35}$$

To simplify the notation, from now on, we will neglect the prime T in the notation of the mode. Besides, we will neglect the explicit dependence of the fields from ω except when it is important for a better comprehension.

We come back to consider Eq. 4.10. By using Eqs. 4.34 and 4.31, the electric field that comes from the second term is:

$$\begin{aligned}\mathbf{E}_1(\mathbf{r}) \equiv &\int_D \overleftrightarrow{G}(\mathbf{r},\mathbf{r}')\cdot\Delta\varepsilon(\mathbf{r}')\mathbf{E}_0(\mathbf{r}')d\mathbf{r}'\\ = &\sum_{n=1}^{N(\omega)}\imath\frac{L\omega}{2v_{g,n}}\mathbf{E}_{k_n}(\mathbf{r})\int_D\Delta\varepsilon(\mathbf{r}')\mathbf{E}^*_{k_n}(\mathbf{r}')\cdot\mathbf{E}_0(\mathbf{r}')\Theta(x-x')d\mathbf{r}'\\ &+\sum_{n=1}^{N(\omega)}\imath\frac{L\omega}{2v_{g,n}}\mathbf{E}^*_{k_n}(\mathbf{r})\int_D\Delta\varepsilon(\mathbf{r}')\mathbf{E}_{k_n}(\mathbf{r}')\cdot\mathbf{E}_0(\mathbf{r}')\Theta(x'-x)d\mathbf{r}'\\ &+\int_D\overleftrightarrow{G}_{rad}(\mathbf{r},\mathbf{r}')\cdot\Delta\varepsilon(\mathbf{r}')\mathbf{E}_0(\mathbf{r}')d\mathbf{r}'\\ = &\mathbf{E}_{p1}(\mathbf{r})+\mathbf{E}_{p2}(\mathbf{r})+\mathbf{E}_r(\mathbf{r})\end{aligned} \tag{4.36}$$

[6] When we consider all the modes at a certain frequency, we have to consider not only the propagating mode below the light line, but also the leaky modes above the light line.

while the third term give us

$$\begin{aligned}\mathbf{E}_2(\mathbf{r}) \equiv & \int_D \int_D \overleftrightarrow{G}(\mathbf{r},\mathbf{r}') \cdot \overleftrightarrow{G}(\mathbf{r}',\mathbf{r}'') \cdot \Delta\varepsilon(\mathbf{r}')\Delta\varepsilon(\mathbf{r}'')\mathbf{E}_0(\mathbf{r}'')d\mathbf{r}''d\mathbf{r}' \\ = & \sum_{n=1}^{N(\omega)} \imath\frac{L\omega}{2v_{g,n}}\mathbf{E}_{k_n}(\mathbf{r}) \int_D \Delta\varepsilon(\mathbf{r}')\mathbf{E}^*_{k_n}(\mathbf{r}') \cdot \mathbf{E}_1(\mathbf{r}')\Theta(x-x')d\mathbf{r}' \\ & + \sum_{n=1}^{N(\omega)} \imath\frac{L\omega}{2v_{g,n}}\mathbf{E}^*_{k_n}(\mathbf{r}) \int_D \Delta\varepsilon(\mathbf{r}')\mathbf{E}_{k_n}(\mathbf{r}') \cdot \mathbf{E}_1(\mathbf{r}')\Theta(x'-x)d\mathbf{r}' \\ & + \int_D \overleftrightarrow{G}_{rad}(\mathbf{r},\mathbf{r}') \cdot \Delta\varepsilon(\mathbf{r}')\mathbf{E}_1(\mathbf{r}')d\mathbf{r}'\end{aligned} \tag{4.37}$$

By combining the equations 4.10, 4.36 and 4.37, the electric field results:

$$\begin{aligned}\mathbf{E}(\mathbf{r}) &= \mathbf{E}_0(\mathbf{r}) + \mathbf{E}_1(\mathbf{r}) + \mathbf{E}_2(\mathbf{r}) \\ &= \mathbf{E}_0(\mathbf{r}) + \int_D \overleftrightarrow{G}_{rad}(\mathbf{r},\mathbf{r}') \cdot \Delta\varepsilon(\mathbf{r}') \left(\mathbf{E}_0 + \mathbf{E}_1\right)(\mathbf{r}') \, d\mathbf{r}' \\ &\quad + \sum_{n=1}^{N(\omega)} \imath\frac{L\omega}{2v_{g,n}}\mathbf{E}_{k_n}(\mathbf{r}) \int_D \Delta\varepsilon(\mathbf{r}')\mathbf{E}^*_{k_n}(\mathbf{r}') \cdot \left(\mathbf{E}_0 + \mathbf{E}_1\right)(\mathbf{r}') \, \Theta(x-x')d\mathbf{r}' \\ &\quad + \sum_{n=1}^{N(\omega)} \imath\frac{L\omega}{2v_{g,n}}\mathbf{E}^*_{k_n}(\mathbf{r}) \int_D \Delta\varepsilon(\mathbf{r}')\mathbf{E}_{k_n}(\mathbf{r}') \cdot \left(\mathbf{E}_0 + \mathbf{E}_1\right)(\mathbf{r}') \, \Theta(x'-x)d\mathbf{r}' \\ &= \mathbf{E}_0(\mathbf{r}) + \sum_{n=1}^{N(\omega)} \imath\frac{L\omega}{2v_{g,n}}\mathbf{E}_{k_n}(\mathbf{r}) \int_D A^+_n(\mathbf{r}')\Theta(x-x')d\mathbf{r}' \\ &\quad + \sum_{n=1}^{N(\omega)} \imath\frac{L\omega}{2v_{g,n}}\mathbf{E}^*_{k_n}(\mathbf{r}) \int_D A^-_n(\mathbf{r}')\Theta(x'-x)d\mathbf{r}' \\ &\quad + \int_D \overleftrightarrow{G}_{rad}(\mathbf{r},\mathbf{r}') \cdot \Delta\varepsilon(\mathbf{r}') \left(\mathbf{E}_0 + \mathbf{E}_1\right)(\mathbf{r}') \, d\mathbf{r}'\end{aligned} \tag{4.38}$$

where the explicit form of A^+_n, A^-_n are respectively:

$$\begin{aligned}A^+_n(\mathbf{r}',\omega) &= \Delta\varepsilon(\mathbf{r}')\mathbf{E}^*_{k_n}(\mathbf{r}') \cdot (\mathbf{E}_0(\mathbf{r}',\omega) + \mathbf{E}_1(\mathbf{r}',\omega)), \\ A^-_n(\mathbf{r}',\omega) &= \Delta\varepsilon(\mathbf{r}')\mathbf{E}_{k_n}(\mathbf{r}') \cdot (\mathbf{E}_0(\mathbf{r}',\omega) + \mathbf{E}_1(\mathbf{r}'),\omega).\end{aligned} \tag{4.39}$$

We can observe that the electric field is sum of the forward propagating mode (the first two terms), the backward propagating mode (the third term) and the radiated field (the last term). It is, therefore, possible to determine the transmission and reflection coefficient, respectively,

$$T(\omega) \equiv \lim_{x\to\infty} \left| \frac{\mathbf{E}_{forw}(\mathbf{r},\omega)}{\mathbf{E}_0(\mathbf{r},\omega)} \right|^2 \tag{4.40}$$

and

$$R(\omega) \equiv \lim_{x\to-\infty} \left| \frac{\mathbf{E}_{back}(\mathbf{r},\omega)}{\mathbf{E}_0(\mathbf{r},\omega)} \right|^2, \tag{4.41}$$

where, we consider the field at two limits, $x \to \pm\infty$ to obtain the reflectivity and transmittivity of the scattering region, because at $\pm\infty$ only guided modes (even if backscattered) exist.

The transmitted part is

$$\begin{aligned} T(\omega) &= \lim_{x\to+\infty} \left| \frac{\mathbf{E}_{forw}(\mathbf{r},\omega)}{\mathbf{E}_0(\mathbf{r},\omega)} \right|^2 \\ &= \lim_{x\to+\infty} \left| 1 + \frac{\sum_{n=1}^{N(\omega)} \imath \frac{L\omega}{2v_{g,n}} \mathbf{E}_{k_n}(\mathbf{r}) \int_D A_n^+(\mathbf{r}',\omega)\Theta(x-x')d\mathbf{r}'}{\mathbf{E}_0(\mathbf{r})} \right|^2 \\ &= 1 + \sum_{n=1}^{N(\omega)} \sum_{p=1}^{N(\omega)} \frac{L^2\omega^2}{4v_{g,n}v_{g,p}} \frac{\mathbf{E}_{k_n}(\mathbf{r})\mathbf{E}_{k_p}^*(\mathbf{r})}{|\mathbf{E}_0(\mathbf{r})|^2} \\ &\quad \int_D \int_D \Delta\varepsilon(\mathbf{r}')\Delta\varepsilon^*(\mathbf{r}'') \left[\mathbf{E}_{k_n}^*(\mathbf{r}')\cdot\mathbf{E}_0(\mathbf{r}')\right] \left[\mathbf{E}_{k_p}(\mathbf{r}'')\cdot\mathbf{E}_0^*(\mathbf{r}'')\right] d\mathbf{r}'d\mathbf{r}'' \\ &\quad + \sum_{n=1}^{N(\omega)} \frac{L\omega}{v_{g,n}} \Re\left\{ \frac{\imath\mathbf{E}_{k_n}(\mathbf{r}) \int_D A_n^+(\mathbf{r}',\omega)d\mathbf{r}'}{\mathbf{E}_0(\mathbf{r})} \right\}. \end{aligned} \tag{4.42}$$

4.2.4 The backscatter losses

The backscatter loss is the fraction of light intensity that is backscattered due to imperfections captured by $\Delta\varepsilon$ and it is simply the reflection coefficient $R(\omega)$. We have:

$$\begin{aligned} \alpha_{back} \equiv & R(\omega) = \lim_{x\to-\infty} \left| \frac{\mathbf{E}_{back}(\mathbf{r},\omega)}{\mathbf{E}_0(\mathbf{r},\omega)} \right|^2 \\ &= \lim_{x\to-\infty} \left| \frac{\sum_{n=1}^{N(\omega)} \imath \frac{L\omega}{2v_{g,n}} \mathbf{E}_{k_n}^*(\mathbf{r}) \int_D A_n^-(\mathbf{r}',\omega)\Theta(x'-x)d\mathbf{r}'}{\mathbf{E}_0(\mathbf{r})} \right|^2 \\ &= \sum_{n=1}^{N(\omega)} \sum_{p=1}^{N(\omega)} \frac{L^2\omega^2}{4v_{g,n}v_{g,p}} \frac{\mathbf{E}_{k_p}(\mathbf{r})\mathbf{E}_{k_n}^*(\mathbf{r})}{|\mathbf{E}_0(\mathbf{r})|^2} \int_D \int_D A_n^-(\mathbf{r}') \left(A_p^-(\mathbf{r}'')\right)^* d\mathbf{r}'d\mathbf{r}'' \\ &= \sum_{n=1}^{N(\omega)} \sum_{p=1}^{N(\omega)} \frac{L^2\omega^2}{4v_{g,n}v_{g,p}} \frac{\mathbf{E}_{k_p}(\mathbf{r})\mathbf{E}_{k_n}^*(\mathbf{r})}{|\mathbf{E}_0(\mathbf{r})|^2} \\ &\quad \int_D \int_D \Delta\varepsilon(\mathbf{r}')\Delta\varepsilon^*(\mathbf{r}'') \left[\mathbf{E}_{k_n}(\mathbf{r}')\cdot\mathbf{E}_0(\mathbf{r}')\right] \left[\mathbf{E}_{k_p}^*(\mathbf{r}'')\cdot\mathbf{E}_0^*(\mathbf{r}'')\right] d\mathbf{r}'d\mathbf{r}'', \end{aligned} \tag{4.43}$$

where we did the approximation $A_n^-(\mathbf{r},\omega) = \Delta\varepsilon(\mathbf{r}')\mathbf{E}_{k_n}(\mathbf{r}')\cdot\mathbf{E}_0(\mathbf{r}',\omega)$, because we have only kept terms that are consistent with the truncation of the Born expansion in Eq. 4.10 at the second order.

There are several ways in writing this relation, but we choose the representation with correlation, because it permits to introduce correlation consideration about the disorder as we will see in sec. 4.2.7.

We define the intermodal losses between two modes with wavevectors k_n and k_p as:

$$\begin{aligned}\alpha_{k_n,k_p}(\omega) = \frac{L^2\omega^2}{4v_{g,n}v_{g,p}}\Bigg[&\frac{\mathbf{E}_{k_p}(\mathbf{r})\mathbf{E}^*_{k_n}(\mathbf{r})}{|\mathbf{E}_0(\mathbf{r})|^2}\int_D\int_D \Delta\varepsilon(\mathbf{r}')\Delta\varepsilon^*(\mathbf{r}'')\\ &[\mathbf{E}_{k_n}(\mathbf{r}')\cdot\mathbf{E}_0(\mathbf{r}')]\left[\mathbf{E}^*_{k_p}(\mathbf{r}'')\cdot\mathbf{E}^*_0(\mathbf{r}'')\right]d\mathbf{r}'d\mathbf{r}''\\ &+\frac{\mathbf{E}_{k_n}(\mathbf{r})\mathbf{E}^*_{k_p}(\mathbf{r})}{|\mathbf{E}_0(\mathbf{r})|^2}\int_D\int_D \Delta\varepsilon(\mathbf{r}')\Delta\varepsilon^*(\mathbf{r}'')\\ &\left[\mathbf{E}_{k_p}(\mathbf{r}')\cdot\mathbf{E}_0(\mathbf{r}')\right]\left[\mathbf{E}^*_{k_n}(\mathbf{r}'')\cdot\mathbf{E}^*_0(\mathbf{r}'')\right]d\mathbf{r}'d\mathbf{r}''\Bigg]\\ = \frac{L^2\omega^2}{4v_{g,n}v_{g,p}}\cdot 2\Re\Bigg\{&\frac{\mathbf{E}_{k_p}(\mathbf{r})\mathbf{E}^*_{k_n}(\mathbf{r})}{|\mathbf{E}_0(\mathbf{r})|^2}\int_D\int_D \Delta\varepsilon(\mathbf{r}')\Delta\varepsilon^*(\mathbf{r}'')\\ &[\mathbf{E}_{k_n}(\mathbf{r}')\cdot\mathbf{E}_0(\mathbf{r}')]\left[\mathbf{E}^*_{k_p}(\mathbf{r}'')\cdot\mathbf{E}^*_0(\mathbf{r}'')\right]d\mathbf{r}'d\mathbf{r}''\Bigg\},\end{aligned} \tag{4.44}$$

while in the particular case $k_n = k_p$, we have:

$$\begin{aligned}\alpha_{k_n}(\omega) = \frac{L^2\omega^2}{4v_{g,n}^2}\Bigg[&\frac{|\mathbf{E}_{k_n}(\mathbf{r})|^2}{|\mathbf{E}_0(\mathbf{r})|^2}\int_D\int_D \Delta\varepsilon(\mathbf{r}')\Delta\varepsilon^*(\mathbf{r}'')\\ &[\mathbf{E}_{k_n}(\mathbf{r}')\cdot\mathbf{E}_0(\mathbf{r}')]\left[\mathbf{E}^*_{k_n}(\mathbf{r}'')\cdot\mathbf{E}^*_0(\mathbf{r}'')\right]d\mathbf{r}'d\mathbf{r}''\Bigg]\\ = \frac{L^2\omega^2}{4v_{g,n}^2}\cdot\Re\Bigg\{&\frac{|\mathbf{E}_{k_n}(\mathbf{r})|^2}{|\mathbf{E}_0(\mathbf{r})|^2}\int_D\int_D \Delta\varepsilon(\mathbf{r}')\Delta\varepsilon^*(\mathbf{r}'')\\ &[\mathbf{E}_{k_n}(\mathbf{r}')\cdot\mathbf{E}_0(\mathbf{r}')]\left[\mathbf{E}^*_{k_n}(\mathbf{r}'')\cdot\mathbf{E}^*_0(\mathbf{r}'')\right]d\mathbf{r}'d\mathbf{r}''\Bigg\}.\end{aligned} \tag{4.45}$$

Using the latter definitions, we can recast Eq. 4.43 as:

$$\alpha_{back}(\omega) = R(\omega) = \sum_{n=1}^{N(\omega)}\left[\alpha_{k_n}(\omega) + \sum_{p=n+1}^{N(\omega)}\alpha_{k_n,k_p}(\omega)\right]. \tag{4.46}$$

4.2.5 The radiation losses

The radiation losses are the losses due to the fraction of light radiated out by the waveguide:

$$L_{rad}(\omega) = 1 - T(\omega) - R(\omega), \tag{4.47}$$

and by using Eq. 4.42 and 4.43, we have:

$$\begin{aligned}\alpha_{rad} \equiv L_{rad} = & -\sum_{n=1}^{N(\omega)}\sum_{p=1}^{N(\omega)} \frac{L^2\omega^2}{v_{g,n}v_{g,p}\left|\mathbf{E}_0(\mathbf{r})\right|^2} \\ & \int_D\int_D \Delta\varepsilon(\mathbf{r}')\Delta\varepsilon^*(\mathbf{r}'') \left[\Re\left\{\mathbf{E}_{k_n}(\mathbf{r})\mathbf{E}^*_{k_n}(\mathbf{r}')\right\}\cdot\mathbf{E}_0(\mathbf{r}')\right] \\ & \qquad \left[\Re\left\{\mathbf{E}_{k_p}(\mathbf{r})\mathbf{E}^*_{k_p}(\mathbf{r}'')\right\}\cdot\mathbf{E}^*_0(\mathbf{r}'')\right] d\mathbf{r}'d\mathbf{r}'' \\ & -\sum_{n=1}^{N(\omega)} \frac{L\omega}{v_{g,n}} \Re\left\{\frac{\imath\mathbf{E}_{k_n}(\mathbf{r})\int_D A_n^+(\mathbf{r}',\omega)d\mathbf{r}'}{\mathbf{E}_0(\mathbf{r})}\right\}.\end{aligned} \tag{4.48}$$

4.2.6 The single-mode case

In this section, we consider that the waveguide at frequency ω_0 is single-mode, that is the equation $\omega(k) = \omega_0$ has only one solution, k_0.

In this case, the homogeneous solution (cfr. 4.25) for the electric field is

$$\mathbf{E}_0(\mathbf{r}) = \sqrt{\frac{a}{L}}\mathrm{e}^{\imath k_0 x}\mathbf{e}_{k_0}(\mathbf{r}),$$

while the associated Green dyadic is

$$\begin{aligned}\overleftrightarrow{G}_{prop}(\mathbf{r},\mathbf{r}'_0) = \imath\frac{a\omega_0}{2v_g}\Big[&\mathbf{e}_{k_0}(\mathbf{r})\otimes\mathbf{e}^*_{k_0}(\mathbf{r}')\mathrm{e}^{\imath k_0(x-x')}\Theta(x-x') \\ &+\mathbf{e}^*_{k_0}(\mathbf{r})\otimes\mathbf{e}_{k_0}(\mathbf{r}')\mathrm{e}^{\imath k_0(x'-x)}\Theta(x'-x)\Big],\end{aligned} \tag{4.49}$$

where $v_g \equiv \frac{d\omega}{dk}\big|_{k=k_0}$.

Using the last two equations, Eq. 4.38 becomes

$$\begin{aligned}\mathbf{E}(\mathbf{r}) = & \mathbf{E}_0(\mathbf{r}) \\ & + \mathbf{E}_0(\mathbf{r})\int_D \Delta\varepsilon(\mathbf{r}')A(\mathbf{r}')\Theta(x-x')d\mathbf{r}' \\ & + \mathbf{E}^*_0(\mathbf{r})\int_D \Delta\varepsilon(\mathbf{r}')B(\mathbf{r}')\Theta(x'-x)d\mathbf{r}' \\ & + \int_D \Delta\varepsilon(\mathbf{r}')\overleftrightarrow{G}_{rad}(\mathbf{r},\mathbf{r}')\cdot\mathbf{C}(\mathbf{r}')d\mathbf{r}'\end{aligned} \tag{4.50}$$

where the explicit form of A, B and $\mathbf{C}$ are respectively:

$$\begin{aligned}
A(\mathbf{r}) = & \imath\frac{a\omega}{2v_g}|\mathbf{e}_k(\mathbf{r})|^2 \\
& - \frac{a^2\omega^2}{4v_g^2}|\mathbf{e}_k(\mathbf{r})|^2\int_D \Delta\varepsilon(\mathbf{r}')|\mathbf{e}_{-k}(\mathbf{r}')|^2\Theta(x-x')d\mathbf{r}' \\
& - \frac{a^2\omega^2}{4v_g^2}\mathrm{e}^{-2\imath kx}\left[\mathbf{e}_k^*(\mathbf{r})\cdot\mathbf{e}_k^*(\mathbf{r})\right] \\
& \qquad \int_D \Delta\varepsilon(\mathbf{r}')\mathrm{e}^{\imath 2kx'}\left[\mathbf{e}_k(\mathbf{r}')\cdot\mathbf{e}_k(\mathbf{r}')\right]\Theta(x'-x)d\mathbf{r}' \\
& + \imath\frac{a\omega}{2v_g}\mathrm{e}^{-\imath kx}\mathbf{e}_k^*(\mathbf{r})\int_D \Delta\varepsilon(\mathbf{r}')\mathrm{e}^{\imath kx'}\overleftrightarrow{G}_{rad}(\mathbf{r},\mathbf{r}')\cdot\mathbf{e}_k(\mathbf{r})d\mathbf{r}' \\
B(\mathbf{r}) = & \imath\frac{a\omega}{2v_g}\mathrm{e}^{2\imath kx}\left[\mathbf{e}_k(\mathbf{r})\cdot\mathbf{e}_k(\mathbf{r})\right] \\
& - \frac{a^2\omega^2}{4v_g^2}\mathrm{e}^{2\imath kx}\left[\mathbf{e}_k(\mathbf{r})\cdot\mathbf{e}_k(\mathbf{r})\right]\int_D \Delta\varepsilon(\mathbf{r}')|\mathbf{e}_k^*(\mathbf{r}')|^2\Theta(x-x')d\mathbf{r}' \\
& - \frac{a^2\omega^2}{4v_g^2}|\mathbf{e}_k(\mathbf{r})|^2\int_D \Delta\varepsilon(\mathbf{r}')\mathrm{e}^{\imath 2kx'}\left[\mathbf{e}_k(\mathbf{r}')\cdot\mathbf{e}_k(\mathbf{r}')\right]\Theta(x'-x)d\mathbf{r}' \\
& + \imath\frac{a\omega}{2v_g}\mathrm{e}^{\imath kx}\mathbf{e}_k(\mathbf{r})\int_D \Delta\varepsilon(\mathbf{r}')\mathrm{e}^{\imath kx'}\overleftrightarrow{G}_{rad}(\mathbf{r},\mathbf{r}')\cdot\mathbf{e}_k(\mathbf{r})d\mathbf{r}' \\
\mathbf{C}(\mathbf{r}) = & \mathbf{E}_0(\mathbf{r}) \\
& + \imath\frac{a\omega}{2v_g}\sqrt{\frac{a}{L}}\mathrm{e}^{\imath kx}\mathbf{e}_k(\mathbf{r})\int_D \Delta\varepsilon(\mathbf{r}')|\mathbf{e}_k^*(\mathbf{r}')|^2\Theta(x-x')d\mathbf{r}' \\
& + \imath\frac{a\omega}{2v_g}\sqrt{\frac{a}{L}}\mathrm{e}^{\imath kx}\mathbf{e}_k(\mathbf{r})\int_D \Delta\varepsilon(\mathbf{r}')\mathrm{e}^{\imath 2kx'}\left[\mathbf{e}_k(\mathbf{r}')\cdot\mathbf{e}_k(\mathbf{r}')\right]\Theta(x'-x)d\mathbf{r}' \\
& + \sqrt{\frac{a}{L}}\int_D \Delta\varepsilon(\mathbf{r}')\overleftrightarrow{G}_{rad}(\mathbf{r},\mathbf{r}')\cdot\mathbf{E}_0(\mathbf{r}')d\mathbf{r}'.
\end{aligned} \tag{4.51, 4.52, 4.53}$$

We can now obtain the approximation of the reflection coefficient (cfr. Eq. 4.43) as:

$$\begin{aligned}
R(\omega) \equiv & \lim_{x\to-\infty}\left|\frac{\mathbf{E}_{back}(\mathbf{r})}{\mathbf{E}_0(\mathbf{r})}\right|^2 \\
= & \frac{L^2\omega^2}{4v_g^2}\int_D\int_D B(\mathbf{r}')\left(B(\mathbf{r}'')\right)^* d\mathbf{r}'d\mathbf{r}'' \\
= & \frac{a^2\omega^2}{4v_g^2}\int_D\int_D \Delta\varepsilon(\mathbf{r}')\Delta\varepsilon^*(\mathbf{r}'') \\
& \qquad \left[\mathbf{e}_{k_0}(\mathbf{r}')\cdot\mathbf{e}_{k_0}(\mathbf{r}')\right]\left[\mathbf{e}_{k_0}^*(\mathbf{r}'')\cdot\mathbf{e}_{k_0}^*(\mathbf{r}'')\right]\mathrm{e}^{2\imath k_0(x'-x'')}d\mathbf{r}'d\mathbf{r}'',
\end{aligned} \tag{4.54}$$

4.2.7 The disorder correlation

The several works, that have been done to study impact of imperfections on the performance of a PhC, established quite generally that small randomness in PhC geometry and/or material constants lead to an overall reduction in a band gap size, as well as an increased back-scattering and radiation losses, while stronger randomness can lead to appearance of localized impurity states. Usually the disorder parameters introduced above are scanned from small to large and conclusions are drawn about their relative impacts. But propagation parameters can be sensitive functions of disorder parameters. Thus, for a rigorous comparison of theoretical estimates with experimental observations one has to be precise about the types and statistical importance of realistic imperfections. Skorobogatiy and Bégin in [45] tried to understand which are the statistical parameters of importance when describing disorder in PC lattices, and then to characterize such parameters quantitatively by analyzing high resolution experimental images of 2D planar slab PCs. They found that three intuitive sets of parameters are necessary to create a comprehensive statistical model of PC imperfections. First set of parameters describe coarse properties of features such as radius, ellipticity and other low angular momenta components in a feature shape. Such coarse variations of a shape can be either deliberately designed or result from an imperfect manufacturing process. Another set of parameters describe roughness of feature edges on a nanometer scale, that is wall roughness, which is ultimately determined by the random physical processes of electron scattering in a resist, resist development and etching. A final set of parameters describes deviations of feature centers from ideal periodic lattice.

We want to try to model the disorder function $\Delta\varepsilon(\mathbf{r})$ in a quite simple way, by taking in account the imperfections introduced during the fabrication process. The dominant imperfection is surface roughness appearing on the sidewalls of the holes. It is due to random fabrication variations in the mask, that after etching translates to vertical striations appearing on the sidewalls of the holes. It is reasonable to assume perfect correlation in the vertical direction, so we need only address in-plane variations. This is not completely true, because above all in SOI structure there is a not perfect verticalness of the holes due to the etching process of the holes.

We consider a semiconductor membrane with a number of etched holes (α) with radius r with centers located at the points $\mathbf{C}_i = (\rho_i, \phi_i)$ in polar coordinates [44]. The vertical coordinate is z and the membrane height is h. An exact expression for $\Delta\varepsilon(\mathbf{r})$ can be written in function of the roughness function ΔL, defined as the

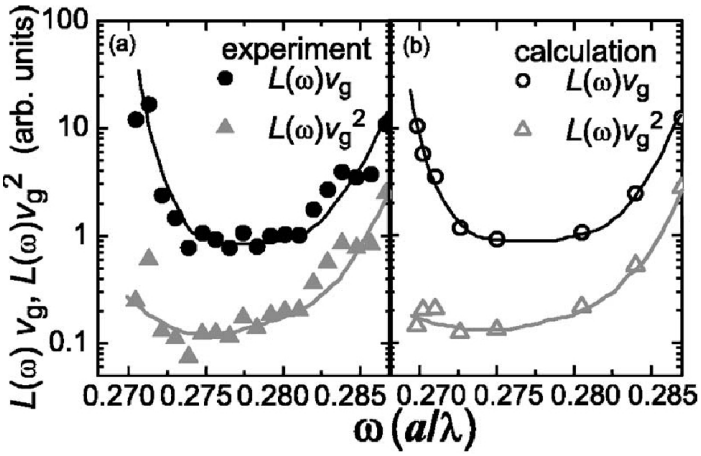

Figure 4.3: Confrontation between (a) measured and (b) calculated losses for a W1 waveguide. Image from [46]

distance between the true and the ideal structures:

$$\Delta L = \Delta L(\tilde{\phi}(\mathbf{C}, \mathbf{C}_i)), \tag{4.55}$$

with

$$\tilde{\phi}(\mathbf{C}, \mathbf{C}_i) = \arctan(\frac{\rho \sin\phi - \rho_i \sin\phi_i}{\rho \cos\phi - \rho_i \cos\phi_i}). \tag{4.56}$$

If we suppose that $\Delta L << r$, we can write

$$\Delta\varepsilon(\mathbf{r}) = (\varepsilon_2 - \varepsilon_1)\Theta(h/2 - |z|) \sum_{i}^{N_{holes}} \Delta L(\tilde{\phi}(\mathbf{C}, \mathbf{C}_i))\delta(r - |\rho - \rho_i|), \tag{4.57}$$

where $\varepsilon_1(\varepsilon_2)$ is the dielectric constant in the etched layer outside (inside) the air holes.

Because the disorder function appears in each loss equation inside a double integral and assuming inter-hole disorder uncorrelated, we can consider the multiple-scattering correlation function [47] of the ΔL function

$$< \Delta L(\tilde{\phi})\Delta L(\tilde{\phi}') >= \sigma^2 \mathrm{e}^{-r\frac{\|\tilde{\phi}-\tilde{\phi}'\|}{l_p}} \delta_{\alpha\alpha'}, \tag{4.58}$$

where $\tilde{\phi}' = \tilde{\phi}(\mathbf{C}', \mathbf{C}_i')$, l_p is the in-plane correlation length, and σ is the RMS roughness length.

The model just introduced is quite simple, but it allows a basic evaluation of the impact of disorder on propagation properties, as demonstrated in [46]. The authors, in fact, use this model to evaluate the proportionality of backscattering losses to the

inverse of the square of the group velocity. In Fig. 4.3, it was plotted the product of the measured losses and calculated v_g and v_g^2 for a W1 waveguide, while in Fig. 4.3b, there is the same plot but with calculated losses. The left side of the picture demonstrates the $(1/v_g)^2$ scaling for the losses, confirming that when v_g becomes small, the backward scattering becomes important and indeed dominant. The right side with the calculated data show a similar behavior, proving the validity of the used model.

Chapter 5

Time-Wavelength Reflectance Maps of PhCWGs

In the last chapter, we investigate the effects of disorder on the propagation of light in PhCWGs. Several techniques have been proposed for measuring the critical parameters of PhC waveguides, such as time resolved near field imaging (SNOM) [32], phase-shift [48], time-of-flight [49], time-domain transmission measurement [50] and Fabry-Perot fringe analysis [51]. Each of these methods has its own advantages and its own drawbacks, for instance, it is not straightforward to have a simple experimental setup, able to measure very dispersive structures, in a short time, with minimal sensitivity to parasitic light. Recently, the optical low-coherence reflectometry (OLCR) technique was applied to the investigation of PhC structures, demonstrating its effectiveness to provide an accurate and reliable measurement of the group delay, a good estimation of propagation losses and evidence of inter-mode coupling induced by disorder [52].

In this chapter, we will discuss about phase-sensitive optical low-coherence reflectometry, that, combined with a suitable digital processing of the OLCR signal, shows a considerable amount of information about disorder and permits to draw a complete dispersion map, i.e., to divide the components of the reflected signal corresponding to different wavelengths, but superposed in time [53].

We apply this technique to four 1 mm long PhC waveguides with suitable engineered dispersion curves, that operate in a regime of semi-slow light (see Sec. 3.3.2), a trade-off between group velocity and propagation losses [33], because it is more robust with respect to the strong losses induced by disorder.

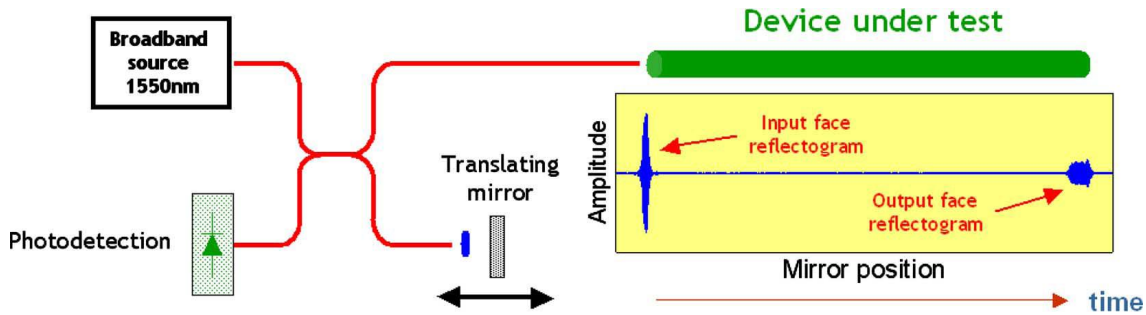

Figure 5.1: Simplified scheme illustrating the principle of the OLCR measurement. It is a fibered Michelson interferometer with the device under test in one arm. The interference signal versus the delay is measured with high spatial accuracy.

All the material presented in this chapter has been developed at Advanced Photonics Lab of Thales Research and Technology, Paris, under the guidance of dr. Alfredo de Rossi, and has been published in [53].

5.1 Optical Low Coherence Reflectometry

OLCR is a nondestructive technique allowing the measurement of the backreflected signal as a function of the position inside a passive or active photonic device. It provides a very good spatial resolution and a large dynamical range [54]. It has been shown [55], [56] that this technique can be used to extract all characteristic parameters relevant to complex structures such as Bragg gratings and ring resonators coupled to waveguides (i.e., coupling coefficients, propagation losses, and optical cavity length L).

The OLCR setup is basically a Michelson interferometer illuminated with a broadband source (e.g., a 1520-1610 nm Er^{3+} superfluorescent source), which spectrum is $S(\omega)$; the device under test in one arm, and a translating mirror in the other one (see Fig. 5.1). The main idea is that the backreflected signal coming back from the sample after a delay t interferes with the signal coming back from the other arm at the same time, within an interval Δt, because of its limited temporal coherence. Thus, the amplitude of the interference fringes is proportional to the signal backreflected within a spatial region inside the sample, which depends on the position of the other arm. When examining a waveguide or a photonic device entailing an input and an output facet, the measured signal shows typically the first reflection at the device input facet and then the signatures of multiple round trips inside the device

(Fig. 5.1). Moreover, a background originated by backscattering in the waveguide is also detected. Ideally, the spatial resolution is related to the spectral width of the source through a simple Fourier transform. Actually, this technique measures a time, which is the propagation delay through the sample; consequently, the link between the spectral band of the source and the accuracy in the measurement of the delay appears formally as an uncertainty principle between time and frequency. OLCR is demonstrated as a suitable technique for the measurement of propagation and dispersion inside waveguides and, in particular, for slow light.

5.1.1 Phase-Sensitive OLCR

A standard OLCR equipment only measures the amplitude of the interference fringes. However, valuable information is contained in the complete interferogram. Indeed, the interferogram $I(t)$ is connected to the complex reflectivity $r(\omega)$ by the inverse Fourier transform:

$$I(t) = \int_{-\infty}^{+\infty} S(\omega) r(\omega) \mathrm{e}^{-\imath\omega t} d\omega. \tag{5.1}$$

This suggests that the complex reflectivity can be retrieved by Fourier transform and normalization with respect to the source spectrum $S(\omega)$. However, a specific experimental setup is required, with spatial accuracy in the submicrometer scale, in order to resolve the interference fringes. This kind of setup has been developed at TELECOM ParisTech, and the complete description can be found in [57]. Once the complex reflectivity is obtained, it is straightforward to extract the group delay from the phase. This allows a complete characterization of a waveguide in term of complex index, group delay, group velocity dispersion and birefringence. This technique was initially proposed to characterize fiber Bragg gratings [58], micro-structured fibers, or few-modes fibers [59].

5.2 PhC Waveguides

In this work we will focus on single mode PhC waveguides made on thin membranes of gallium arsenide (GaAs). The scanning electron microscopy (SEM) of the sample in Fig. 5.2 shows the typical structure which is fabricated by patterning a silica hard mask through Electron-beam lithography, followed by reactive ion etching (RIE) and final transfer into the semiconductor by high-density plasma etching [51].

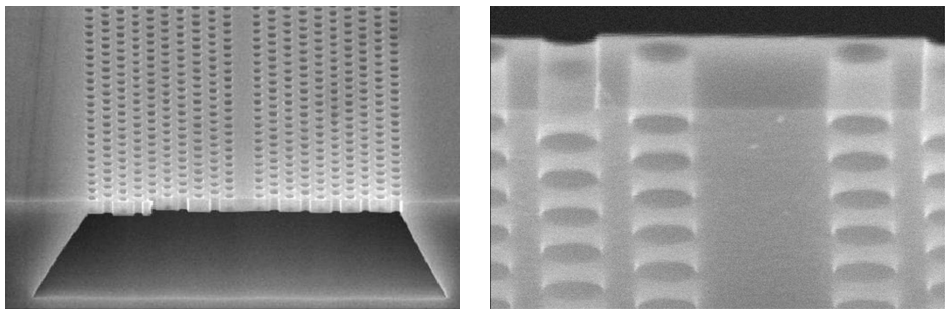

(a) (b)

Figure 5.2: (a) SEM image of a typical PhC membrane waveguide on GaAs. (b) Detail of the sample.

The air-clad membrane of GaAs was obtained by removing an underlying sacrificial layer by wet etching. We have obtained a very high fabrication quality (Fig. 5.2b) which allowed us to achieve a record Q factor of 700000 in III-V PhC cavities [60], [61].

The four PhC waveguides used in our study are 1 mm long with the thickness of the membrane is 265 nm.

1. **Sample 1** has a lattice period $a = 418$ nm, the hole radius is $r = 0.26a$. The waveguide consists of a single missing row of holes along the direction; the normalized width is $W = 1.057\sqrt{3}a$. This value is used to optimize coupling to PhC cavities. The corresponding band diagram, shown in Fig. 5.3, is calculated using a 3D Finite Differences in Time Domain code with periodic boundary conditions, in order to implement the Bloch's theorem. This code permits to calculate accurately the leaky modes outside the light cone (dashed) as well as the bound modes (solid). Two bands of TE modes appear within the measurement spectral window. The TE even band reveals the typical behavior of single line defect PhC waveguides [62]; the group velocity is almost constant at high frequency and then decreases and vanishes at the band edge, which is located at 1630 nm. The odd TE band has two minima, one is in the leaky region. The dispersion of a TM mode is very close to an index-guided waveguide, except for a small bandgap between 1537 nm and 1527 nm. The group index of the TM mode is approximately constant and close to $n_g = 5$, which is quite a high value [63]. This is not surprising, however, and it is not peculiar of photonic crystal. Rather, this is typical of tightly confined TM

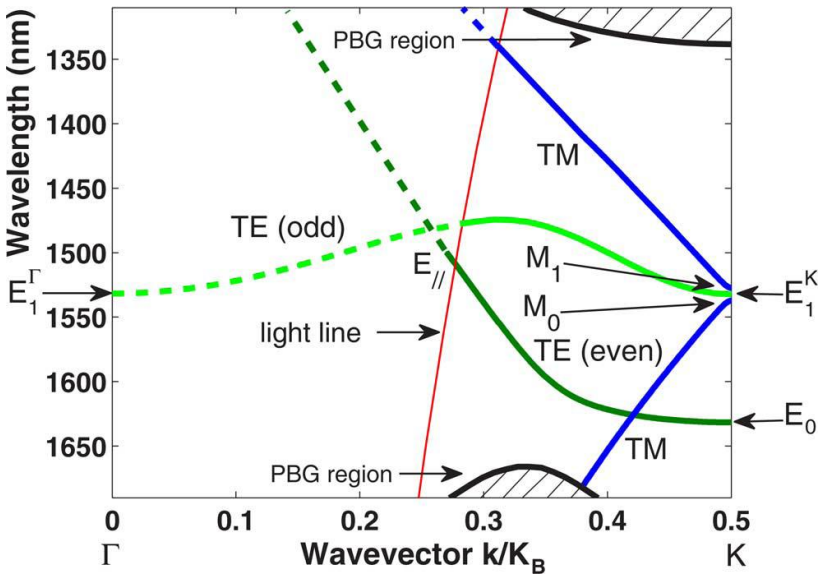

Figure 5.3: Calculated dispersion for the PhC waveguide (sample 1) revealing a TE even mode with band edge at 1630 nm (E_0), a TE odd mode with band edges at the points $k = k_B/2$ (E_1^K)and $k = 0$ (E_1^Γ) which coincide at 1533 nm; the TM band with a minigap in 1537 nm (M_0) and 1527 nm (M_1). The light line (red line) marks the transition to leaky modes ($E_{//}$ at 1510 nm for TE even).

modes in very thin slabs, as it can easily be proven by effective index analysis.

2. **Sample 2** is very similar to sample 1, except that the lattice period is $a =$ 400 nm, the hole radius is $r = 0.242a$. In addition, sample 2 entails the well known optimized L3 microcavity with loaded $Q \approx 10000$ (intrinsic $Q \approx 40,000$) and resonant frequency at 1555 nm, which is side-coupled to the waveguide. The normalized width of $W = 1.057\sqrt{3}a$ was chosen in order to optimize the coupling with the cavity.

3. **Samples 3** is characterized by a non uniform size of the holes along the transverse axis of the waveguide [33].

4. **Sample 4** is identical to sample 3, except for three localized defects. This defects were deliberately inserted to test the effectiveness of OLCR.

5.2.1 Group Delay in PhC Waveguides

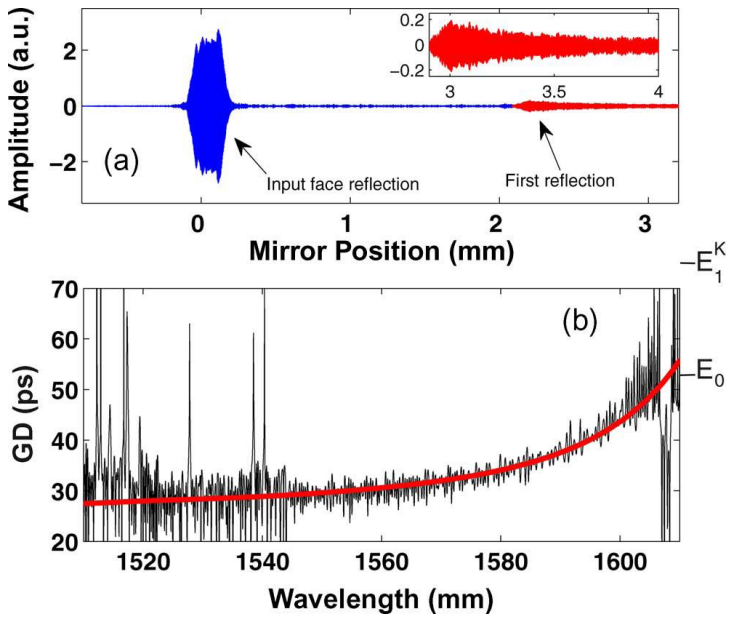

Figure 5.4: (a) Measurement of the phase-sensitive OLCR signal from sample 1, TE even polarization. (b) From this signal, the group delay is extracted. The solid thick line represents the calculated delay.

Fig. 5.4a shows the reflectogram for sample 1 in the TE polarization. We can see the reflection peaks corresponding to the input facet and to the first reflection on the rear facet of the waveguide. The reflection on the rear facet appears to be strongly broadened, compared to the reflection at the input facet, due to the large dispersion value of the PhC waveguide. Fig. 5.4b, instead, compares the Group Delay (GD) obtained through a Fourier analysis on the second peak of the reflectogram with the value calculated from the simulated dispersion diagram (see Fig. 5.3). We analyze the TE even case which better reveals the specific properties of PhC waveguides [52] and we find a very good agreement between the two curves.

The transmission band of the PhC waveguide under test extends from the onset of optical leakage, setting the high frequency limit (here 1520 nm), to the low-frequency cutoff (1630 nm). As expected, the round-trip group delay increases first slowly when moving to longer wavelengths and then increases very fast ($\Delta\tau \approx 30$ ps) when approaching the cutoff, thus entering in the slow-light region (1600-1610 nm). The results are consistent with phase-shift measurements made on similar samples, which also reported similar group delay evolutions [48].

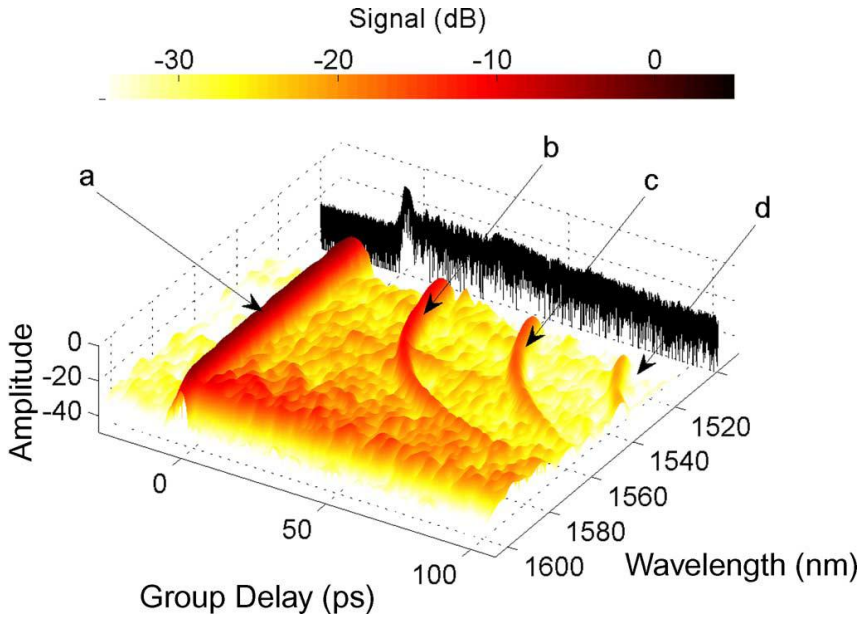

Figure 5.5: 3-D time-wavelength reflectance map of sample 2 extracted numerically from the phase-sensitive reflectogram which is also shown (black plot). Clearly visible are (a) the reflectance peaks from the input facet and (b)-(d) after multiple round trips in the waveguide.

5.3 Time-Wavelength Reflectance Maps

In an OLCR reflectogram of a highly dispersive waveguide the contributions from the whole spectra are superimposed (i.e., overlapping between the different successive reflections on the rear facet). This is a major limitation when investigating strongly dispersive structures such as photonic crystals. The obvious way to achieve a spectral separation between fast and slow modes is to cascade an optical tunable narrow bandpass filter after the OLCR source [56]. In the absence of dispersive effects the spatial resolution is determined by the coherence of the source. Therefore, considering the broadband source parameters (source bandwidth $\Delta\lambda = 80$ nm and central wavelength $\lambda_0 = 1565$ nm), the expected resolution is about 10 µm, corresponding to 33 fs in time domain. However, a difference in fiber length between the two arms of the interferometer and/or the optical filtering of the source induces a residual dispersion that deteriorates the theoretical spatial resolution. Hence, practical resolution is about 0.36 ps without filtering and 1.1 ps with a 2 nm filtering.

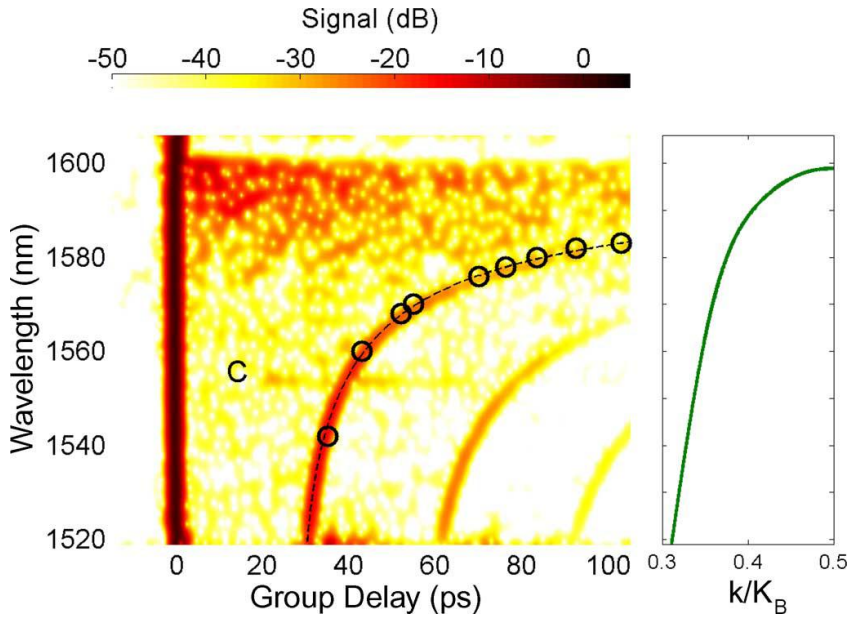

Figure 5.6: The time-wavelength map as in Fig. 5.5 is represented as a 2D plot. The reflectivity peaks obtained with the optical filtering, represented by circles, and the calculated group delay (dotted curve) are superimposed. The signature of the side-coupled cavity at $\lambda = 1555$ nm is denoted by the letter C. The left panel shows the calculated dispersion (λ versus wave vector) for the corresponding TE even mode.

5.3.1 Interferogram Digital Processing

To overcome reflection overlapping in reflectograms, the best way to extract GD properties is to apply a digital processing to the OLCR measurements. The numerical algorithm that exploits the phase-sensitive reflectograms has been introduced in [64]. The phase-sensitive reflectogram similar to that shown in Fig. 5.4a is Fourier transformed and we then apply a sliding numerical filtering (Gaussian-shape filter) to the spectrum in order to treat in the spectral domain each wavelength separately. The filter bandwidth (typically 2 nm) is chosen as a trade-off between the coherence length of the filtered source and the medium dispersion to optimize the spatial resolution. The procedure is repeated by sweeping the filter center frequency such that a wavelength dependent reflectogram is obtained.

Fig. 5.5 represents as a 3-D graph the time-wavelength map extracted from the corresponding reflectogram, also shown on the backside. The intensity of the reflected signal is reported as a function of the arrival time (after a round trip), and of the wavelength. Each maximum in the signal amplitude corresponds to a

strong reflection, either on a facet or on defects inside the waveguide. We see four maxima associated to the input facet, the rear facet, and two more round trips in the waveguide. This figure provides a clear understanding of the impact of losses and dispersion on the shape of the reflectogram; that is the broadening and the decrease of the reflectance peak after one or more round trips. The procedure is validated by comparing the outcome with the results obtained by direct optical filtering of the OLCR source. The GD values obtained for different values of selected frequency are shown in Fig. 5.6. The two methods give self-consistent results concerning the dispersion properties of the PhCs. Besides, the spectral signature (at 1550 nm) of the resonance of an optimized L3 type side-coupled microcavity is revealed (the horizontal vanishing line).

The quality of the measurement and the efficiency of the numerical treatment in preserving the information is remarkable. The measurement with the numerical treatment is easier (only coupling of the fiber into the waveguide input facet is required) to implement with respect to time-resolved techniques [32], that can be considered complementary, or SNOM techniques. In addition, it is very fast (a few seconds).

5.3.2 Reflectance Maps versus High Resolution Transmission

It is enlightening to compare the time-wavelength map in Fig. 5.6 with the high-resolution transmission spectra measured on sample 2 using a narrow linewidth (1 pm) laser tunable in the range 1500 to 1600 nm. This is shown in Fig. 5.7. The transmission band of the cavity extends between 1520 nm and the waveguide cutoff, which is beyond 1600 nm. The transmission band is characterized by regular and well contrasted Fabry-Pérot fringes appearing from the light line limit to about 1575 nm. This corresponds to the almost ideal transmission of a single mode waveguide with end faced reflectivity equal to about 30%, which agrees well with the calculated value [48]. Beyond this limit, the fringes become less regular and the contrast increases. This is also the spectral region where the group velocity of the even TE mode decreases while approaching the cutoff. The resonance of the side-coupled cavity appears as a deep dip (the cavity is overcoupled: $Q/Q_i \approx \sqrt{T_{\min}/T_{\max}} \approx 0.2$). The lineshape is not Lorentzian due to inteference with waveguide Fabry-Pérot resonance.

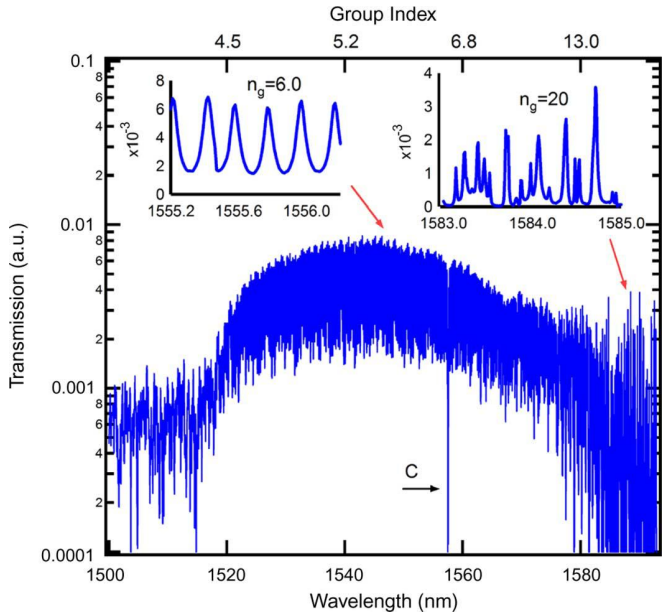

Figure 5.7: High-resolution transmission spectra of sample 2 (TE polarization, log scale). The calculated value for the edge of the TE odd band (E_1) is at 1520 nm and corresponds to the strong decrease of transmission. Also visible is the signature of the side-coupled cavity at 1555 nm (mark C), with $Q \approx 10000$. Insets: enlarged view showing regular Fabry-Pérot fringes (left) and isolated peaks near the band edge (linear scale).

5.4 Disorder induced scattering

Imperfections, roughness and discontinuities break the translational symmetry in optical waveguides and result into backscattering (coupling to the backward propagating wave) or scattering to other waveguide modes. This also induces some depolarization, as TE and TM modes may be mixed by imperfections. The general picture holds for PhC structures, however, their much richer band structure, entailing strongly varying group velocity and minigaps (e.g., Fig. 5.3), has a strong impact on the scattering losses. A theory specific to PhC waveguides has been developed in Sec. 4.2 [44], which agrees very well with experiments on silicon PhC waveguides [46]. Various mechanisms associated to disorder-induced scattering have been revealed: backscattering, intermodal scattering and a peculiar channel of propagation losses in which energy is scattered into a slow and leaky mode in the odd TE band. Now, by using the reflectance maps, we want to confirm these observations and get a deeper physical insight.

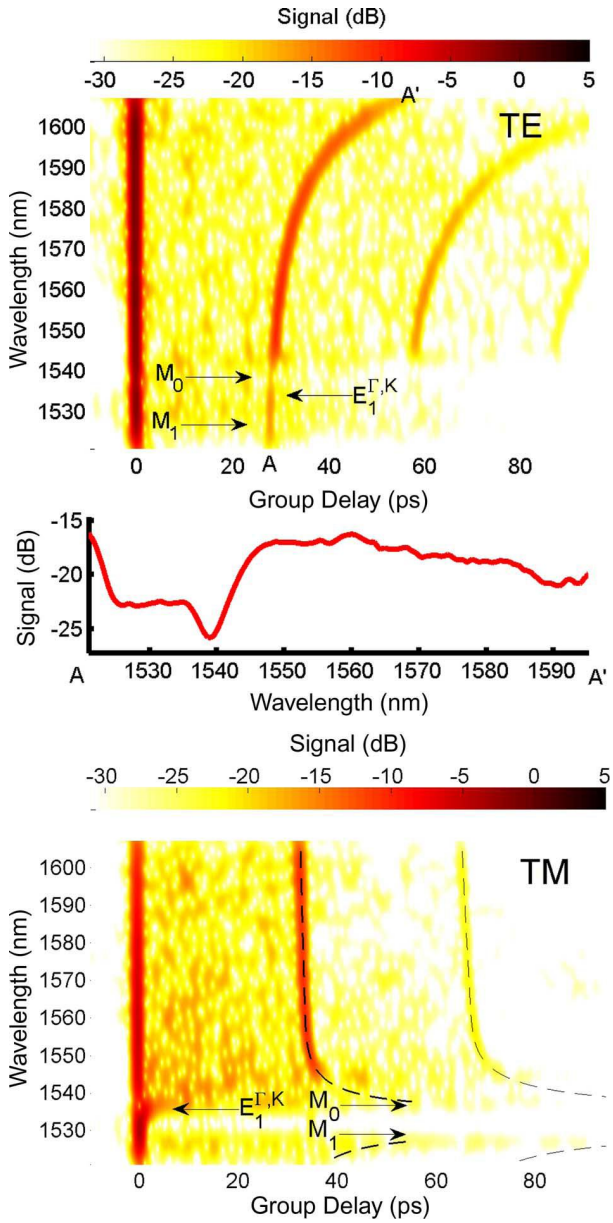

Figure 5.8: Time-wavelength reflectance maps for the sample 1, with dispersion calculated in Fig. 5.3, for TE (top) and TM (bottom) polarizations. The plot in the middle is extracted from the TE map following the trace of the first round trip. The calculated group dispersion for the TM mode is superimposed (dotted). The arrows denote the TM minigap (M_0 and M_1) and the band edges of the odd TE mode (E_1^K, E_1^Γ).

5.4.1 Propagation of Slow Modes

The theory developed for PhCs reveals that backscattering has an explicit dependence on the inverse group velocity squared, therefore may become very strong even if fabrication imperfections are minimal. A first evidence of the impact of the disorder on slow modes is given by the high-resolution measurement shown in Fig. 5.7. The regular Fabry-Pérot fringes appearing from 1520 nm to about 1575 nm evidence almost ideal propagation, so that scattering is negligible. The picture changes sharply at longer wavelengths: the fringes become irregular and then change into isolated peaks with no-ordered structure. The transmission is high at resonance (only one half of its maximum value, Fig. 5.7). These peaks are likely to correspond to extended resonant states generated by coherent backscattering which are reminiscent of what was observed in disordered opals [65]. Long group delays are associated to resonances, instead, short group delays result from antiresonances. The OLCR spectral map in Fig. 5.6 provides a complementary view of the phenomena. While in the spectral region from 1520 nm up to 1575 nm the signature of the mode is well defined and follows the calculated dispersion perfectly, at larger wavelengths the signal is dispersed and comes at any time from zero to large values. This can be understood knowing that the OLCR spectral map cannot resolve the alternation of resonances and antiresonances, as the filter was set to 2 nm. Those two independent measurements show that disorder induces a drastic change in the propagation of the slow modes. The OLCR map reveals that slow modes do not follow their theoretical dispersion but, as the group index increases, the reflection peak vanishes while the backscattering appears. Within this propagation regime, which is dominated by disorder, the energy does not escape from the mode, as the waveguide transmission remains high, but the propagation time varies very fast with wavelength and may be very large.

5.4.2 Intermodal Scattering and Propagation Losses

Disorder induces a transfer of energy from a mode to another with the explicit dependence on the inverse of the product of the respective group velocities 4.2. It follows that a high-order mode with slow group velocity may have a strong impact on the fundamental mode. This was observed experimentally in Si waveguides for the first time in [46], but only by using the time-wavelength reflectance maps, it is possible to obtain a very clear signature of the phenomenon. Let us consider sample

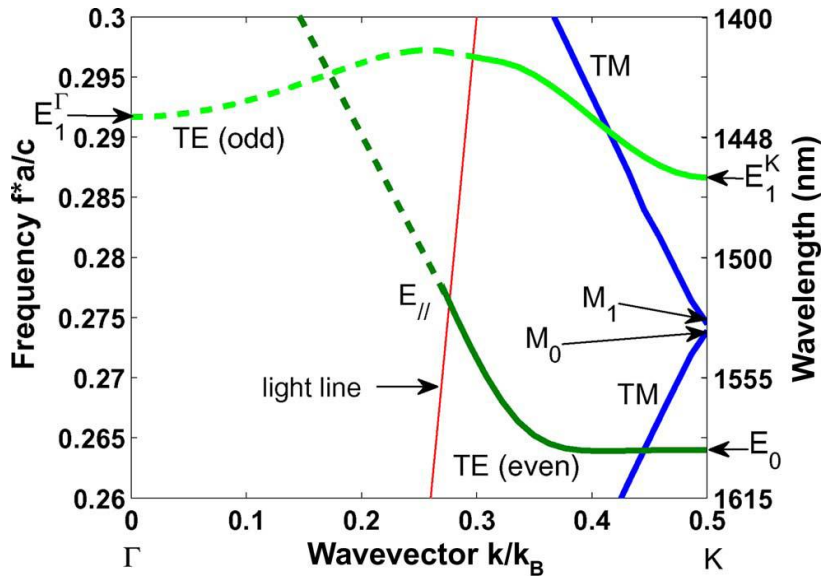

Figure 5.9: Calculated dispersion for the sample 3. The two TE bands have edges at 1590 nm (E_0), 1460 nm (E_1^K) and 1440 nm (E_1^Γ). The TM band has a minigap in 1530 nm (M_0) and 1535 nm (M_1). The red line also shown is the light line.

1 (Fig. 5.8) and focus on the TE polarization first. In addition to a clean trace of the dispersion of the fundamental mode and to some backscattering originated in a non-uniform manner along the waveguide, the map reveals the weakening of the reflected signal from 1540 nm, where it is particularly pronounced, towards lower wavelengths. This is even more evident in the second round trip. The amplitude of the OLCR signal taken along a path following the dispersion of the mode (Fig. 5.8) provides further insight. In contrast with Fig. 5.6, there is no evidence of backscattering enhancement in this spectral range which would explain the transmission loss. Therefore, the overall reflectivity signal (integrated over the time) is strongly decreased and this corresponds to a strong decrease of waveguide transmission.

The map relative to the TM polarization reveals the mini-gap, as predicted by the FDTD modeling (see Fig. 5.3). The minigap is located between 1537 and 1527 nm. In this range, the reflection at the input facet (delay is equal to zero) is increased and no signal appears at positive delays, as expected.

Understanding the results in Fig. 5.8 requires the examination of the calculated band diagram in Fig. 5.3. First of all, the onset of optical leakage of the fundamental mode is expected at 1510 nm, therefore too far away to explain the result. The odd TE band has two minima, one (E_1^K) is at the edge of the Brillouin zone (point K)

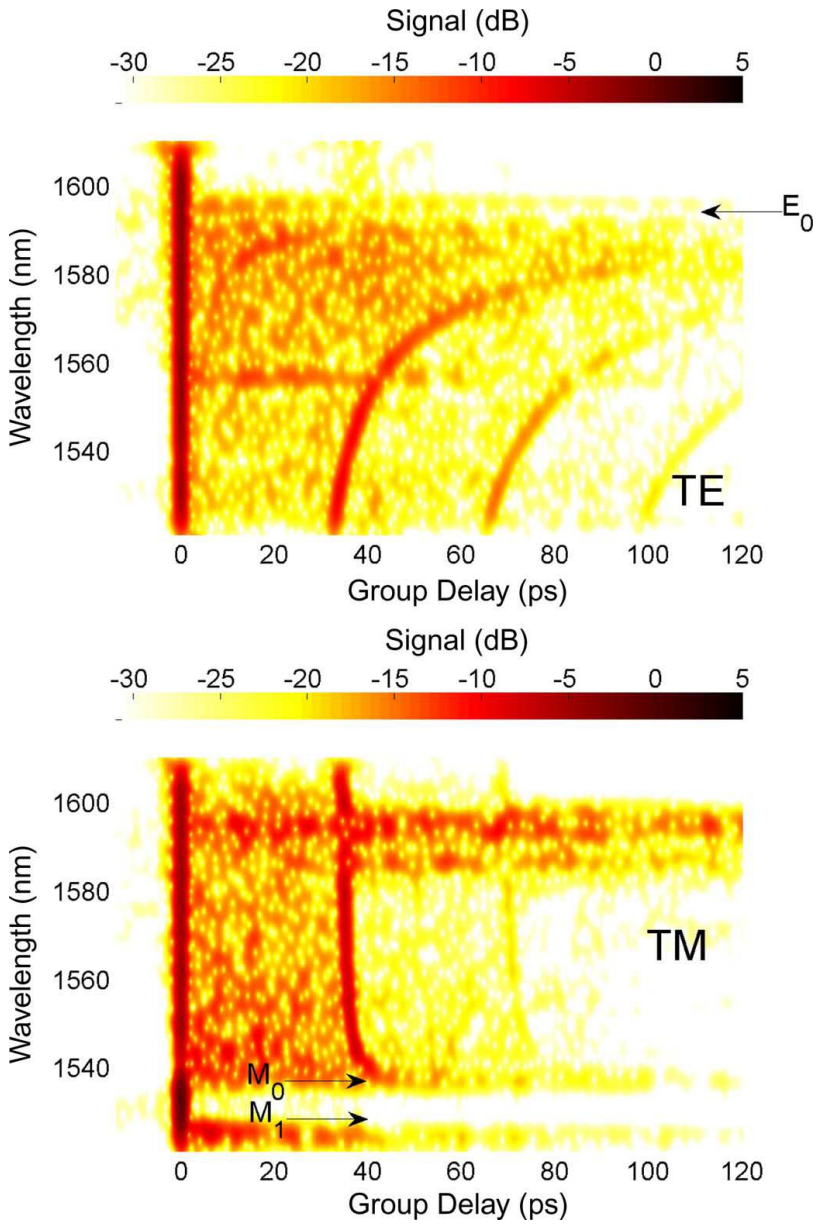

Figure 5.10: Time-wavelength reflectance maps measured for sample 3, for TE (top) and TM (bottom) polarizations. Corresponding dispersion is in Fig. 5.9. The arrows denote the band edge of the even TE mode (E_0). Note that the edge of the even mode is at higher frequency than in the case reported in Fig. 5.8.

and the other is at the center (point Γ). These two minima are very close (1533 nm). The spectral match between the TM minigap and the losses in TE mode would suggest a possible impact of slow TM modes, therefore some polarization scattering. However, polarization scattering requires that disorder breaks the symmetry of PhC membrane, which was not observed on silicon-based structures [66]. On the other hand, the effect could be attributed to the slow modes at the edge of the TE odd band, which are in the same spectral range. A clear answer to the question is possible by confronting this measurement with some measurements made on sample 3, which dispersion (see Fig. 5.9) shows the odd TE mode is far away from the TM minigap. In fact, the TE map (Fig. 5.10) shows no trace of the impact of disorder, which could be associated to the TM minigap. Therefore, we conclude that the slow modes at the edges of the TM minigap do not explain the dip in the transmission of the TE mode. More generally, propagation losses, as we see in this case, cannot be attributed to transfer of energy to another mode, as the reflectance map clearly shows that the energy escapes from the waveguide. We believe that the mechanism underlying these losses is off-plane scattering mediated by slow leaky modes in the odd TE band. This was proposed and observed in [46]. Scattering from the fundamental (even) TE mode to small-k modes near the Γ point light is peculiar, because these modes have a very short lifetime. The effect is enhanced near the band edge because the group velocity vanishes there, as predicted by the Green function theory. This picture is confirmed by the fact that, in the case of sample 3, the small-k band edge $E_1^{\Gamma} = 1440$ nm, which is outside the measurement range and therefore cannot be seen. Indeed, no transmission dip is seen in the measurements.

5.4.3 Scattering in Slow Modes

Fig. 5.10 also provides further insight on the slow modes of the TE even band and completes the picture given by Fig. 5.6, because the cutoff is well within the spectral band of the OLCR setup. First, the band edge is clearly identified, as for $\lambda > 1595$ nm the entire signal comes from the input facet. In other words, the light cannot penetrate in the photonic crystal as expected, as it should be for wavelength within the photonic bandgap. On the other hand, a relevant amount of signal is originated from backscattering all along the waveguide. As the group delay increases, the strength of the signal reflected by the end facet decreases and becomes even weaker than backscattering. Again, as it was for sample 1, backscattering is even stronger when moving closer to the band edge. When looking at the properties

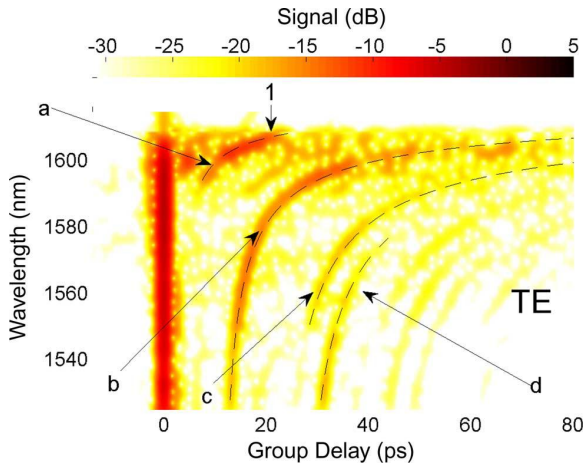

Figure 5.11: Time-wavelength reflectance maps for the sample 4. Curves (a), (b) and (c) denote reflectance peaks on defects inside the structure, while (c) corresponds to the reflection from the output facet of the waveguide.

of the TM transmission we notice that, first, the signature of the minigap is better defined than in Fig. 5.8 and it is apparent that the reflectance increases at the input facet accordingly (no propagation inside the waveguide). Second, a stripe of reflectance signal between 1585 nm to 1600 nm denotes that, again, light propagates in the waveguide in a disordered way and that the energy is dispersed over almost any delay. In particular, this is the signature of a transfer of energy towards modes with long lifetime. It is not possible to explain that based on the dispersion of the TM mode, which is almost flat in this region. On the other hand, this region coincides with the slow modes of the TE band. This suggests that TE-TM scattering is the underlying mechanism in this case.

5.4.4 Signature of Slow Modes

Fig. 5.11 shows the time-reflectance map for sample 4, that was designed with three well localized defects. In the reflectance map, the reflection peaks generated by three localized defects are well recognized; the first one a is situated at 0.1 mm after the input facet, the second one (b) at 0.4 mm after the input facet and the third one (c) at 0.85 mm. The peak corresponding to the reflection at the output facet is denoted by the letter (d). The dispersive behavior of scattering at the point defects is apparent. Defect (a) produces a strong scattering between 1595-1608 nm, defect (c) between 1550-1590 nm and takes over the reflection at the end facet (d).

The signatures of the defects are exploited in order to estimate the group index of slow modes which are too strongly backscattered before reaching the end facet. Let us look at the trace of the defect (b), follow it until the onset of the signature of defect (a) and then continue on this latter until point (1). In this way we deduce a group delay of 20 ps at 1607 nm, which translates into a group index of 60 (the length is 0.1 mm).

5.5 Conclusion

Phase-sensitive OLCR is a powerful tool to explore the properties of PhC waveguides, and to investigate dispersion and disorder induced scattering. The representation of the measurement as a time-wavelength map of the backreflected signal gives a tremendous physical insight for understanding the role of disorder induced scattering and how it is connected to dispersion. We found that scattering depends strongly on the group velocity, and in particular that backscattering tends to dominate as soon as the group velocity decreases (thus confirming theory).

Understanding the impact of disorder on the propagation of slow modes in PhC structures is crucial in view of realizing devices exploiting the full potential of dispersion engineering inherent to photonic crystals, and we think that this technique can give a large contribution.

Chapter 6

Heterodyne Detection for PhCWGs Characterization

The basic understanding of the dynamics into a 2D photonic crystal waveguide is fundamental before to evaluate the potential photonic devices.

The work presented in this chapter was developed during two period at the Technical University of Denmark, department of Photonics, DTU Fotonik, under the supervision of Prof. Mike van der Poel and Prof. Jesper Mørk. The aim was to realize a series of experiment, with the collaboration of Ph.D. fellow Per L. Hansen, to evaluate the delay effects of a 2D photonic crystal waveguide on a pulse in the range of femtoseconds, by using the heterodyne detection technique with femtosecond pulses. Unfortunately, it was not possible to get any useful result, so we will just present the heterodyne principles, describing the heterodyne pump-probe set-up, and the devices we used in the FemtoLab at DTU Fotonik.

6.1 The Heterodyne Measurement Technique

The word *heterodyne* is derived from the Greek roots *hetero-*, different, and *dyn-*, power. In radio and signal processing, heterodyning is the generation of new frequencies by mixing, or multiplying, two oscillating waveforms. It is useful for modulation and demodulation of signals, or placing information of interest into a useful frequency range. The two frequencies are mixed in a vacuum tube, transistor, diode, or other signal processing device. Mixing two frequencies creates two new frequencies, according to the properties of the sine function: one at the sum of the

two frequencies mixed, and the other at their difference. These new frequencies are called *heterodynes*. Typically only one of the new frequencies is desired, usually the higher one after modulation and the lower one after demodulation. The other signal is filtered out of the output of the mixer. The original heterodyne technique was pioneered by Canadian inventor-engineer Reginald Fessenden, but was not pursued very far because local oscillators were not very stable at the time. Frequency filters and the heterodyne detection in the radio makes it possible to closely space different radio channels in the frequency domain.

The essence of heterodyning is to measure the beating between two waves. This waves can be acoustic, in the range of Hertz, as for example the beating between a tuning fork and a not tuned music instrument, or it can be radio frequencies as mentioned before. In our case, heterodyning will be done on optical waves, where the carrier frequency is $f \simeq 193$THz. The detected heterodyne signal will be at 60kHz and easily detectable by standard equipment.

The advantages of using a heterodyne detection scheme are multiple when it is used to characterize waveguide components. The main one is the possibility to measure changes not only in the amplitude transmission of the waveguide, but also in the phase of the field after the propagation thought the component. The property to selectively filter the interested frequencies permits to distinguish optical fields with the same optical properties (polarization, wavelength, direction and position), by shifting the central frequency of the fields a few MHz from each other.

This powerful technique can be improved by using ultrashort optical pulses (in the range of fs), because it enables the measurement of time-resolved transmission and refractive index changes.

The idea of using a heterodyne detection technique together with a pump-probe set-up was first presented by the group of E. Ippen at MIT in the early 1990's [67]. The first results on gain and index dynamics in semiconductor optical amplifiers on a subpicosecond time scale were presented in 1991-92 [68][69], while in 1996 a similar setup was used to investigate four-wave mixing (FWM) at the Danish Telecom Research facility (TDR) [70]. The theory for femtosecond pulses was developed at the same time by A. Mecozzi and J. Mørk [71]. An improved detection scheme was built in 1998 at the Technical University of Denmark (DTU) by P. Borri and W. Langbein [72] to characterize FWM and gain dynamics in quantum dot waveguide amplifiers [73][74].

6.1.1 The source

From a theoretical point of view, the source must give a train of pulses with a certain repetition rate F, where each pulse is centered at the variable frequency ω_0 and has the desired pulse energy. Each pulse $E_0(t)$ should be considered a Gaussian pulse with an intensity width τ_p in the subpicosend range.

Supposing $E_0(t)$ centered at $t = t_0$, we have

$$E_0(t) = E_0 \exp\left(-\frac{(t-t_0)^2}{\tau_p^2} + \imath\omega_0 t\right). \tag{6.1}$$

In frequency domain the pulse will be represented as

$$\tilde{E}_0(\omega) = \frac{E_0\tau_p}{\sqrt{2}} \exp\left(-\frac{\tau_p^2}{4}(\omega-\omega_0)^2 + \imath\omega t_0\right). \tag{6.2}$$

The train of pulses can be described as

$$E(t) = \sum_{n=-\infty}^{\infty} E_0(t - t_0 + nT), \tag{6.3}$$

where $T = 1/F$ is the repetition rate and n is an integer.

To obtain all these features, a commercial laser system from Coherent Inc. is used. The system consists of 5 separate systems

- Coherent Verdi V-5 (5W of continuous wave power);
- Coherent Verdi V-10 (10W of continuous wave power);
- Coherent MIRA 900 (Titanium-Sapphire modelocked oscillator);
- Coherent RegA 9000 (Titanium-Sapphire regenerative amplifier);
- Coherent OPA (Optical parametric amplifier).

The full system is shown in Fig. 6.1. The Verdi V-5 provides 5 W of power to pump the Ti:Al_2O_3 (titanium:sapphire) crystal, which acts as the gain medium for the MIRA. The Ti:Al2O3 gain peak is at 800 nm. The slit and the two dispersive prisms P_1 and P_2 allow to obtain the modelocking of the cavity. The MIRA minimum pulse width is $\approx$ 150 fs with $\sim$ 1.3 W of output power. The repetition rate is 80 MHz.

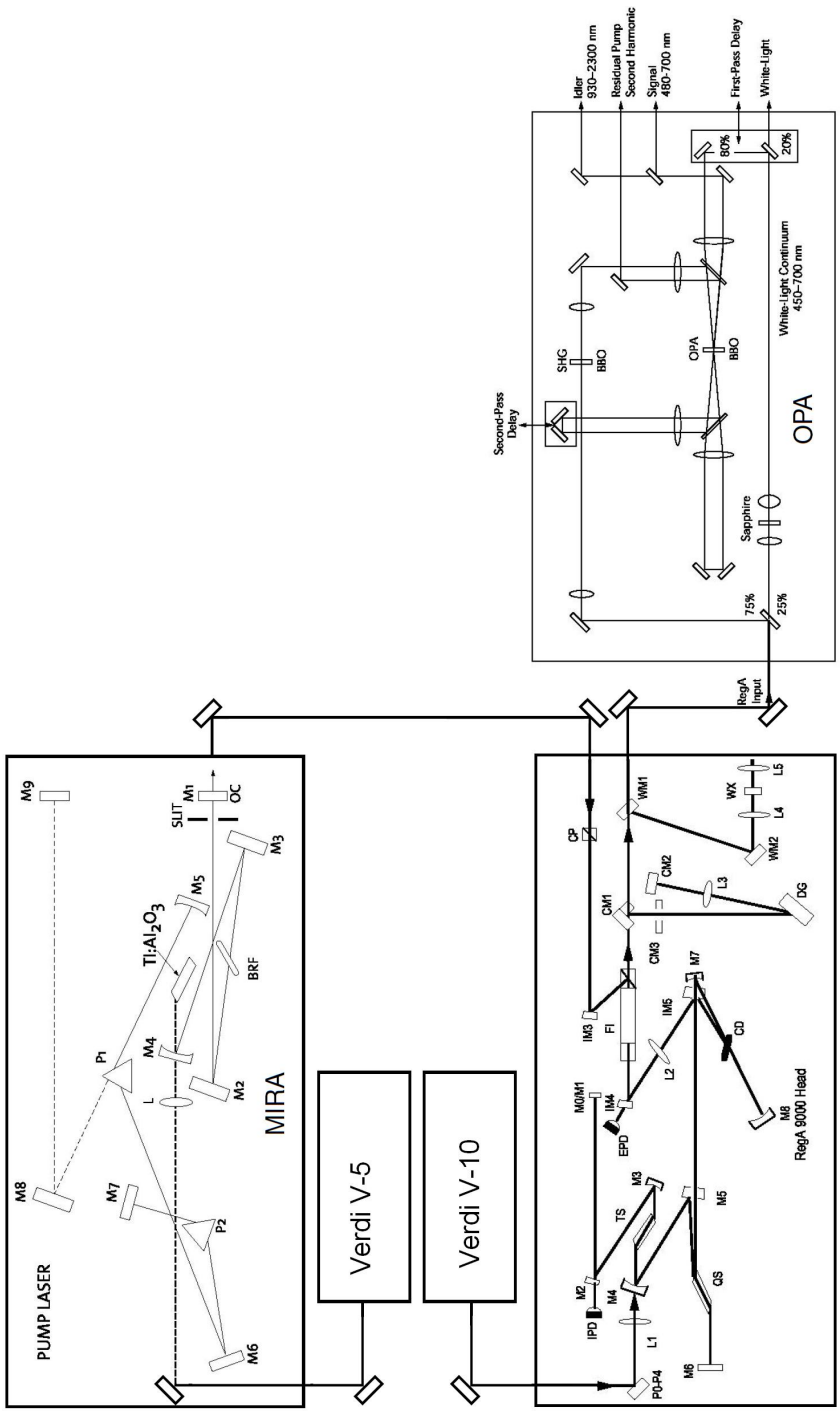

Figure 6.1: Illustration of the Coherent Inc. laser system. The Verdi V-5 and V-10 pump respectively the MIRA and the RegA. The output pulses from the MIRA are amplified in the RegA. The 800 nm output pulses of the RegA are shifted to the desired wavelength by optical parametric amplification in the OPA.

To obtain a variable wavelength of the pulse, coming from the Ti:Al_2O_3 based system, the nonlinear process of optical parametric amplification is used. This implies that the MIRA output pulse needs to be amplified.

For this regenerative process, it is used the Regenerative Amplifier (RegA). It is built around a Q-switched laser cavity. A Ti:Al_2O_3 crystal is pumped with 10 W of power from the Verdi V-10 and an intra cavity acousto-optic deflector (Q-switch) induces the externally controllable loss (QS in Fig. 6.1). When the acousto-optic cell is set to deflect, the inversion in the Ti:Al_2O_3 crystal increases (stimulated emission by the lasing mode of the cavity is prohibited). As the deflection in QS is turned off, a pulse from MIRA is simultaneously coupled into the cavity using an other acousto-optic cell, the cavity dumper (CD in Fig. 6.1). The pulse will now experience a maximum gain from the Ti:Al_2O_3 crystal. The pulse travels through the cavity until the gain is depleted and is then ejected using the cavity dumper again. Following the ejection of the pulse, the Q-switch is again turned on as to prohibit lasing in the RegA cavity. When the inversion has again accumulated, a new pulse from the MIRA can be injected. The time to restore the inversion sets the limit of the repetition rate of the RegA output, which becomes ∼147.5 kHz. This means, that only every 540th MIRA pulse is injected into the RegA and amplified. The average output power from the RegA is also 1.3 W (same as for the MIRA), but now with 540 times more energy in the pulses. The several roundtrips the pulse does in the cavity induce a broadening of the pulse that is compensated by a pulse-shaper before the exit of the RegA, with a resulting pulse intensity-FWHM τ_p of $\sim$ 150 fs.

The output of the RegA is injected into the optical parametric amplifier, the Coherent OPA. In the OPA, 25% of the pulse energy is split off to generate a white light continuum, by using the self-focusing effect into a sapphire crystal. The result is a very broad band spectrum from the ultra-violet to the infrared, around 800 nm. The 75% of the RegA output is used for second harmonic generation of a 400 nm pulse in a nonlinear crystal (SHG-BBO in Fig. 6.1).

Finally, the white light continuum is overlapped with the 400 nm pulse in a second nonlinear crystal (OPA-BBO in Fig. 6.1), where a 400 nm photon is split into a signal photon and an idler photon. The wavelength of the signal photon and the idler photon depends on the angle of the nonlinear crystal, which can be adjusted to get the wavelength of interest. The nonlinear crystal is passed two times to maximize the conversion.

For the following experiments, only the idler is used and adjusted for operation

in the region around 1550 nm.

6.1.2 The heterodyne pump-probe set-up

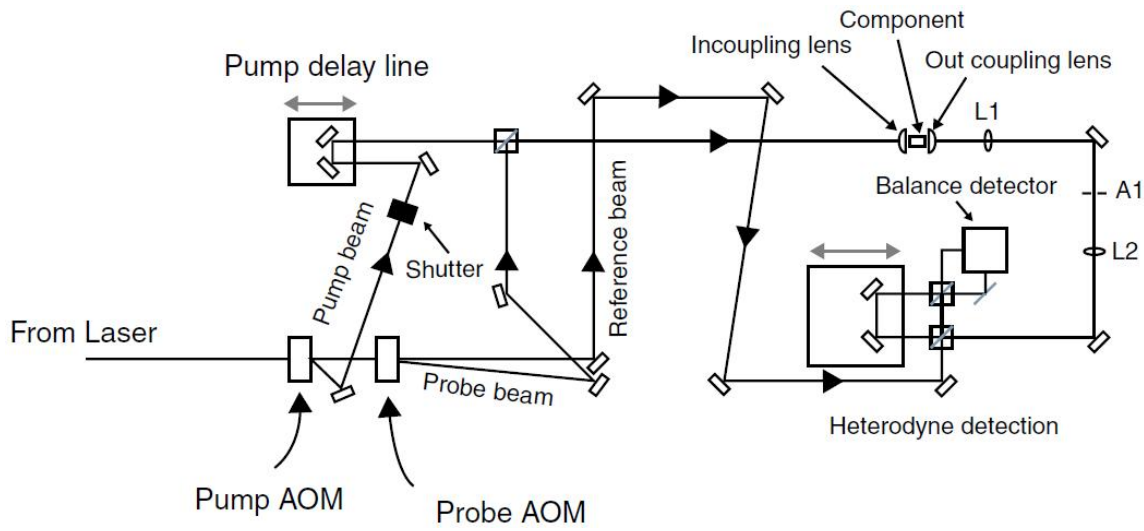

Figure 6.2: Illustration of the heterodyne pump-probe set-up.

Fig. 6.2 show a schematic illustration of the heterodyne pump-probe set-up.

The pulse that comes from the laser enters the pump AOM. An AOM consists of fused silica with a piezoelectric transducer on the one side of the crystal. A radio wave, generated by a driver, hits the silica and generates a traveling acoustic wave in the silica. This generates an index grating on which the optical wave is diffracted. Additionally, the optically diffracted field will be Doppler shifted by the radio-frequency at which the AOM is driven (40 MHz). The power of the diffracted beam, from here pump beam, is controlled by the power of the radio wave, which is controllable from the driver.

The pump beam goes through a shutter and a delay line with a 250 ps span, then is directed to the in-coupling microscope objective and, finally, is coupled into the component. The energy of the pump pulses at the microscope objective can be varied over 4 orders of magnitude, with a maximum energy of $\approx$ 250 pJ.

The part of the beam not deflected in the pump AOM enters the probe AOM. Here the probe beam is divided in the probe beam and the reference beam. The first one is the one deflected and frequency shifted by 39 MHz, 1 MHz less than the pump beam. It is overlapped with the pump beam in a 50/50 beam splitter, so

that with the pump beam goes into the microscope objective and then is coupled into the component. At that point, the pump and probe pulses can be distinguished only from 1 MHz MHz in frequency. After propagation through the component the pump-probe beam is collimated using the out coupling microscope lens. The lens L1 with the small aperture A1 are used to clean the output mode, while the lens L2 recollimates it.

The heterodyne set-up for passive waveguides

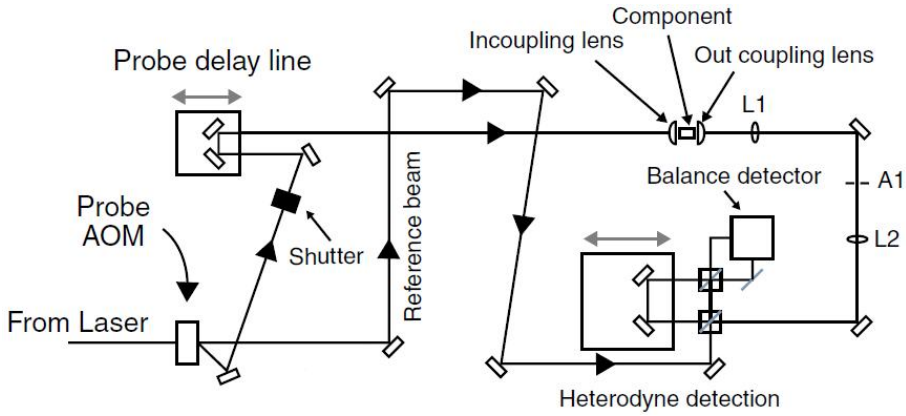

Figure 6.3: Illustration of the heterodyne set-up for passive waveguide.

In Fig. 6.3, it is shown a schematic illustration of the heterodyne set-up in case the experiment does not need any pump beam, as for instance the device under test is passive. The main difference is that the pump AOM is removed so that the only two beams that propagates are the reference and the probe ones. The probe AOM is set to introduce a frequency shift of 40 MHz, as for the pump AOM in the precedent scheme.

6.1.3 Detection

The heterodyne detection scheme is presented in Fig. 6.4. The center of the scheme is the 50/50 beam splitter; it has two functions: it permits to overlap spatially the pump and probe and the reference beam, already temporally overlapped through the reference delay line, and it divides the beam in two for the balanced detector, that measures the two quadratures from the beam splitter. The complete beam is composed with the overlap of the non-shifted reference pulse, the 40 MHz frequency shifted pump beam and the 39 MHz frequency shifted probe beam.

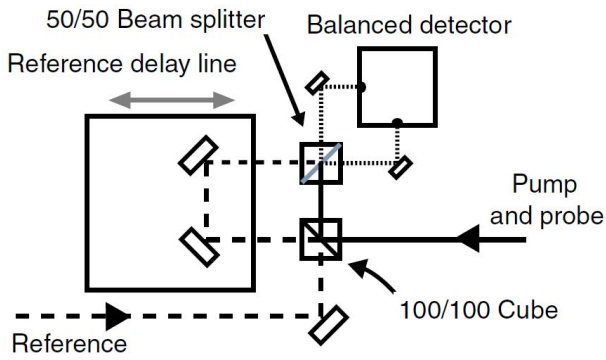

Figure 6.4: Zoom of the heterodyne detection scheme. The reference pulse can be delayed so that it overlaps the probe one. The probe and reference pulses are spatially overlapped in the 50/50 beam splitter and the two quadratures are detected in the balanced detector.

Writing the reference and pump (probe) fields in terms of their slowly varying envelope and phase component[75]

$$\begin{aligned} E_r(t) &= A_r(t)\exp(\imath(\omega_r t + \phi_r)) \\ E_p(t) &= A_p(t)\exp(\imath(\omega_p t + \phi_p)), \end{aligned} \tag{6.4}$$

the fields that arrive at the inputs A and B of the detector are:

$$\begin{aligned} E_A &= \frac{1}{\sqrt{2}}(A_r(t)\exp(\imath(\omega_r t + \phi_r)) + \imath A_p(t)\exp(\imath(\omega_p t + \phi_p))) \\ E_B &= \frac{1}{\sqrt{2}}(\imath A_r(t)\exp(\imath(\omega_r t + \phi_r)) + A_p(t)\exp(\imath(\omega_p t + \phi_p))) \end{aligned} \tag{6.5}$$

where we ignored any possible phase change expect from the $\pi/2$ shift from the reflection. The resulting intensity measured by the detector are

$$\begin{aligned} I_A &= \frac{c\varepsilon_0}{4}(A_p^2(t) + A_r^2(t) - 2A_p(t)A_r(t)\sin(\phi_p - \phi_r + (\omega_p - \omega_r)t)) \\ I_B &= \frac{c\varepsilon_0}{4}(A_p^2(t) + A_r^2(t) + 2A_p(t)A_r(t)\sin(\phi_p - \phi_r + (\omega_p - \omega_r)t)), \end{aligned} \tag{6.6}$$

where the last term in each intensity is the beat signal, between pump (probe) and reference.

The detector is balanced to reduce the common mode intensity noise fluctuations; its output is an electric current proportional to the difference of the two signals, that is proportional only to the beat signal

$$i(t) = \alpha(I_B - I_A) = \alpha\ c\varepsilon_0 A_p(t)A_r(t)\sin(\phi_p - \phi_r + (\omega_p - \omega_r)t), \tag{6.7}$$

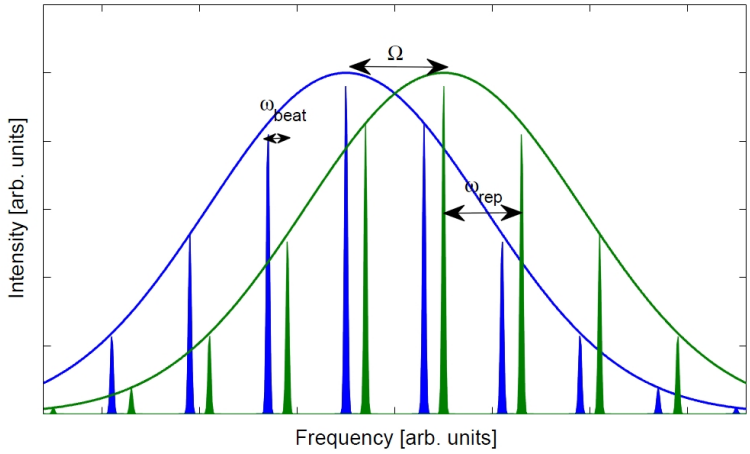

Figure 6.5: Illustration (not to scale) of the mixed reference and pump (probe) spectrum. Ω denotes the RF frequency driving the AOM, ω_{rep} is the repetition rate of the RegA, and ω_{beat} is the lowest beat frequency between the probe and reference spectrum, that is detected by the lock-in amplifier.

where α is a properly defined proportionality factor.

The spectrum of a laser pulse train consists of a series of sharp spectral lines separated by the repetition rate, f_{rep}, so there exists a infinite beat frequencies, as shown in Fig. 6.5. Approximating the spectral lines with delta functions, the spectra of the two fields are

$$\begin{aligned} E_r(\omega) &= \sum A_n \delta(\omega_0 - n\omega_{\text{rep}} - \omega), \qquad n \in \mathbb{Z} \\ E_p(\omega) &= \sum A_m \delta(\omega_0 + \Omega - m\omega_{\text{rep}} - \omega), \qquad m \in \mathbb{Z}, \end{aligned} \tag{6.8}$$

where Ω is the frequency driving the pump (probe) AOM, and $\omega_{\text{rep}} = 2\pi f_{\text{rep}}$.

The beat frequencies are then

$$\Delta\omega_{nm} = (m-n)\omega_{\text{rep}} - \Omega \equiv l\omega_{\text{rep}} - \Omega, \qquad l \in \mathbb{Z}. \tag{6.9}$$

The repetition rate of the train of pulses used in the experiment is 255 kHz , and the driving frequencies of the two AOMs for pump and probe are 39 MHz and 40 MHz , respectively. In the case of the setup for passive devices, only the probe is used and a driving frequency of the AOM of 40 MHz. In this case, the lowest beating frequency between the two fields is 35 MHz for $l = 157$, while the next lowest is 190 kHz.

The current of the balanced detector is sent to a lock-in amplifier with a detectable range from 0 to 100 kHz , so only the first one is detected. The lock-in amplifier

is referenced by down-mixing the sinusoidal RF frequency driving the AOM with a square wave signal of the repetition rate of the train of pulses. Since the square wave signal contains all higher harmonics of the repeon rate, the mixed frequencies corresponds exactly to those in Eq. 6.9.

An important point of this technique is that the output signal current shows changes of the electrical field of the pump (probe), and not of the intensity, and this implies that is detectable all the information contained in amplitude and phase of the output current.

6.2 The Device

Figure 6.6: Asymmetric Mach Zehnder Interferometer (aMZI), composed by two arms, with the longest one containing a 10 µm long slow light PhCWG (surrounded in red and expanded in Fig. 6.7). The physical difference of length of the two arms introduces a delay τ_d between the pulses that propagates through the device of $\sim$ 300 fs.

The aim of the experiment was to measure the delay induced by a 2DPhC on a femtosecond pulse, that is to obtain information about the group index and the slow or semi-slow light effect into a 2DPhC. To measure a delay, it is fundamental to have a reference pulse to compare with the delayed pulse. For this reason, an integrated asymmetric Mach Zehnder Interferometer was chosen as device under test. The asymmetric Mach Zehnder Interferometer, shown in Fig. 6.6, is composed by two arms: the first one is a simple silicon waveguide, while the second one is longer of the first one and contains a photonic crystal waveguide.

For this experiment, a chip with several interferometers was designed and fabricated in Silicon, with Silicon on Insulator technology (SOI) at DTU Fotonik. The

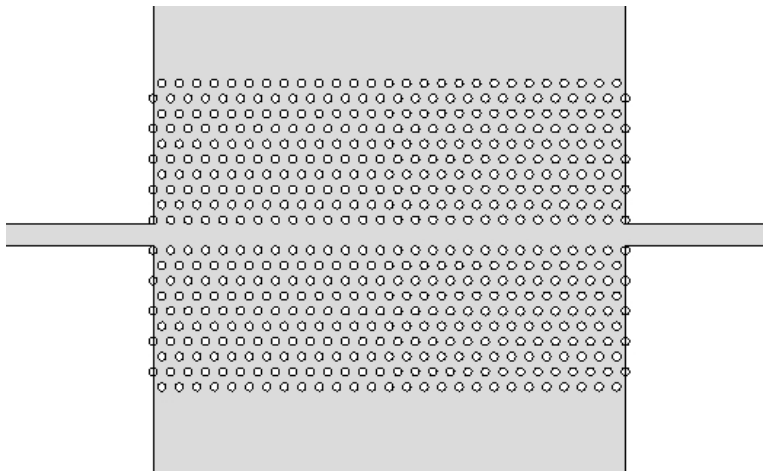

Figure 6.7: Example of photonic crystal waveguide included in the device of Fig. 6.6.

chip contains two families of PhCWG, to investigate slow light and semi-slow light phenomena, respectively. For each of these families, nine interferometers were realized, with three different lattice constants a (370 nm, 380 nm, and 390 nm) and three different lengths L (10 µm, 50 µm and 100 µm) of the waveguide.

The basic idea is quite simple. The pulse coupled into the device is split by an integrated 50/50 beam splitter in a reference beam, that propagates in the simple straight waveguide, and in a probe beam, that propagates in the arm with the photonic crystal waveguide. The PhCWG slows down the pulse introducing a delay related to the wavelength of the pulse according the dispersion relation that describes the behavior of the waveguide. After the propagation through the PhCWG the pulse is overlapped spatially with the one coming from the simple arm by another integrated beam splitter. The choice to use an asymmetric Mach Zehnder Interferometer, with the arms with a difference of length equivalent to a delay τ_d of ~ 300 fs, permits to recognize the two pulses at the detector, even when the PhCWG operates as a simple waveguide, that is the wavelength of the pulse is not in the bandgap of the photonic crystal.

Chapter 7

Conclusions

This thesis has concerned the propagation of light in semiconductor photonic crystal waveguide structures with emphasis on propagation properties and disorder effects. We have introduced the theory of photonic crystals, of which main peculiarity is the dispersion relation that introduces a set of permitted and forbidden bands for light propagation (Chapter 1). Then, we have focused on two-dimension photonic crystal, analyzing the difference between a membrane structure and a structure on a low-index cladding (Chapter 2). By introducing a linear defect in a photonic crystal, we have seen that it is possible to obtain a waveguide with the same band diagram of the original crystal, but few states (modes) in forbidden bands, that permit to guide light (Chapter 3). These modes have a dispersion relation not merely linear or parabolic, so it is recommended to take into account higher order dispersion. So, we have focused on third order dispersion, by evaluating its effect on a pulse propagating in the waveguide. By analyzing band for which group index is higher (sometime much higher) than the usual refractive index (i.e. the velocity of light is significantly smaller than expected), we have introduced the concept of Slow Light phenomena. Finally, by considering the third order susceptibility, we have theoretically investigated the Four-Wave Mixing phenomenon in this waveguide. All these phenomena are always influenced by the presence of the extrinsic disorder, due to fabrication process, so we have developed a basic model to evaluate the effect of disorder on the backscattering losses and out-of-plane losses (Chapter 4).

Several techniques have been studied and implemented to characterize experimentally photonic crystal waveguides. In this work, we have introduced the Time-Wavelenght Reflectance Map and the Heterodyne Pump-Probe Technique. The first

one (Chapter 5) has been developed with Thales Research and Technology (Paris, France), and allows to evaluate the propagation properties of the waveguide as function of the wavelength showing a deep physical insight for understanding the role of disorder induced scattering and how it is connected to dispersion. The second one (Chapter 6) has been tested at DTU Fotonik (Copenhagen, Denmark) and detects changes in amplitude and phase of an electromagnetic pulse propagated through a photonic crystal waveguide allowing, theoretically, to evaluate group delay, distortions and non-linear effects in Fast and Slow Light regime.

In the following, the results on each of the above topics are briefly summarized.

Four Wave Mixing Equations We have considered cubic non-linearity due to third order susceptibility and we have developed the Four-wave mixing equations for a photonic crystal waveguide. In this model, we have considered also the Self Phase Modulation and the Cross Phase Modulation. Differently from the fibers [42], these terms are essential for a right evaluation of the phase change of the mixing waves. To obtain the model, we have considered the dielectric function as space-dependent, so we have replaced the effective area of the classical equations, meaningless in a photonic crystal, with the effective volume, that we have found to be dependent from group velocity and field shape of the different waves. The result represents a theoretical limit of the amplification factor that is possible to obtain in a photonic crystal waveguide.

Disorder effects We have developed a model based on Green function theory to evaluate the impact of imperfections on the performance of a PhC. We already know that small randomness in PhC geometry and/or material constants lead to an overall reduction in a band gap size, as well as an increased back-scattering and radiation losses, while stronger randomness can lead to appearance of localized impurity states. With our model, we have found that back-scattering losses are proportional to the inverse of the square of the group velocity. This means that when v_g is small, the backward scattering becomes important and indeed dominant, as confirmed by Time-Wavelength Reflectance Map.

Time-Wavelenght Reflectance Map Phase-sensitive OLCR is a powerful tool to explore the properties of PhC waveguides, and to investigate dispersion and disorder induced scattering. We have experimentally confirmed that scattering depends

strongly on the group velocity, and in particular that backscattering tends to dominate as soon as the group velocity decreases.

7.1 Outlook

Several topics related to the work presented in this thesis are worthy of further investigation that will be possibly pursued in future work.

Slow light enhanced non-linear effects It is important to investigate the relation between slow light and nonlinear effects such as self-phase modulation, two-photon absorption and free carriers, through dispersion-engineered silicon photonic crystal waveguides. We know that there could be an enhancement of non-linear effects due to slow light (Sec. 3.4.2), but it is not clear the process and how to control it. A better understanding of this relation could open the possibility of developing ultra-fast and/or ultra-small all-optical devices.

Pump-probe measurements The heterodyne pump-probe setup, explained in Chapter 6, is a powerful tool to characterize photonic devices, because it may provide also a useful insight of the carrier dynamics in waveguide structures, that are deeply related to non-linear behavior. It could be very interesting to rearrange the setup and start a new set of experiments on photonic crystal waveguides.

Quantum dot photonic crystal waveguide The photonic crystal waveguides proved capable of delaying a pulse, but the delay is fixed by the frequency of the pulse. Even if there are non-linear effects that may permit some new application, the insertion of quantum dot into the waveguide could open a completely new field of operation, achieving efficient and variable control over pulse propagation in compact semiconductor waveguides [76].

Bibliography

[1] J. D. Joannopoulos, S. G. Johnson, J. N. Winn, and R. D. Meade, *Photonic Crystals: Molding the Flow of Light.* Princeton University Press, 2004.

[2] E. Yablonovitch, "Inhibited spontaneous emission in solid-state physics and electronics," *Phys. Rev. Lett.*, vol. 58, no. 20, pp. 2059–2062, May 1987.

[3] S. John, "Strong localization of photons in certain disordered dielectric superlattices," *Phys. Rev. Lett.*, vol. 58, no. 23, pp. 2486–2489, Jun 1987.

[4] K. Sakoda, *Optical properties of photonic crystals.* Springer, 2004.

[5] M. Agio, "Optical properties and wave propagation in semiconductor-based two-dimensional photonic crystals," Ph.D. dissertation, Università degli Studi di Pavia, Italy, and Iowa State University, Iowa, 2002.

[6] A. Kirchner, K. Busch, and C. M. Soukoulis, "Transport properties of random arrays of dielectric cylinders," *Physical review B*, vol. 57(1), pp. 277–288, 1998.

[7] T. C. Choy, *Effective Medium Theory: Principles and Applications.* Oxford University Press, 1999.

[8] A. Yaruv, *Optical waves in crystals.* New York: Wiley, 1984.

[9] V. M. Agranovich and V. E. Kravtsov, "Notes on crystal optics of superlattices," *Solid State Communications*, vol. 55(1), pp. 85–90, 1985.

[10] S. John and R. Rangarajan, "Optimal structures for classical wave localization: An alternative to the ioffe-regel criterion," *Physical Review B*, vol. 88 (14), pp. 10 101–10 104, 1988.

[11] J. B. Pendry and A. MacKinnon, "Calculation of photon dispersion relations," *Physical Review Letters*, vol. 69(19), pp. 2772–2775, 1992.

[12] M. Qiu and S. He, "A non-orthogonal finite-difference time-domain method for computing the band structure of a two-dimensional photonic crystal with dielectric and metallic inclusions," *Journal of Applied Physics*, vol. 87(12), pp. 8268–8275, 2000.

[13] L. Li, "Use of fourier series in the analysis of discontinuous periodic structures," *Journal of the Optical Society of America A*, vol. 19(9), pp. 1870–1876, 1996.

[14] L. C. Andreani and M. Agio, "Photonic bands and gap maps in a photonic crystal slab," *IEEE Journal of Quantum Electronics*, vol. 88(7), pp. 891–898, 2002.

[15] P. Halevi, A. A. Krokhin, and J. Arriaga, "Photonic crystal optics and homogenization of 2d periodic composites," *Physical Review Letters*, vol. 82(4), pp. 719–722, 1999.

[16] D. Cassagne, C. Jouanin, and D. Bertho, "Hexagonal photonic-band-gap structures," *Physical Review B*, vol. 53(11), pp. 7134–7141, 1996.

[17] E. Lidorikis, M. M. Sigalas, E. N. Economou, and C. M. Soukoulis, "Gap deformation and classical wave localization in disordered two-dimensional photonic-band-gap materials," *Physical Review B*, vol. 61(20), pp. 13 458–13 464, 2000.

[18] S. G. Johnson, S. Fan, P. R. Villeneuve, J. D. Joannopoulos, and L. A. Kolodziejski, "Guided modes in photonic crystal slabs," *Physical Review B*, vol. 60(8), pp. 5751–5758, 1999.

[19] T. Ochiai and K. Sakoda, "Dispersion relation and optical transmittance of a hexagonal photonic crystal slab," *Phys. Rev. B*, vol. 63, no. 12, p. 125107, Mar 2001.

[20] D. M. Whittaker and I. S. Culshaw, "Scattering-matrix treatment of patterned multilayer photonic structures," *Phys. Rev. B*, vol. 60, no. 4, pp. 2610–2618, Jul 1999.

[21] T. Ochiai and K. Sakoda, "Nearly free-photon approximation for two dimensional photonic crystal slabs," *Phys. Rev. B*, vol. 64, no. 4, p. 045108, Jul 2001.

[22] T. F. Krauss, R. M. D. L. Rue, and S. Brand, "Two-dimensional photonic-bandgap structures operating at near-infrared wavelengths," *Nature*, vol. 383, 1996.

[23] H. Benisty, D. Labilloy, C. Weisbuch, C. J. M. Smith, T. F. Krauss, D. Cassagne, A. Beraud, and C. Jouanin, "Radiation losses of waveguide-based two-dimensional photonic crystals: Positive role of the substrate," *Applied Physics Letters*, vol. 76, no. 5, pp. 532–534, 2000.

[24] S. G. Johnson, P. R. Villeneuve, S. Fan, and J. D. Joannopoulos, "Linear waveguides in photonic-crystal slabs," *Phys. Rev. B*, vol. 62, no. 12, pp. 8212–8222, Sep 2000.

[25] H. Benisty, "Modal analysis of optical guides with two-dimensional photonic band-gap boundaries," *Journal of Applied Physics*, vol. 79(10), pp. 7483–7492, May 1996.

[26] A. Tavlove, *Computational Electrodynamics: The Finite-Difference Time-Domain Method.* Artech House Publishers, 1995.

[27] K. Yee, "Numerical solution of initial boundary value problems involving maxwell's equations in isotropic media," *Antennas and Propagation, IEEE Transactions on*, vol. 14, no. 3, pp. 302–307, May 1966.

[28] A. Y. Petrov and M. Eich, "Zero dispersion at small group velocities in photonic crystal waveguides," *Applied Physics Letters*, vol. 85, Nov. 2004.

[29] Y. A. Vlasov, M. O'Boyle, H. F. Hamann, and S. J. McNab, "Active control of slow light on a chip with photonic crystal waveguides," *Nature*, vol. 438, pp. 65–69, Nov 2005.

[30] Y. Vlasov, W. M. J. Green, and F. Xia, "High-throughput silicon nanophotonic wavelength-insensitive switch for on-chip optical networks," *Nature Photon.*, vol. 2, pp. 242–246, Mar 2008.

[31] D. O'Brien, A. Gomez-Iglesias, M. D. Settle, A. Michaeli, M. Salib, and T. F. Krauss, "Tunable optical delay using photonic crystal heterostructure nanocavities," *Phys. Rev. B*, vol. 76, no. 11, Sep. 2007.

[32] H. Gersen, T. J. Karle, R. J. P. Engelen, W. Bogaerts, J. P. Korterik, N. F. van Hulst, T. F. Krauss, and L. Kuipers, "Real-space observation of ultraslow light in photonic crystal waveguides," *Phys. Rev. Lett.*, vol. 94, pp. 1–4, Feb. 2005.

[33] L. H. Frandsen, A. V. Lavrinenko, J. Fage-Pedersen, and P. I. Borel, "Photonic crystal waveguides with semi-slow light and tailored dispersion properties," *Opt. Express*, vol. 14, no. 20, pp. 9444–9450, 2006.

[34] J. B. Khurgin, "Optical buffers based on slow light in electromagnetically induced transparent media and coupled resonator structures: comparative analysis," *J. Opt. Soc. Am. B*, vol. 22, no. 5, pp. 1062–1074, 2005.

[35] M. Ibanescu, S. G. Johnson, D. Roundy, C. Luo, Y. Fink, and J. D. Joannopoulos, "Anomalous dispersion relations by symmetry breaking in axially uniform waveguides," *Phys. Rev. Lett.*, vol. 92, no. 6, p. 063903, Feb 2004.

[36] A. Figotin and I. Vitebsky, "Nonreciprocal magnetic photonic crystals," *Phys. Rev. E*, vol. 63, no. 6, p. 066609, May 2001.

[37] R. Engelen, Y. Sugimoto, Y. Watanabe, J. Korterik, N. Ikeda, N. van Hulst, K. Asakawa, and L. Kuipers, "The effect of higher-order dispersion on slow light propagation in photonic crystal waveguides," *Opt. Express*, vol. 14, no. 4, pp. 1658–1672, 2006.

[38] R. Boyd, *Nonlinear Optics*. Academic Press, 2009.

[39] P. Yeh, "Electromagnetic propagation in birefringent layered media," *Journal of Optical Society of America*, vol. 69, no. 5, pp. 742–756, 1979.

[40] B. Lombardet, L. Dunbar, R. Ferrini, and R. Houdre, "Bloch wave propagation in two-dimensional photonic crystals: Influence of the polarization," *Optical and Quantum Electronics*, vol. 37, pp. 293–307, 2005.

[41] T. Kamalakis and T. Sphicopoulos, "A new formulation of coupled propagation equations in periodic nanophotonic waveguides for the treatment of kerr-induced nonlinearities," *IEEE J. Quantum Electronics*, vol. 43, no. 10, pp. 923–933, 2007.

[42] G. Agrawal, *Nonlinear fiber optics*. Academic Press, 2001.

[43] M. Settle, M. Salib, A. Michaeli, and T. F. Krauss, "Low loss silicon on insulator photonic crystal waveguides made by 193nm optical lithography," *Opt. Express*, vol. 14, no. 6, pp. 2440–2445, 2006.

[44] S. Hughes, L. Ramunno, J. F. Young, and J. E. Sipe, "Extrinsic optical scattering loss in photonic crystal waveguides: Role of fabrication disorder and photon group velocity," *Phys. Rev. Lett.*, vol. 94, no. 3, p. 033903, Jan 2005.

[45] M. Skorobogatiy, G. Bégin, and A. Talneau, "Statistical analysis of geometrical imperfections from the images of 2d photonic crystals," *Opt. Express*, vol. 13, no. 7, pp. 2487–2502, 2005.

[46] E. Kuramochi, M. Notomi, S. Hughes, A. Shinya, T. Watanabe, and L. Ramunno, "Disorder-induced scattering loss of line-defect waveguides in photonic crystal slabs," *Phys. Rev. B*, vol. 72, no. 16, p. 161318, Oct 2005.

[47] F. P. Payne and J. P. R. Lacey, "A theoretical analysis of scattering loss from planar optical waveguides," *Optical and Quantum Electronics*, vol. 26, no. 10, pp. 977–986, 1994.

[48] S. Combrié, A. De Rossi, L. Morvan, S. Tonda, S. Cassette, D. Dolfi, and A. Talneau, "Time-delay measurement in singlemode, low-loss photonic crystal waveguides," *Electronics Letters*, vol. 42, no. 2, pp. 86–88, Jan. 2006.

[49] N. Kawai, K. Inoue, N. Ikeda, N. Carlsson, Y. Sugimoto, K. Asakawa, S. Yamada, and Y. Katayama, "Transmittance and time-of-flight study of Al_xGa_{1-x}as-based photonic crystal waveguides," *Phys. Rev. B*, vol. 63, no. 15, p. 153313, Mar 2001.

[50] T. Asano, K. Kiyota, D. Kumamoto, B.-S. Song, and S. Noda, "Time-domain measurement of picosecond light-pulse propagation in a two-dimensional photonic crystal-slab waveguide," *Applied Physics Letters*, vol. 84, no. 23, pp. 4690–4692, 2004.

[51] S. Combrié, E. Weidner, A. DeRossi, S. Bansropun, S. Cassette, A. Talneau, and H. Benisty, "Detailed analysis by fabry-perot method of slab photonic crystal line-defect waveguides and cavities in aluminium-free material system," *Opt. Express*, vol. 14, no. 16, pp. 7353–7361, 2006.

[52] S. Combrié, N.-V.-Q. Tran, E. Weidner, A. de Rossi, S. Cassette, P. Hamel, Y. Jaouën, R. Gabet, and A. Talneau, "Investigation of group delay, loss, and disorder in a photonic crystal waveguide by low-coherence reflectometry," *Applied Physics Letters*, vol. 90, no. 23, pp. 231 104–+, Jun. 2007.

[53] A. Parini, P. Hamel, A. D. Rossi, S. Combrié, N.-V.-Q. Tran, Y. Gottesman, R. Gabet, A. Talneau, Y. Jaouën, and G. Vadalà, "Time-wavelength reflectance maps of photonic crystal waveguides: A new view on disorder-induced scattering," *J. Lightwave Technol.*, vol. 26, no. 23, pp. 3794–3802, 2008.

[54] K. Takada, I. Yokohama, K. Chida, and J. Noda, "New measurement system for fault location in optical waveguide devices based on an interferometric technique," *Appl. Opt.*, vol. 26, no. 9, pp. 1603–1606, 1987.

[55] Y. Gottesman, E. V. K. Rao, and D. G. Rabus, "New methodology to evaluate the performance of ring resonators using optical low-coherence reflectometry," *J. Lightwave Technol.*, vol. 22, no. 6, p. 1566, 2004.

[56] Y. Gottesman and E. Rao, "Non destructive methodology for defect detection and localization in bragg gratings," in *Indium Phosphide and Related Materials, 2005. International Conference on*, May 2005, pp. 578–581.

[57] C. Palavicini, Y. Jaouën, G. Debarge, E. Kerrinckx, Y. Quiquempois, M. Douay, C. Lepers, A.-F. Obaton, and G. Melin, "Phase-sensitive optical low-coherence reflectometrytechnique applied tothe characterization of photonic crystal fiber properties," *Opt. Lett.*, vol. 30, no. 4, pp. 361–363, 2005.

[58] S. Dyer and K. Rochford, "Low-coherence interferometric measurements of the dispersion of multiple fiber bragg gratings," *Photonics Technology Letters, IEEE*, vol. 13, no. 3, pp. 230–232, Mar 2001.

[59] P. Hamel, Y. Jaouën, R. Gabet, and S. Ramachandran, "Optical low-coherence reflectometry for complete chromatic dispersion characterization of few-mode fibers," *Opt. Lett.*, vol. 32, no. 9, pp. 1029–1031, 2007.

[60] S. Combrié, A. D. Rossi, Q. V. Tran, and H. Benisty, "Gaas photonic crystal cavity with ultrahigh q: microwatt nonlinearity at 1.55 μm," *Opt. Lett.*, vol. 33, no. 16, pp. 1908–1910, 2008.

[61] E. Weidner, S. Combrié, N.-V.-Q. Tran, A. D. Rossi, J. Nagle, S. Cassette, A. Talneau, and H. Benisty, "Achievement of ultrahigh quality factors in gaas photonic crystal membrane nanocavity," *Applied Physics Letters*, vol. 89, no. 22, p. 221104, 2006.

[62] M. Notomi, K. Yamada, A. Shinya, J. Takahashi, C. Takahashi, and I. Yokohama, "Extremely large group-velocity dispersion of line-defect waveguides in photonic crystal slabs," *Phys. Rev. Lett.*, vol. 87, no. 25, p. 253902, Nov 2001.

[63] M. D. Settle, R. J. P. Engelen, M. Salib, A. Michaeli, L. Kuipers, and T. F. Krauss, "Flatband slow light in photonic crystals featuring spatial pulse compression and terahertz bandwidth," *Opt. Express*, vol. 15, no. 1, pp. 219–226, 2007.

[64] Y. Gottesman, A. Parini, B.-E. Benkelfat, and E. Rao, "Benefits of concurrent spatial and spectral analysis of photonic components," in *Indium Phosphide and Related Materials, 2008. IPRM 2008. 20th International Conference on*, May 2008, pp. 1–3.

[65] Y. A. Vlasov, M. A. Kaliteevski, and V. V. Nikolaev, "Different regimes of light localization in a disordered photonic crystal," *Phys. Rev. B*, vol. 60, no. 3, pp. 1555–1562, Jul 1999.

[66] Y. Tanaka, T. Asano, Y. Akahane, B.-S. Song, and S. Noda, "Theoretical investigation of a two-dimensional photonic crystal slab with truncated cone air holes," *Applied Physics Letters*, vol. 82, no. 11, pp. 1661–1663, 2003.

[67] K. L. Hall, G. Lenz, E. P. Ippen, and G. Raybon, "Heterodyne pump-probe technique for time-domain studies of optical nonlinearities in waveguides," *Opt. Lett.*, vol. 17, no. 12, pp. 874–876, 1992.

[68] K. L. Hall, A. M. Darwish, E. P. Ippen, U. Koren, and G. Raybon, "Femtosecond index nonlinearities in ingaasp optical amplifiers," *Applied Physics Letters*, vol. 62, no. 12, pp. 1320–1322, Mar 1993.

[69] K. L. Hall, G. Lenz, A. M. Darwish, and E. P. Ippen, "Subpicosecond gain and index nonlinearities in ingaasp diode lasers," *Optics Communications*, vol. 111, no. 67, pp. 589 – 612, 1994.

[70] M. Hofmann, S. Brorson, J. Mørk, P. Skovgaard, J. McInerney, and A. Mecozzi, "Subpicosecond heterodyne four-wave mixing experiments on ingaasp semiconductor laser amplifiers," *Optics Communications*, vol. 139, no. 18, pp. 117 – 124, 1997.

[71] A. Mecozzi and J. Mørk, "Theory of heterodyne pump-probe experiments with femtosecond pulses," *J. Opt. Soc. Am. B*, vol. 13, no. 11, pp. 2437–2452, 1996.

[72] P. Borri, W. Langbein, J. M[oslash]rk, and J. M. Hvam, "Heterodyne pump-probe and four-wave mixing in semiconductor optical amplifiers using balanced lock-in detection," *Optics Communications*, vol. 169, no. 1-6, pp. 317 – 324, 1999.

[73] P. Borri, W. Langbein, J. Mørk, J. M. Hvam, F. Heinrichsdorff, M.-H. Mao, and D. Bimberg, "Dephasing in inas/gaas quantum dots," *Phys. Rev. B*, vol. 60, no. 11, pp. 7784–7787, Sep 1999.

[74] P. Borri, W. Langbein, J. Hvam, F. Heinrichsdorff, M.-H. Mao, and D. Bimberg, "Ultrafast gain dynamics in inas-ingaas quantum-dot amplifiers," *Photonics Technology Letters, IEEE*, vol. 12, no. 6, pp. 594–596, Jun 2000.

[75] G. Agrawal, *Fiber-optic communication systems.* John Wiley and Sons, 1997.

[76] T. R. Nielsen, A. Lavrinenko, and J. M. rk, "Slow light in quantum dot photonic crystal waveguides," *Applied Physics Letters*, vol. 94, no. 11, p. 113111, 2009.

[77] A. Mekis, S. Fan, and J. D. Joannopoulos, "Bound states in photonic crystal waveguides and waveguide bends," *Phys. Rev. B*, vol. 58, no. 8, pp. 4809–4817, Aug 1998.

[78] M. Agio and C. M. Soukoulis, "Ministop bands in single-defect photonic crystal waveguides," *Phys. Rev. E*, vol. 64, no. 5, p. 055603, Oct 2001.

[79] Y. Tanaka, Y. Sugimoto, N. Ikeda, H. Nakamura, K. Asakawa, K. Inoue, and S. Johnson, "Group velocity dependence of propagation losses in single-line-defect photonic crystal waveguides on gaas membranes," *Electronics Letters*, vol. 40, no. 3, pp. 174–176, Feb. 2004.

[80] F. Romstad, "Absorption and refractive index dynamics in waveguide semiconductor absorbers," Ph.D. dissertation, Technical University of Denmark, Copenhagen, Denmark, 2002.